

**IMAGE PROCESSING METHODS FOR THE DETECTION OF
ACUTE REJECTION AFTER KIDNEY TRANSPLANTATION**

By

Seniha Esen Yuksel

B.Sc., EE, Middle East Technical University, 2003

A Thesis

Submitted to the Faculty of the
Graduate School of the University of Louisville
in Partial Fulfillment of the Requirements
for the Degree of

Master of Science

Department of Electrical and Computer Engineering
University of Louisville
Louisville, Kentucky

December 2005

**IMAGE PROCESSING METHODS FOR THE DETECTION OF
ACUTE REJECTION AFTER KIDNEY TRANSPLANTATION**

By

Seniha Esen Yuksel

A Thesis Approved on

by the Following Thesis Committee:

Aly A. Farag, Ph.D., Thesis Director

Georgy Gimel'farb, Ph.D.

Xiangqian Liu, Ph.D.

Tamer Inanc, Ph.D.

ACKNOWLEDGMENTS

I would like to extend my heartiest gratitude to my advisor Prof. Aly A. Farag, who has supported me for an invaluable educational opportunity at the CVIP Lab. He opened my mind to research, and my way to many possibilities. I cannot thank him enough, but shall remain grateful for all he has done.

I would also like to express my sincere thanks to Dr. Mohamed Abou El-Ghar and Dr. Tarek Eldiasty for the kidney images as well as for their insightful comments; and to my thesis committee members Dr. Georgy Gimel'farb, Dr. Xiangqian Liu, and Dr. Tamer Inanc for their valuable suggestions. Dr. Gimel'farb's encouragement at hard times has been especially invaluable.

I would like to thank all the members of the CVIP Lab for making my stay in Louisville enjoyable; with special thanks to Ayman El-Baz, for he has never hesitated to share his experience in the field and has been a good teacher and a great friend. Also I give my thanks to Sabry Hassouna, who introduced me to the possibilities of Qt, VTK and ITK tools, to Mike Miller for reviewing my thesis, and to my office-mate Noha El-Zehiry for being a caring person. I am feeling so lucky to have met my colleagues in the CVIP Lab and experience a great research environment with them.

The last, but not the least, I would like to thank Prof. Gonul Turhan Sayan and Prof. Gozde Bozdagi from METU for supporting me to pursue my masters in the USA, and for encouraging me during my stay.

This thesis is dedicated to my family, my mother Prof. Oznur Yuksel, my father Arch. Huseyin Yuksel, and my brother Dr. Mehmet Eren Yuksel. Nothing could have been possible without their support and love.

ABSTRACT

IMAGE PROCESSING METHODS FOR THE DETECTION OF ACUTE REJECTION AFTER KIDNEY TRANSPLANTATION

Seniha Esen Yuksel

December 02, 2005

Acute rejection is the most important cause of renal dysfunction after kidney transplantation, but the currently used noninvasive techniques are not specific enough to detect acute rejection. This thesis investigates the potentials of Dynamic Contrast Enhanced Magnetic Resonance Imaging (DCE-MRI) as a noninvasive imaging technique to differentiate acute rejection transplants from normal functioning transplants; and focuses on finding image analysis techniques for the registration and segmentation of renal images. In the image analysis framework of this study, mutual information registration is used to correct the motion due to patient movements. For the segmentation of the kidney from the abdomen images, a novel deformable model energy is proposed. With this new energy, the deformable model evolves using both prior shape and current gray level information. To further segment the kidney into cortex and medulla structures, another deformable model energy is proposed based only on gray level information. At the end of the segmentation, average intensity vs. time curves are plotted to evaluate the perfusion patterns of acute rejection patients and normal functioning transplants. The outcome of this research is an image analysis framework embedded into a graphical user interface to be easily tested by the doctors.

TABLE OF CONTENTS

ACKNOWLEDGMENTS	iii
ABSTRACT	iv
LIST OF TABLES	vii
LIST OF FIGURES	viii
NOMENCLATURE	xv
CHAPTER	
I. INTRODUCTION	1
A. Protocol of the Data Acquisition	3
B. Scope of the Thesis	7
C. Framework of the Proposed Image Analysis System	8
D. Outline of the Thesis	14
II. BACKGROUND	15
A. Anatomy and Functions of the Kidney	15
B. Properties of the Contrast Agent Gd-DTPA	18
C. Related Work in Renal Image Analysis Using DCE-MRI	20
D. A Note on Protocol Selection	23
III. REGISTRATION	27
A. Mutual Information Metric	28
1. Density Modeling via Joint Histograms	30
2. Density Modeling via Parzen Windowing	32
3. Implementation Issues	35
B. Validation of Registration	35
C. Registration Results	40
D. Summary	41
IV. SEGMENTATION	47
A. Segmentation of the Kidney from the Surrounding Organs	47
1. Image Subtraction and Connected Component Analysis	49
2. Deformable Models	51
3. Proposed Deformable Model	57

a. Mixture of Gaussians and the EM Algorithm	58
b. Mixture of Gaussians with Positive and Negative Components	62
c. Sequential EM-Based Initialization	64
d. Shape Modeling	65
e. Energy Function	70
B. Segmentation into Cortex and Medulla	83
C. Segmentation Results	84
V. EVALUATION OF THE PERFUSION SIGNALS	92
VI. CONCLUSIONS	96
REFERENCES	101
APPENDICES	
I. GENETIC ALGORITHMS	108
II. DERIVATIVES AND GRADIENTS	113
III. KASS'S ACTIVE CONTOURS ALGORITHM	115
IV. WILLIAMS'S ACTIVE CONTOURS ALGORITHM	117
CURRICULUM VITA	119

LIST OF TABLES

TABLE	PAGE
1. Mutual information registration parameters.	36
2. Registration of test sequence 1 to the reference image: robustness to translation (in pixels) and rotation R (in degrees).	38
3. Registration of test sequence 2 to the reference image: robustness to translation (in pixels) and rotation R (in degrees).	40
4. Affine registration of the kidney database.	70
5. Parameters used in genetic algorithms.	112

LIST OF FIGURES

FIGURE	PAGE
1. A block diagram of the proposed image analysis to create a CAD system for renal transplantation.	4
2. Example of a DCE-MRI series. For each patient, 150 images are taken from one cross section with 4 second intervals. Six images of one subject (numbers 1, 4, 5, 6, 10, 15) are shown here to give an idea of the protocol.	5
3. Current Protocol. For each subject, 150 abdomen images are taken from one cross-section with 4 second intervals. An example of the DCE-MRI series for one subject is shown here with the first 45 images in the sequence.	6
4. Extracting the signals from DCE-MR images.	7
5. The framework of the proposed system. After the image acquisition, the images are aligned using mutual information registration. Then the kidney is segmented from the abdomen images, and it is segmented further into cortex and medulla compartments. The segmented kidney mask is propagated over the whole sequence to get the average cortex and medulla intensity values; then these intensities are plotted as renograms; and the critical points in the renograms are used in the classification.	10
6. The segmentation framework of the proposed system. At the beginning of the segmentation framework, an average prior kidney shape and an average signed distance map density is obtained from previously segmented and aligned kidney images. For a new patient, the user selects a late enhancement image and seed points from an early enhancement image. The gray level density estimation of the late enhancement image is obtained via a modified EM algorithm, and it is combined with the average signed distance map density of the database to be used as the energy of a deformable model. By evolving the deformable model with prior shape and current gray level information, a kidney mask is obtained. The kidney region is further segmented into cortex and medulla compartments depending on the gray level density estimation of the kidney region in the early enhancement image. . . .	11
7. More detail on the steps to obtain the average shape for the segmentation framework. The kidneys are manually segmented from the abdomen scans, and they are aligned by affine registration. The signed distance maps of these binary images are calculated wrt. the kidney boundaries, and they are	

averaged to obtain the average signed distance map. From the average signed distance map, an average kidney shape is obtained (positive distances represent the kidney, negative distances represent the background). From the histograms of the signed distance maps, an average signed distance map density is obtained via a modified EM algorithm.	12
8. Segmentation framework illustration with images. An early enhancement image, seed points, and a late enhancement image are selected from the current patient. For kidney segmentation, a deformable model is initialized at the seed points to evolve with the gray level density estimation and the signed distance map density estimation of prior shape. With a second deformable model, cortex and medulla are extracted from the kidney region	13
9. Location of a kidney.	16
10. Anatomy of a kidney.	17
11. Structure of a nephron.	17
12. Ideal patterns of signal enhancement in the cortex of a normal transplant with V = Vascular Phase, T = Tubular Phase, D = Ductal Phase. The signal intensity increases immediately after the injection of the contrast agent in about 40 seconds, reaches a maximum within the first 100 seconds and starts to drop slowly to its initial value while the urine is formed.	19
13. Old protocol. An example of the DCE-MRI series for one subject. For each subject, 6 cross-sections are taken with 30 second intervals.	24
14. Old protocol perfusion curves for cortex (a) and medulla (b). There is a 30 second interval between each scan. At the 30 th second (first scan), most of the important perfusion has already occurred so the important intermediate data is lost. Therefore, smaller time intervals are required between each scan.	25
15. Illustration of the misalignment of two images. In these images, compared with one another, the anatomical structure is located at different positions. A rigid registration would translate and rotate the right image to align it with the left image.	27
16. The transplanted kidney [4]. After kidney transplantation, the new kidney is placed to the lower abdomen; thus, the transplanted kidney does not show considerable motion due to breathing. The main motion it would experience is due to patient movement.	28
17. Calculating the joint histogram from the occurrence of gray levels.	33
18. Calculating the joint density from the joint histogram by normalization.	34
19. Calculating the marginal densities from the joint density by summing over the rows and columns.	34
20. Three images from a sequence (a, b, c), their gray level densities (d, e, f) and	

the cumulative distributions (CDF's) (g, h, i). A mask is obtained from (b), and by inverse mapping, the test images (j, k, l) are obtained for zero translation and rotation.	39
21. A mask image is generated manually based on the real kidney image in Fig. 20(b). This mask is transformed with various rotations (R in degrees) and translations in x direction (T_x) and in y direction (T_y) in pixels.	42
22. Test Sequence 1. Background, cortex and medulla structures in the mask are filled separately with random variables obtained via inverse mapping from the ray level CDF's (Fig. 20(g)) of Fig. 20(a).	43
23. Test Sequence 2. Background, cortex and medulla structures in the mask are filled separately with random variables obtained via inverse mapping from the gray level CDF's (Fig. 20(h)) of Fig. 20(b)).	44
24. Sample registration results for two images from one data set. The moving image in (b) is registered to the fixed image in (a), and the resultant registration is shown in (c). A checkerboard image is generated from (a) and (c) to test the quality of the registration visually. A checkerboard image is basically obtained by patching one square region from the fixed image and another square region from the moving image after registration, and the expectation is to see continuous contours in between the patches, which is very well obtained in (d). Registration results: Rotation $R = 1.82$ degrees, translation in x direction $T_x = 1.48$ pixels, translation in y direction $T_y = 0.77$ pixels, MI metric = 0.27.	45
25. Sample registration results for two images from one data set. The moving image in (b) is registered to the fixed image in (a), and the resultant registration is shown in (c). A checkerboard image is generated from (a) and (c) to test the quality of the registration visually. A checkerboard image is basically obtained by patching one square region from the fixed image and another square region from the moving image after registration, and the expectation is to see continuous contours in between the patches, which is very well obtained in (d). Registration results: Rotation $R = 0.47$ degrees, translation in x direction $T_x = 2.33$ pixels, translation in y direction $T_y = 0.10$ pixels, MI metric = 0.18.	46
26. The kidney to be segmented from the surrounding organs (a). The first stage of our segmentation algorithm is to obtain a kidney mask (b). Using this mask, kidney is isolated from the outer structures in (c). In the second stage of the segmentation approach, the kidney is segmented into its cortex (white region) and medulla (gray region) compartments (d).	48
27. The motivation for segmenting the kidney from the surrounding organs. . . .	49
28. Image subtraction. The average of non-enhanced images (a) and (b) are subtracted from the average of enhanced images (c) and (d). The subtraction image is scaled to $[0, 255]$ intensity levels as shown in (e), and the largest	

connected component is extracted (f).	50
29. A curve can be represented parametrically as $v(s) = (x(s); y(s)); 0 \leq s \leq 1$. . .	52
30. The movement of the deformable contour towards the edges. The black contour shows the initial snake at time t . At time $t + 1$, black contour deforms towards the edges (the red kidney outlier) and forms the blue contour. Green dots are the nodes that make up the contours.	52
31. In the greedy algorithm, each point v_i of the contour is moved within a small neighborhood (e.g. 3x3) to the point which minimizes the energy functional. .	54
32. Williams and Shah algorithm. (a) The contour is initialized manually in the close vicinity of the edges. This initial contour deforms to give the segmentation in (b). Note that the algorithm still has problems in penetrating into the concavities.	54
33. The kidney to be segmented from the surrounding organs (a). The results of some popular segmentation algorithms that depend only on gray level and gradient information: (b) connected thresholding, (c) thresholding level sets, (d) fast marching level sets, (e) geodesic active contours segmentation.	56
34. (a) An test density $f(q)$ composed of the three Gaussian components given in (b). (c) The approximation $p(q)$ (shown in red) to $f(q)$ (shown in blue) using the traditional EM algorithm. The traditional EM algorithm could not capture the density due to the negative Gaussian component. (d) The modified EM algorithm (shown in blue) introduced by Farag <i>et al.</i> offers a better approximation to the empirical density (shown in red) as it can capture the negative Gaussian component.	62
35. A kidney image (a) with its empirical density $f(q)$ given in (b). The empirical density $f(q)$ we want to estimate (in red), and its approximation with two dominant modes using the traditional EM algorithm (in blue) (c). The two dominant modes (d) corresponding to the density estimation of $class_1$ (the kidney) and $class_2$ (the background) found by the traditional EM algorithm. .	66
36. (a) The error $\Delta(q)$ between the empirical density $f(q)$ and the two dominant modes shown in Fig. 35 (c). (b) Error is scaled to represent a density function. (c) Estimation of error density and the components forming this error density with signs given in (d).	67
37. (a) The empirical density $f(q)$ shown in red and its estimation $p_2(q)$ shown in blue. (b) Step-10 of the Sequential EM algorithm assigns the error components to the two dominant classes so as to minimize the error between the empirical density $f(q)$ and its estimation $p(q)$, and finds the threshold to be 109. If only this threshold was used in segmentation, the segmentation result would be as in (c). When the kidney and background are segmented manually, the densities of these two classes are as in (d), and the threshold after manual segmentation is 119. Note the similarity between the automatically estimated density (b) and the manually obtained density (d). . .	68

38. Kidney database from 10 subjects.	71
39. Segmented database from 10 subjects.	72
40. Affine registration of the database.	73
41. Final registered database from 10 subjects.	74
42. Boundaries of the aligned kidneys from 10 subjects.	75
43. Signed distance maps of the 10 subjects.	76
44. Signed distance map densities of the 10 subjects.	77
45. (a) The average density obtained by averaging the densities given in Fig. 44. (b) The average kidney shape obtained from the signed distance maps given in Fig. 43. After averaging the signed distance maps, the pixels with positive signed distance map values are assigned to be white indicating the kidney region, the pixels with negative signed distance map values are assigned to be black indicating the background.	78
46. (a) The average signed distance map density. (b) The estimated two dominant modes which presents the kidney area and its background, (c) the scaled-up absolute deviation of the approximation, (d) the positive and negative LCDG components, (e) Final density estimation, and (f) the densities for two classes (red is for the kidney, blue is for the background).	79
47. The initialization of the deformable contour. Blue dots show the contour points making up the yellow deformable contour. For each of the control points $v(i)$, greedy algorithm looks at the 3x3 neighborhood and moves to the point with lowest energy. Moving to the outer points (red pixels) makes the contour grow whereas moving inside (green pixels) makes the contour shrink.	81
48. The proposed deformable model in the kidney. For each of the neighbors of the control point $v(i)$, four values are calculated to form the external energy: two values from the signed distance density estimation ($p_s(d k = 1)$ and $p_s(d$ $ k = 2)$), and two values from the gray level density estimation ($p_g(q k = 1)$ and $p_g(q k = 2)$).	82
49. Segmenting the kidney into cortex and medulla.	84
50. (a) A late enhancement image to segment. (b) Manual segmentation. (c) Segmentation result with error 11.51% w.r.t the area of the manually segmented kidney. (d) Segmented kidney. (e) An image from the sequence where cortex and medulla can be identified best. (f) The resultant cortex and medulla segmentation based on (e). Gray level parts are the medulla structures and the rest is the cortex.	85
51. (a) A late enhancement image to segment. (b) Manual segmentation. (c) Segmentation result with error 7.60% w.r.t the area of the manually	

segmented kidney. (d) Segmented kidney. (e) An image from the sequence where cortex and medulla can be identified best. (f) The resultant cortex and medulla segmentation based on (e). Gray level parts are the medulla structures and the rest is the cortex.	86
52. (a) A late enhancement image to segment. (b) Manual segmentation. (c) Segmentation result with error 11.36% w.r.t the area of the manually segmented kidney. (d) Segmented kidney. (e) An image from the sequence where cortex and medulla can be identified best. (f) The resultant cortex and medulla segmentation based on (e). Gray level parts are the medulla structures and the rest is the cortex.	87
53. (a) A late enhancement image to segment. (b) Manual segmentation. (c) Segmentation result with error 8.29% w.r.t the area of the manually segmented kidney. (d) Segmented kidney. (e) An image from the sequence where cortex and medulla can be identified best. (f) The resultant cortex and medulla segmentation based on (e). Gray level parts are the medulla structures and the rest is the cortex.	88
54. (a) A late enhancement image to segment. (b) Manual segmentation. (c) Segmentation result with error 12.19% w.r.t the area of the manually segmented kidney. (d) Segmented kidney. (e) An image from the sequence where cortex and medulla can be identified best. (f) The resultant cortex and medulla segmentation based on (e). Gray level parts are the medulla structures and the rest is the cortex.	89
55. (a) A late enhancement image to segment. (b) Manual segmentation. (c) Segmentation result with error 7.47% w.r.t the area of the manually segmented kidney. (d) Segmented kidney. In this patient, medulla was not identifiable.	90
56. (a) A late enhancement image to segment. (b) Manual segmentation. (c) Segmentation result with error 6.32% w.r.t the area of the manually segmented kidney. (d) Segmented kidney. In this patient, medulla was not identifiable.	91
57. Ideal cortical perfusion patterns of normal and acute rejected kidneys.	94
58. (a) Normalized cortex signals from 4 subjects. (b) Normalized medulla signals from 4 subjects. There are 4 seconds between each scan. Subjects 1&2 are acute rejection, subject 3 is normal and subject 4 is chronic glomerulopathy proved by biopsy. In the cortex curves, the normal patient shows the expected abrupt increase in intensity and the fast decrease, followed by a constant valley and a slow decrease. On the other hand, these abrupt patterns are not seen in acute rejection patients, there is no definite peak, and the time to reach the peak intensity is delayed. Also in medullary curves, the normal patient reaches the first peak faster than others. Subject 4 shows that DCE-MRI is also powerful to distinguish other diseases.	95

59. Main page of the software.	97
60. Registration page of the software.	97
61. Segmentation page of the software.	98
62. A cycle of the Genetic Algorithms.	111
63. Pascal's Triangle and the signs assigned to each entry.	113
64. Function $v(s)$ can be represented as an array of nodes, where the last node $v(N)$ is equal to the first node $v(0)$	114

NOMENCLATURE

DCE–MRI	Dynamic Contrast Enhanced Magnetic Resonance Imaging
US	Ultrasound
CT	Computed Tomography
Gd-DTPA	Gadolinium diethylene triamine pentaacetic acid
CDF	Cumulative distribution function
A	Fixed Image
B	Moving Image
a	Gray level value (intensity) of image A
b	Gray level value (intensity) of image B
$p_A(a), p_B(b)$	Marginal gray level densities of images A and B
$p_{AB}(a, b)$	The joint gray level density of images A and B .
$I(A, B)$	Mutual information of the images A and B .
$H(A), H(B)$	Entropy of images A and B .
$H(A/B), H(B/A)$	Conditional (relative) entropies
$H(A, B)$	Joint entropy of A and B
$NMI(A, B)$	Normalized mutual information metric
T	Transformation function
T_x, T_y	Translation in x and y directions
R	Rotation in degrees
$h_A(a), h_B(b)$	Histogram of intensities for images A and B
$h_{AB}(a, b)$	Joint histogram of images A and B

S, R	Intensity samples from images A and B
s_j, r_j	Each one of the intensity samples in S
N_s, N_r	Sizes of S and R
K	Gaussian kernel $\mathfrak{N}(0, \psi)$
X	Random variable with cumulative distribution function F
U	A uniform random variable
I_{subt}	Subtraction image
I_{scaled}	Rescaled image into $[0, 255]$ intensity range
$v(s)$	A continuous deformable contour
s	Index of a point on the continuous deformable contour
v_i	Discrete control points of a deformable contour located at (x_i, y_i)
E	Total energy of the deformable model
E_{int}	Internal energy
E_{ext}	External energy
$E_{elastic}$	Elastic energy
$E_{bending}$	Bending energy
α	Adjustable constant for elastic energy
β	Adjustable constant for bending energy
v', v'', v''''	First, second and fourth derivatives of the deformable contour
$G(\cdot)$	2D Gaussian kernel
\mathbf{Y}	Gray level image of size \mathbf{N}
$ \nabla \mathbf{Y} $	Image gradient
q	Gray level value in the range $[0, Q]$
d	Signed distance
k	Region label with $k = 1$ for background, $k = 2$ for kidney
k^*	Region of interest where the contour is growing

$p_g(q k)$	Density estimation of the gray level for class k
$p_s(d k)$	Density estimation of the signed distance map for class k
$f(q)$	normalized histogram (empirical density) of image $\mathbf{Y}(i, j)$
$\theta = [\mu, \sigma]$	Mean μ and the standard deviation σ of a Gaussian density function $\varphi(q \theta)$
$p_{\mathbf{w}, \Theta}(q)$	A linear combination of K different Gaussians
\mathbf{w}	Weights of the Gaussian components
π	Probabilities of Gaussian components
m	Iteration number
$L(\mathbf{w}, \theta)$	Log likelihood in terms of parameter \mathbf{w}, θ
C_p, C_n	Number of positive and negative Gaussian components
C	Total number of Gaussian components (total of C_p and C_n)
π_p, π_n	Conditional weights of the positive and negative components
$p_2(q)$	A density with two Gaussian components
π_p, π_n	Probabilities of positive and negative Gaussian components
s_f	Scaling factor
$e(t)$	Classification error
t	Threshold
s_c	Scaling parameter
$S_d(i, j)$	Signed distance function
V	2D kidney contour
$S_{av}(i, j)$	Average sign distance
R_V	Region inside the kidney
$d\left((i, j), V\right)$	Minimum Euclidean distance between the image location (i, j) and the curve V

CHAPTER I

INTRODUCTION

In the United States, more than 12000 renal transplantations are performed each year [5]; but the transplanted kidneys face a number of surgical and medical complications that cause a decrease in their functionality. Although such a decrease in functionality can be reversed by proper treatment strategies and drug therapies [6], the currently used techniques are not specific enough to diagnose the possible diseases. Such as, *measurement of creatinine levels* can be affected by diet and medications [7]. *Clearance of inulin* requires multiple blood and urine tests, and it provides information on both kidneys together, but not unilateral information [8]. On the other hand, imaging tests are favorable since they provide information on each kidney separately. However, the most frequently used imaging technique, *scintigraphy* (also called nuclear imaging), preferred for its good functional information, does not give good spatial resolution. Without good spatial resolution, precise anatomical detail cannot be obtained, so the diseases that affect the different parts of the kidney (such as cortex and medulla) cannot be diagnosed accurately [9]. Moreover, scintigraphy exposes the patients to a small dose of radioactivity [10]. As such, another traditional imaging modality, *Computed Tomography* (CT) uses nephrotoxic contrast agents, and exposes the patients to radiation despite its superior functional and anatomical information [11]. *Ultrasonography* was found to show normal findings despite severe renal function [12], and several studies on color Doppler sonography and power Doppler sonography (e.g. [13–15]) have not been able to find significant information to evaluate renal function. Therefore, despite all its high costs and morbidity rates, *biopsy* is still remaining as the golden standard for diagnosis after renal transplantation. Unfortunately, biopsy has the downside effects of subjecting the patients to risks like bleeding and infections, and moreover, the relatively small needle biopsies may lead to over or underestimation of the extent of inflammation in the entire graft [16]. Hence, a noninvasive and repeatable technique is not only useful but also needed to insure the survival of the transplanted kidneys.

Among the diagnostic possibilities after renal transplantation (such as acute rejection, acute tubular necrosis, cyclosporin toxicity and obstruction [17]), the most important cause of renal dysfunction is acute rejection [18]. Acute rejection is the attack of the recipient's immune system to the foreign kidney; so a prompt anti-rejection therapy can suppress the immune system and save the transplanted kidney [19].

The main objective of this thesis is to find image analysis techniques for the detection of acute rejection using a fairly new imaging technique: Dynamic Contrast Enhanced Resonance Imaging (DCE-MRI), which is trying to enter the clinical settings with its superior anatomical (because it is MRI) and functional information (because of the contrast agent). With DCE-MRI, it has been possible to distinguish the different structures of the kidney (such as the cortex and medulla) in a noninvasive way, and combined with the function information, image analysis on DCE-MRI can help in detecting the diseases that affect the different parts of the renal transplants.

In Dynamic Contrast Enhanced Resonance Imaging (DCE-MRI), a contrast agent called Gd-DTPA is injected into the bloodstream, and during its pass from the blood to the kidneys to the urine system, kidneys are imaged rapidly and repeatedly. As the contrast agent Gd-DTPA perfuse into the kidney, it causes a change in the relaxation times of the tissue and creates a contrast change (intensity increase/decrease) in the images. If the intensity is averaged over the kidney tissue and plotted over the time, a signal curve (change in intensity vs. time) is obtained. Such intensity curves obtained from the kidney are called MR renograms [9]. The pattern of an MR renogram is an indicator of the kidney's degree of functionality, and it can be used in determining the type of the rejection or dysfunction. Moreover, since DCE-MRI provides good anatomical information, separate renograms can be obtained for the cortical and medullary structures of the kidney, which would help in distinguishing the diseases that affect different parts of the kidneys. Hence, a typical protocol using dynamic MRI involves the following steps: 1) collect a sequence of images from the kidney region as the contrast agent perfuse through the kidney; 2) follow the contrast difference in the kidney with time (image intensity information from the cortical and medullary regions vary with time as the contrast agent perfuse through the kidney); and 3) establish a correspondence between change of contrast in the image sequence and the status of the kidney.

Such a protocol needs some intermediate image processing steps; namely, segmentation, registration and classification; which are the three main chapters of this thesis. But before going into the details of these steps, in the next section, the data acquisition framework of the University of Louisville and University of Mansoura collaboration is introduced which includes the urine and ultrasound tests as well as DCE-MRI; with a special emphasis on the DCE-MRI protocol. In Sec. B, the scope of the thesis is given, and the importance of this study is discussed from the image analysis point of view. In Sec. C, a summary of the proposed image analysis framework is given. Finally, in Sec. D, the chapter is concluded with an outline of the thesis.

A. Protocol of the Data Acquisition

The early and noninvasive detection of acute rejection is crucial; however, the currently used techniques such as nuclear imaging or ultrasonography are far from giving both the functional and anatomical information accurately; therefore, the doctors in University of Mansoura needed a noninvasive and repeatable technique for the diagnosis of acute renal rejection via the use of DCE-MRI; which has led to the ongoing collaboration between the University of Mansoura and the CVIP Lab at the University of Louisville.

In the big framework of this collaborative research, after transplantation, at 9am daily, patients are tested for urine and blood findings, and following these tests, the abdomen is imaged daily using Color Doppler Ultrasonography for two weeks. If circumstances do not force it to be before, DCE-MRI is taken at the end of the two weeks nursing period. If in addition to the previous tests, DCE-MRI findings show normal, then no further actions are taken. However, if the findings are abnormal, a biopsy is performed to understand the type of the rejection or the disease of the kidney; and the images of the patients with histopathological diagnosis of acute rejection episodes and normal transplant images are sent to University of Louisville to test and train the imaging software. An illustration of the combination of these findings is given in Fig. 1.

For the protocol of DCE-MRI, during the development of this thesis, we observed that a good selection of the imaging protocol is as important as the image analysis – if not more important. The key point in the protocol is to take the images as fast as possible while trying

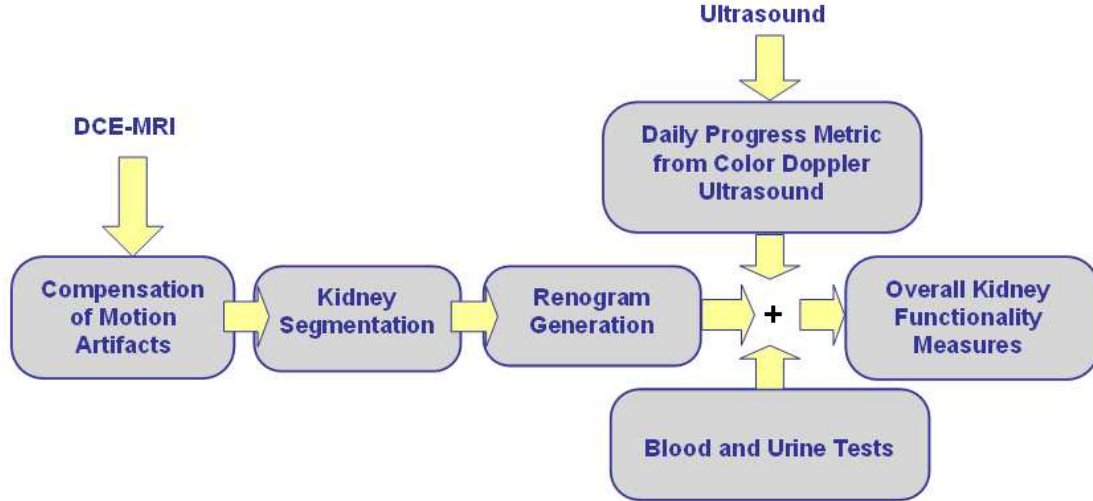


FIGURE 1: A block diagram of the proposed image analysis to create a CAD system for renal transplantation.

to conserve the quality. A compromise in image quality results in too much noise and partial volume effects, but on the other hand, a compromise from speed results in less data points that prevented us from being able to classify the signals. Therefore, with collaborative efforts, the protocol was modified a number of times to acquire a standard and better quality imaging. The protocol described below has been found to be the optimum with the current MRI hardware (a Signa Horizon GE 1.5T scanner).

In our protocol, gradient echo T1 imaging is employed by a Signa Horizon GE 1.5T scanner (Signa Horizon LX Echo speed; General Electric Medical Systems, Milwaukee, WI, USA) with the use of phased array Torso surface coil, and the contrast agent Gadolinium DTPA is introduced via a wide bore veno-catheter placed at antecubital vein at a rate of 3-4 ml/sec with a dose of 0.2 ml/kg.BW. Images are taken at 5mm thickness with no inter-slice gap, repetition time (TR) 34 msec, TE minimum, field of view (FOV) 42x42 cm and matrix of 1005x804. For each patient, 150 temporal sequences of coronal scans are taken with 4 second intervals. Samples of what a DCE-MRI looks like with this protocol are shown in Fig. 2 and in Fig. 3.

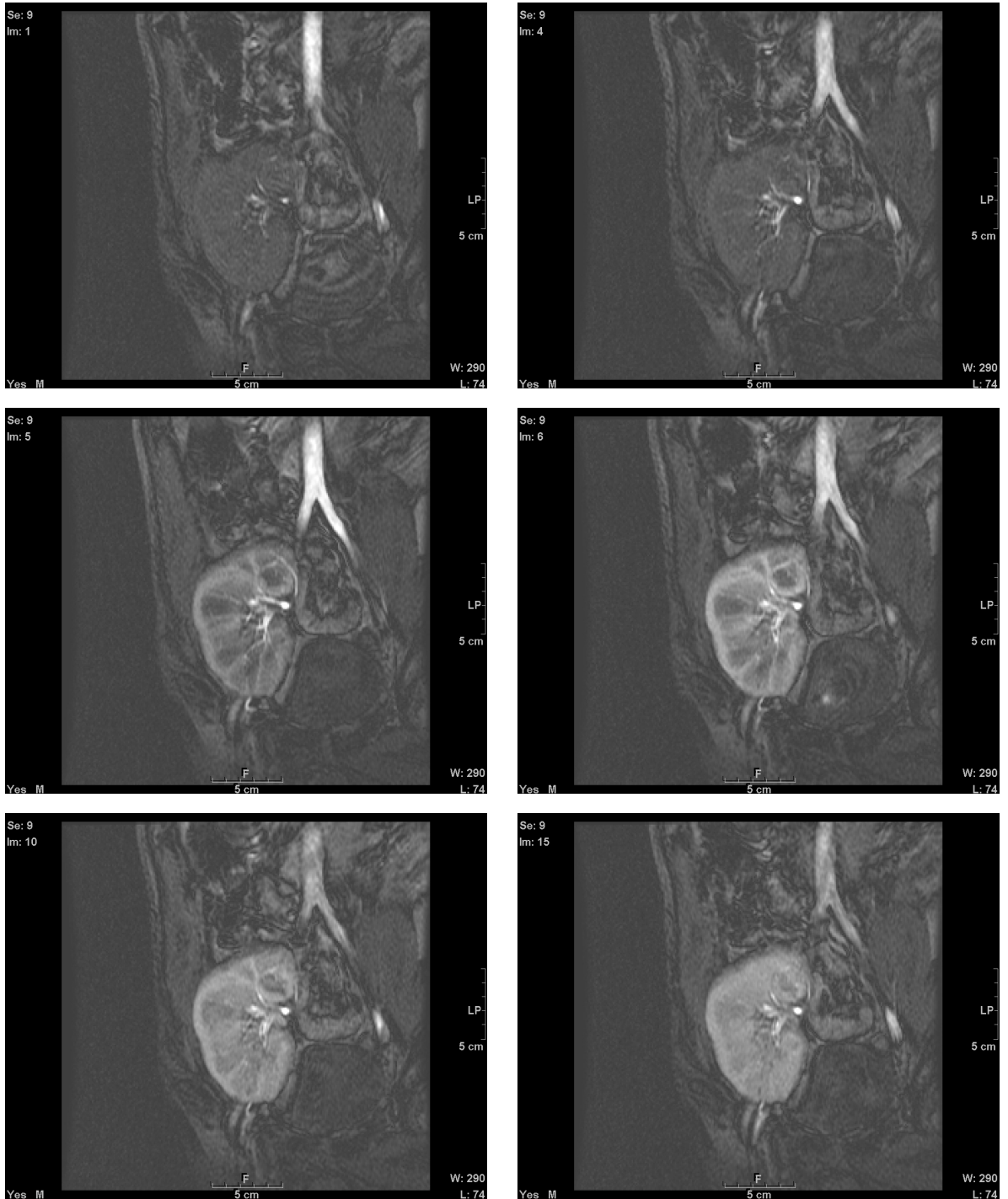


FIGURE 2—Example of a DCE-MRI series. For each patient, 150 images are taken from one cross section with 4 second intervals. Six images of one subject (numbers 1, 4, 5, 6, 10, 15) are shown here to give an idea of the protocol.



FIGURE 3—Current Protocol. For each subject, 150 abdomen images are taken from one cross-section with 4 second intervals. An example of the DCE-MRI series for one subject is shown here with the first 45 images in the sequence.

B. Scope of the Thesis

This thesis focuses on the DCE-MRI findings of the aforementioned collaboration, and aims at building an imaging software that aids in differentiating normal functioning transplants from acute rejection. With DCE-MRI, a contrast change is observed in the kidney images while the contrast agent perfuse into the kidney as shown in Figs. 2 and 3. The ultimate aim of this thesis is to find the patterns of this contrast change and use them in classification as shown in Fig. 4.

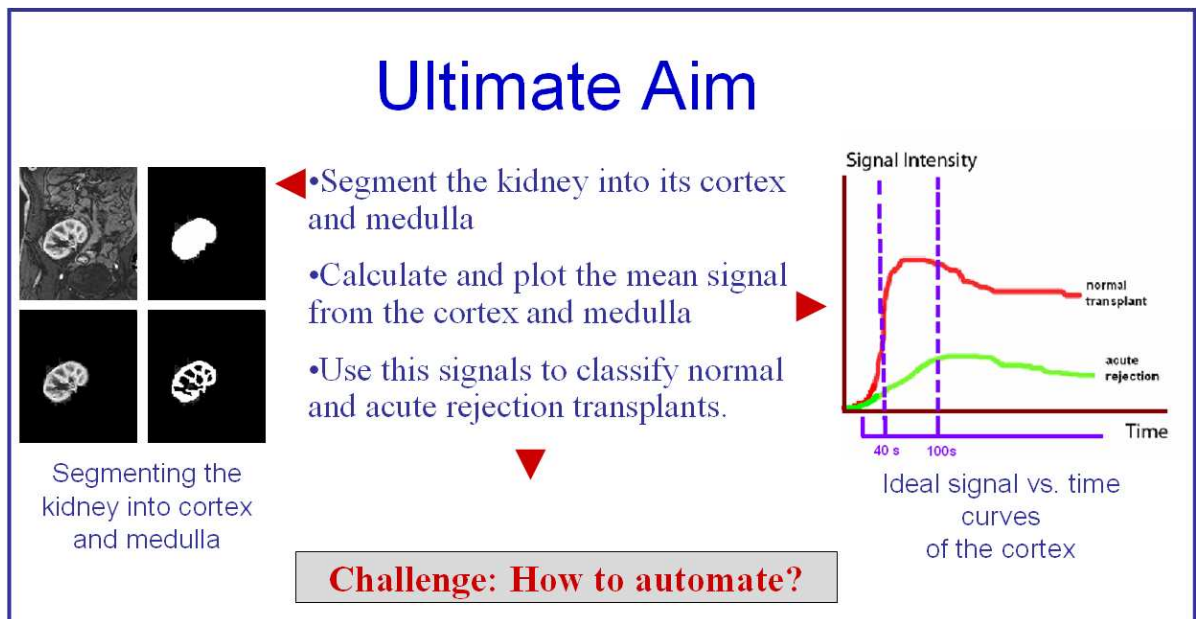


FIGURE 4: Extracting the signals from DCE-MR images

However, extracting the signal patterns is not trivial; and requires some very important image processing steps. The main problems arising in the image processing are three fold:

(i) In dynamic renal perfusion MRI, the abdomen is scanned repeatedly and rapidly after the injection of the contrast agent. Therefore, the images suffer from the motion induced by the patient if he/she moves during the scan, so these images should be registered accurately to correct the motion.

(ii) For the automatic construction of the renograms, first the kidney should be segmented from the surrounding structures, and then it should be segmented into its cortical and medullary structures. However, the time course for the filtration of the contrast agent through the kidneys is of the order of minutes, requiring fast acquisition techniques that take

seconds only. To be able to image this process, DCE-MRI is a faster MR imaging modality, with an inherent compromise between the spatial and temporal resolution [20]. Consequently, renal images suffer from the high levels of noise and partial volume effects, requiring advanced segmentation methods that are robust to noise. Another challenge in the segmentation step is that in some diseases such as acute rejection, the cortico-medullary contrast enhancement is less observed compared to the normal patients, so the individual segmentation of the cortex and medulla becomes more difficult.

(iii) During signal analysis, functional information is extracted by calculating the average intensity of the cortex and the medulla, and plotting these intensity signals over time. From these signals, several features are extracted, and used in the classification of the diseases. However, the inherent noise in the images also reflects itself to the renograms, and combined with the several degrees of the diseases and the patient characteristics (age, sex etc.), the findings can be mostly overlapping.

Still, despite all the problems in image analysis, DCE-MRI is the only noninvasive method that provides both functional and anatomic information, so the efforts are worthwhile, and the findings of this thesis provides an encouraging picture for further research in this area.

C. Framework of the Proposed Image Analysis System

To overcome the previously discussed problems, we proposed an image analysis framework in this thesis as illustrated in Fig. 5. The framework starts with the data acquisition of 150 images from a kidney cross-section with 4 second intervals as was shown in Fig. 3. These images are then aligned using mutual information registration to cancel the breathing and movement errors. At the third step of the image analysis framework, first the kidney is segmented from the abdomen scan, then it is segmented into the cortex and medulla compartments. For these segmentation steps, we developed a novel deformable model approach that incorporates both prior shape and gray level information. The basic steps of the segmentation approach are given in Fig. 6, and explained in detail in Chap. IV.

The segmentation framework starts by asking the user to select two images from the sequence: an early enhancement image where the medulla and cortex regions can be separated, and a late enhancement image where there are less jumps in the intensity inside the kidney.

Further, the user is also asked to select seed points from the medulla regions; which are used in initializing the deformable model in the segmentation steps. To segment the kidney from the abdomen images, a deformable model is evolved in the late enhancement image from the selected seed points. This deformable model evolves using the gray level information of the late enhancement image and a prior shape information calculated from a kidney database. The gray level information of the selected late enhancement image is obtained by estimating the density of the normalized histogram of the image in a 1D density function using a modified expectation maximization algorithm. The prior shape information is also a 1D density function, representing the density estimation of the signed distance maps of manually segmented and affinely registered kidney database. Figure 7 gives a glimpse to prior shape construction, which is given in more detail in Chapter 4, Section A.3.d.

With the two 1D density functions at hand, a deformable model is initialized in the kidney to grow depending on both the gray level information and the prior shape information. More details on the mathematics of this process is given in Chapter 4, Section A.3. With such a deformable model, initially, both the gray level information and the prior shape information pull the contour to grow. At the boundary points of the kidney, if there is a big discontinuity in the gray level information (i.e. strong edges), the gray level information forces the deformable model to stop. On the other hand, if the gray level is similar at the boundary points, the prior shape acts as the stopping term. In doing so, a connected kidney mask is obtained. At this stage, we would like to classify the kidney into cortical and medullary tissue. So another deformable model is let to grow in the medulla from the seed points, this time only with gray level information. Thus, the cortex and medulla are also segmented individually; we refer to these as the kidney mask.

At the final stage, the kidney mask is propagated over the whole sequence of scans. At the each scan, the mean gray level (intensity) values are calculated in the cortex and in the medulla, and these two mean values are plotted as a function of time, giving the cortical and medullary renograms. As a last step, the most important features in these renograms are extracted to diagnose the patients as normal or acute rejection. The details of this framework form the Chapters 3, 4 and 5.

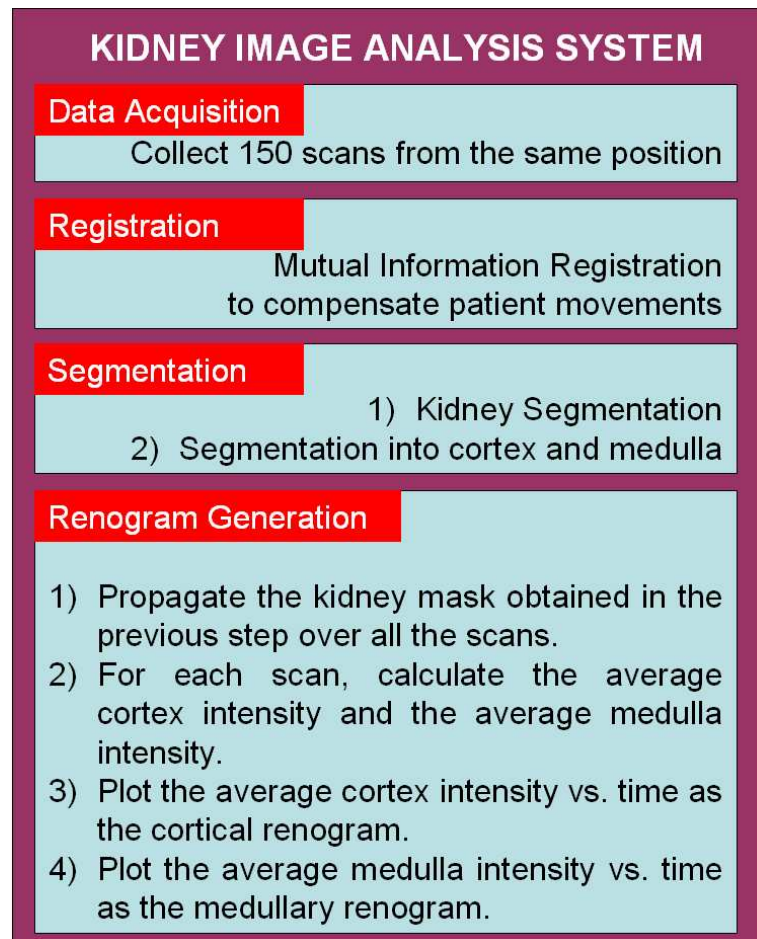


FIGURE 5 – The framework of the proposed system. After the image acquisition, the images are aligned using mutual information registration. Then the kidney is segmented from the abdomen images, and it is segmented further into cortex and medulla compartments. The segmented kidney mask is propagated over the whole sequence to get the average cortex and medulla intensity values; then these intensities are plotted as renograms; and the critical points in the renograms are used in the classification.

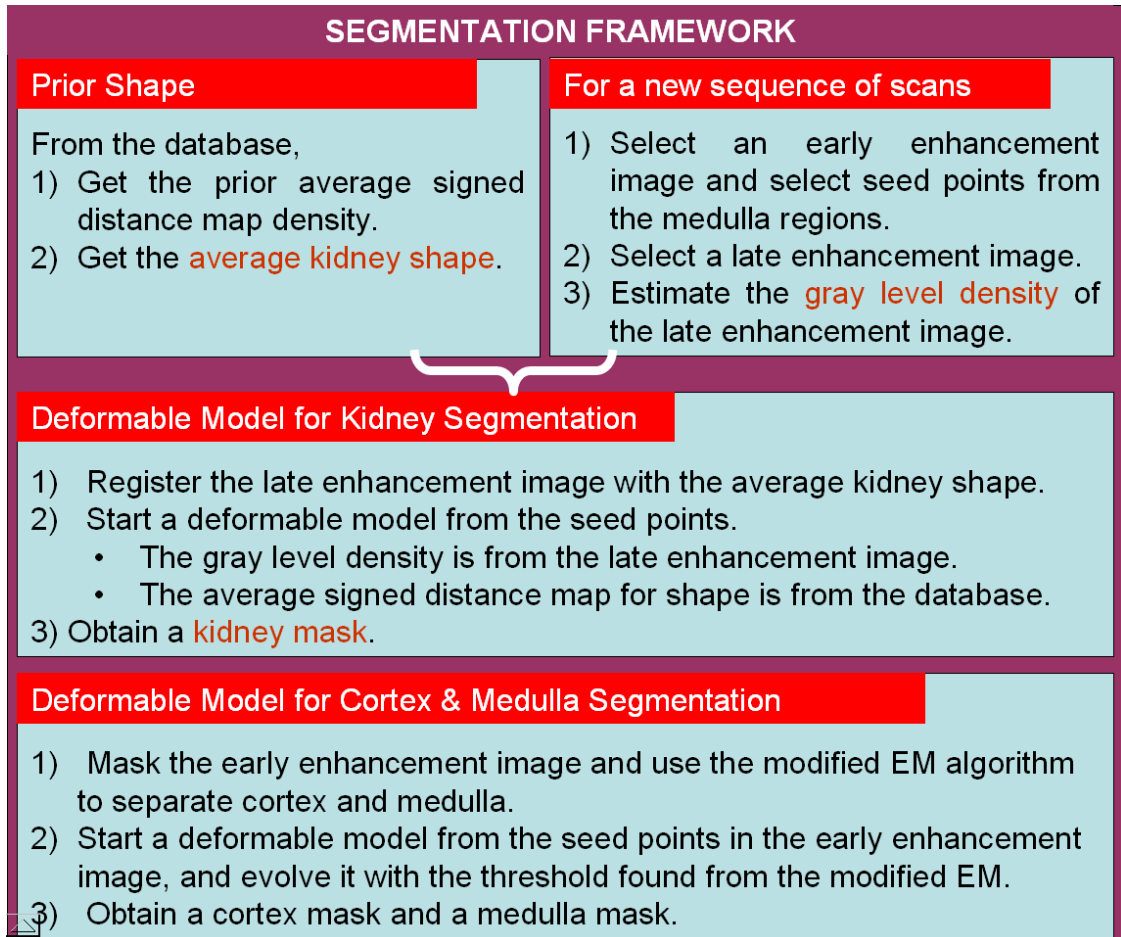


FIGURE 6–The segmentation framework of the proposed system. At the beginning of the segmentation framework, an average prior kidney shape and an average signed distance map density is obtained from previously segmented and aligned kidney images. For a new patient, the user selects a late enhancement image and seed points from an early enhancement image. The gray level density estimation of the late enhancement image is obtained via a modified EM algorithm, and it is combined with the average signed distance map density of the database to be used as the energy of a deformable model. By evolving the deformable model with prior shape and current gray level information, a kidney mask is obtained. The kidney region is further segmented into cortex and medulla compartments depending on the gray level density estimation of the kidney region in the early enhancement image.

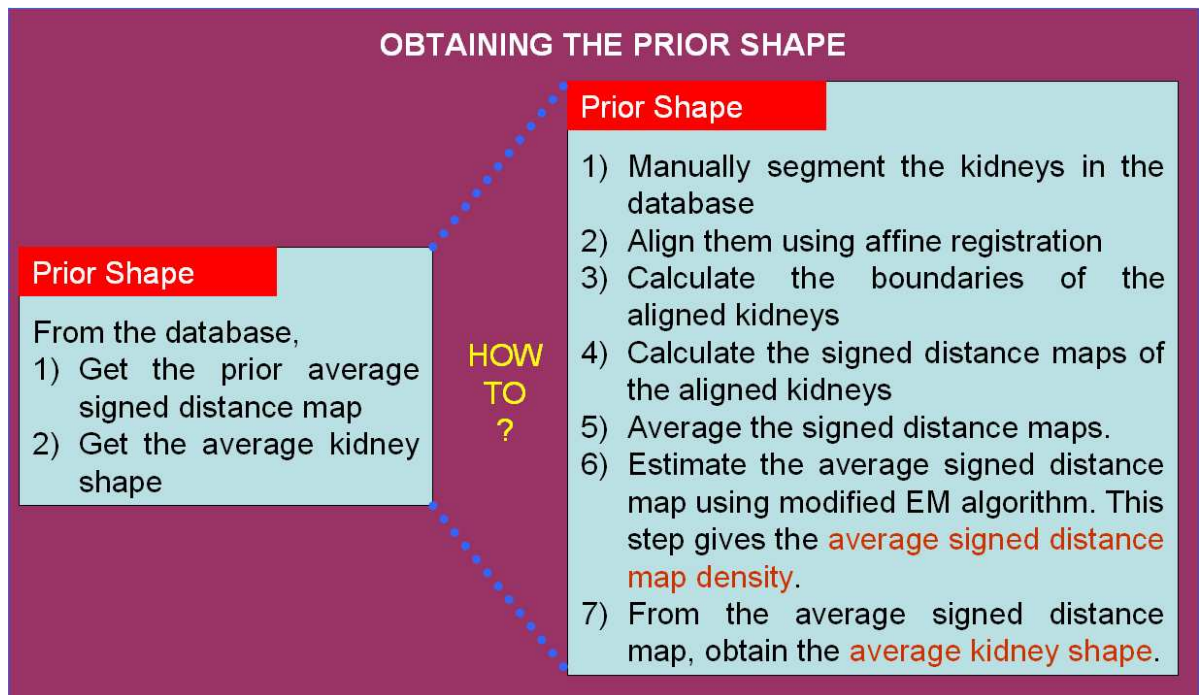


FIGURE 7—More detail on the steps to obtain the average shape for the segmentation framework. The kidneys are manually segmented from the abdomen scans, and they are aligned by affine registration. The signed distance maps of these binary images are calculated wrt. the kidney boundaries, and they are averaged to obtain the average signed distance map. From the average signed distance map, an average kidney shape is obtained (positive distances represent the kidney, negative distances represent the background). From the histograms of the signed distance maps, an average signed distance map density is obtained via a modified EM algorithm.

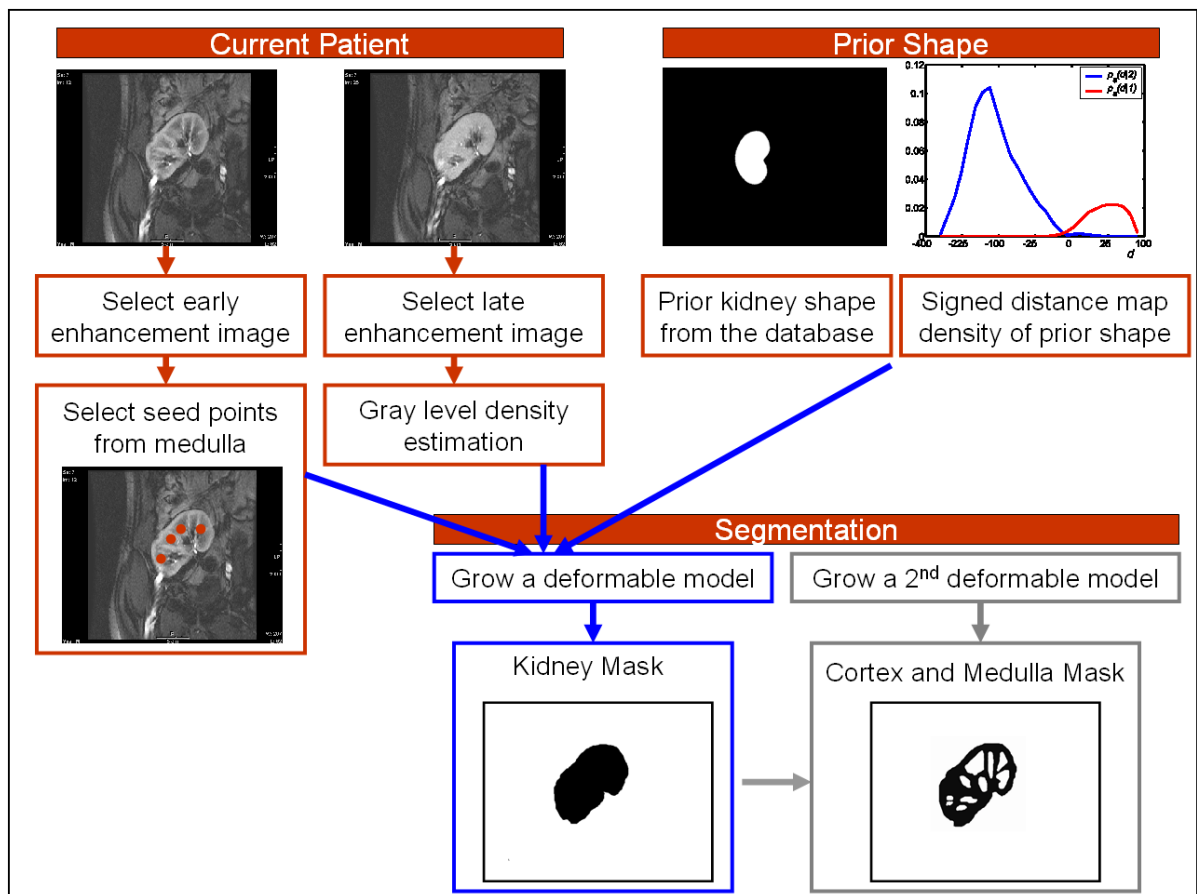


FIGURE 8–Segmentation framework illustration with images. An early enhancement image, seed points, and a late enhancement image are selected from the current patient. For kidney segmentation, a deformable model is initialized at the seed points to evolve with the gray level density estimation and the signed distance map density estimation of prior shape. With a second deformable model, cortex and medulla are extracted from the kidney region.

D. Outline of the Thesis

Chapter II of this thesis focuses on the background information starting with the anatomy and the functions of the kidney. In Section B, the properties of the contrast agent Gd-DTPA is explained with relation to kidney anatomy and physiology, and the role of the contrast agent in DCE-MRI studies is discussed. This section is mostly medical terminology, but it would help the reader to understand the power of dynamic MRI as an imaging modality, and the basics that relate to the contrast patterns in dynamic MR images. In Section C, a discussion on the previous renal DCE-MRI studies is given, with particular attention to the state-of-the-art in computerized image analysis. In Section D, we give a note on the protocol selection, covering the experience obtained in selecting the current protocol.

In Chapter III, mutual information (MI) registration is introduced as a way to correct the motion of the kidneys that could occur due to the patient movement or breathing. An overview of MI is given in Section A with implementation details; a validation approach is demonstrated in Section B on synthetically created kidneys via inverse mapping, and the results on real kidney transplants are given in Section C. Chapter III is concluded with a discussion on the results in Section D.

Chapter IV explains the segmentation of the kidneys from the other structures, as well as the segmentation of the cortex and medulla from the kidneys. In Section A.1, a popularly used method of image subtraction and connected component analysis is discussed. To improve its results, in Section A.2, an introduction to deformable models is given and their limitations are discussed. More information on deformable models is also given in Appendices II, III and IV. In Section A.3, a new segmentation approach is introduced, and in Section B, the kidney is further segmented into the cortex and medulla structures. Section C shows these segmentation results.

Chapter V focuses on the detection of dysfunction and the classification of the diseases. For this purpose, mean signals obtained from the cortex and medulla structures are plotted over time, and several features are extracted from these curves for classification.

The thesis is concluded in Chapter VI, with an overview of the thesis and snapshots from the prepared software, discussions on how to improve the results and on how to apply these techniques to medical practice.

CHAPTER II

BACKGROUND

The power of Dynamic Contrast Enhanced Magnetic Resonance Imaging (DCE-MRI) stems from the use of the contrast agent which brings both the anatomical and the functional information into the process. Therefore, the use of this imaging modality is best understood if one knows about the working principles of the contrast agent and its relations to the anatomy and physiology of the kidney. As a result, this chapter starts with the necessary introduction to the anatomy of the kidney and the properties of the contrast agent with relation to the kidney anatomy and physiology. Following these basics, related work on renal DCE-MRI studies are introduced, and the limitations of these studies are discussed.

A. Anatomy and Functions of the Kidney

Kidneys are bean-shaped organs, located at the back of the abdominal cavity, one on each side of the spinal column, just below the rib cage [21] as shown in Fig. 9 [1]. Each kidney is about the size of a fist, but every day, they process about 200 quarts of blood to make the 2 quarts of waste products and extra water which becomes the urine [4]. It is the urine production that keeps the blood clean and chemically balanced, making the kidneys vital organs for the body.

Looking at a cross-section of a kidney as shown in Fig. 10 [2], three regions appear: the pelvis, the cortex and the medulla. Pelvis region is just the extension of the ureter into the kidney; whereas the cortex (outer portion) and the medulla (inner portion) are the two major anatomical regions. Cortex and medulla are made up of approximately 1 million tubular structures called nephrons, which are the functional units of kidneys, of length 45 to 65mm and width 0.05mm [22].

When blood enters the kidney, it goes to the nephrons in the cortex, where it gets

processed to form the urine. Once the urine is formed by several steps that occur in the cortex and the medulla, it escapes into the pelvis, from where it is transported with the ureter tubes to the urinary bladder and with the urethra to the external environment [21].

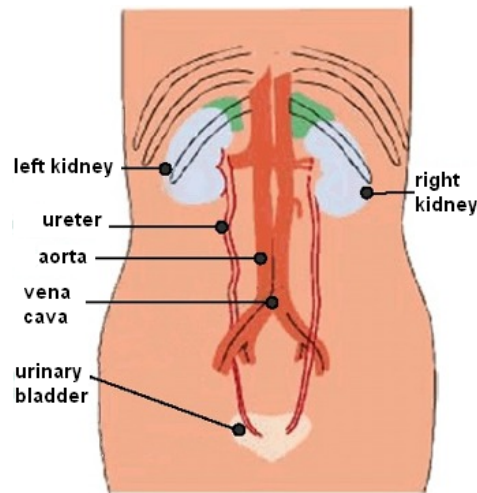


FIGURE 9: Location of a kidney [1]

In this big framework however, the actual process of forming the urine from the blood takes place in the nephrons. Each nephron consist of a glomerulus, its tubule and its blood supply as seen in Fig. 11. The tubule is also divided into four parts: Bowman capsule, proximal tubule, loop of Henle, and distal tubule.

Upon reaching the nephron in the cortex, blood first meets the glomerulus structure and the urine formation starts through three important processes. These processes are filtration by the glomerulus; reabsorption and secretion by the tubular cells. By these processes, the important products such as the amino acids and water in the body are conserved, whereas the metabolic wastes (urea, uric acid, creatinine, ammonia) are excreted out of the body.

The first process of the latter, the *filtration*, takes place in the glomerulus. Because of the differences in the blood pressure and the protein osmotic (oncotic) pressure, glomerulus functions as an ultrafilter and allows only small particles to enter the fluid that goes into the Bowman's capsule. Therefore, the fluid that goes into the Bowman's capsule does not contain the blood cells nor the proteins. From the Bowman's capsule, this filtrated fluid goes into the tubular cells where the necessary materials for the body such as glucose are actively transported back into the body. This active transportation is called *reabsorption*, and it helps to retain

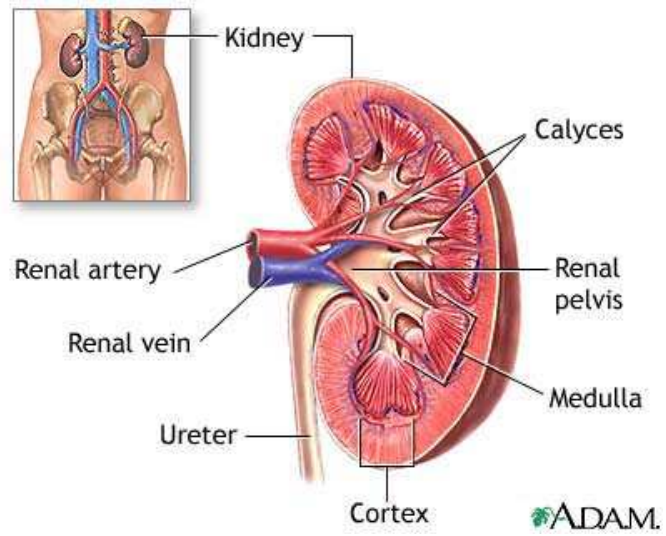


FIGURE 10–Anatomy of a kidney [2]

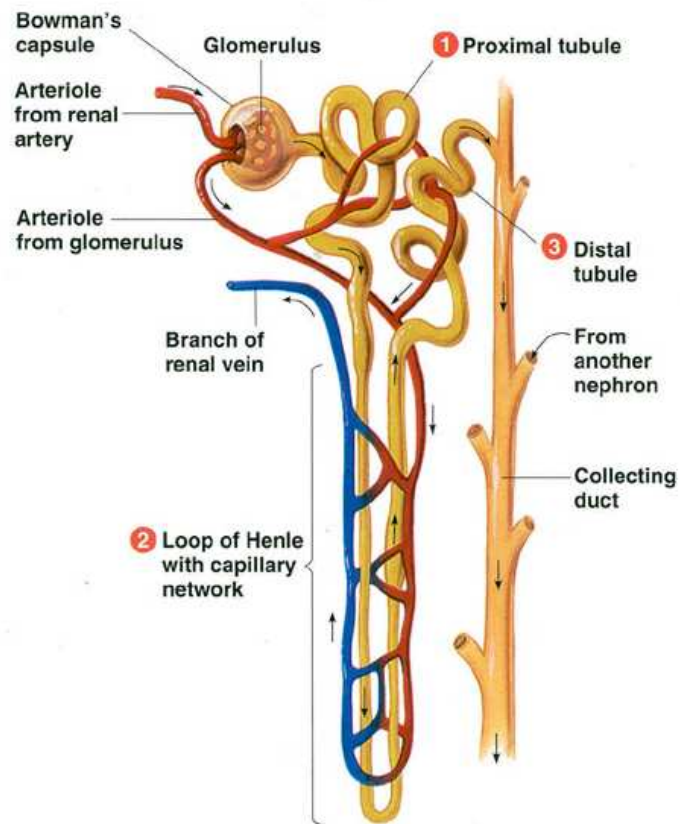


FIGURE 11: Structure of a nephron [3]

normal blood levels of necessary materials. Alternatively, some substances may be removed from the blood and added to the tubular fluids in a process called *secretion* [22]. At the end of these three steps, the urine of a healthy kidney should be protein and glucose free, and should not contain any blood cells.

B. Properties of the Contrast Agent Gd-DTPA

In DCE-MRI, the organ is scanned rapidly and repeatedly after the injection of a contrast agent. In this thesis, the contrast agent used for T1-weighted DCE-MRI is the Gadolinium diethylene triamine pentaacetic acid (Gd-DTPA); approved by the Food and Drugs Administration for clinical use.

Gadolinium diethylene triamine pentaacetic acid (Gd-DTPA) is a water soluble (hydrophilic), paramagnetic and non-nephrotoxic contrast agent which is freely filtered from the body, not secreted, reabsorbed nor metabolized in the body [23, 24]. Gd-DTPA, because of its paramagnetic property, possesses unpaired electrons. In an external magnetic field, the dipolar interaction between these unpaired electrons and the proton nuclear spins of the tissue produce a magnetic resonance signal. Consequently, the changing number of fluctuating magnetic fields near a nucleus cause a change in the T1 and T2 values. As a result, the addition of a small amount of Gd-DTPA greatly reduces the T1 relaxation times of the nearby tissue, and causes a corresponding signal increase in the T1-weighted MR images of the kidneys [8]. Using this signal increase, follow-up of the contrast agent concentration in a region of interest can be obtained.

The perfusion of the contrast agent to the kidney and the consequent contrast changes can be explained in 3 phases: vascular, tubular and ductal. In the vascular phase, Gd-DTPA enters the kidney with the renal vessels and gets filtered at the glomerulus where approximately 80% of the Gd-DTPA passes to the proximal convoluted tubule (PCT). At this phase, the Gd-DTPA concentration is dilute compared to the plasma, which causes a T1 shortening [25]. By T1 shortening, a rapid increase in the signal intensity occurs in the cortex of the kidney in MR images as illustrated in Fig. 12.

The contrast agent Gd-DTPA then moves to the descending limb of the loop of Henle (LOH) (tubular phase). In the descending limb, the water is reabsorbed back to the body,

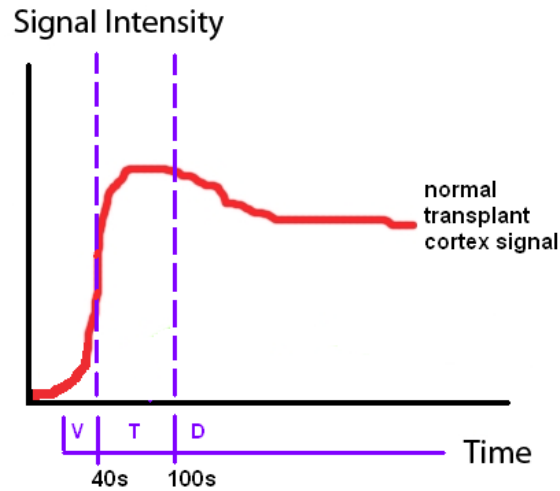


FIGURE 12–Ideal patterns of signal enhancement in the cortex of a normal transplant with $V = VascularPhase$, $T = TubularPhase$, $D = DuctalPhase$. The signal intensity increases immediately after the injection of the contrast agent in about 40 seconds, reaches a maximum within the first 100 seconds and starts to drop slowly to its initial value while the urine is formed.

so the Gd-DTPA concentration increases resulting in even brighter signals. Arriving at the ascending limb of loop of Henle and the distal tubules where water is not reabsorbed, the concentration of Gd-DTPA remains constant (however, the signal may not stay constant due to the combination of T1 and T2 shortening effects). Finally, the contrast agent Gd-DTPA passes into the collecting duct (ductal phase) and to the pelvis, from where it is excreted. In the ductal phase, the clearing of the contrast agent from the pelvis creates a decrease in the signal intensity [25]. This signal (i.e. contrast) increase/decrease pattern for the cortex of a normal transplant is illustrated in Fig. 12. In the perfusion curves, we normally expect the signal intensity to increase (while the contrast agent is passing through the cortex), and then a slight decrease (due to water reabsorption) followed by a constant signal (due to constant flow at the ascending distal tubule) and a decrease due to the washout of the contrast agent. In normal transplants, the signal intensity increases immediately after the injection of the contrast agent in about 40 seconds, reaches a maximum with the first 100 seconds and starts to drop slowly to its initial value while the urine is formed [18, 26].

The effect of the contrast agent on the medulla follows the patterns of the cortex with some delay since the contrast agent arrives at the medulla after a relatively slow filtration process that occurs in the cortex. Also, because of the reabsorption of water and secretion

processes in the tubules, the medullary signal curves show fluctuations different than the cortical ones [9, 27]. This behavior of the signals is a reflectance of both the anatomy and physiology of the kidney; which is why DCE-MRI is so powerful in kidney function evaluation.

C. Related Work in Renal Image Analysis Using DCE-MRI

Starting with the examinations on rats, studies on the kidneys to acquire functional, dynamic or anatomic information date back to the early 1980's, covering a variety of objectives from just understanding the normal behavior of a kidney to detecting its diseases. The potentials of DCE-MRI to understand kidney function have been investigated in various studies (see [11, 20, 23, 26, 28–37] to cite a few), and this imaging modality has been applied to various kidney diseases in several other studies, such as for the detection of renal ischemic lesions [38], for evaluation of renal failure [39], for acute tubular necrosis [40], for the assessment of chronic medical nephropathies [41], to differentiate obstructive from nonobstructive hydronephrosis [42, 43], to evaluate rejection [44], to differentiate acute tubular necrosis from transplant rejection in patients with delayed kidney function [24], to differentiate acute tubular necrosis from acute transplant rejection [18], for functional and morphological evaluation of live kidney donors [45], to study the renal function in the nephrolithiasis and hydronephrosis diseases [26], to observe the effect of hypertension on kidney function [46] and for the evaluation of normal and transplanted rat kidneys [16].

These studies are significant, as they have ascertained DCE-MRI as a very promising technique not only to assess renal blood flow and consequently understand kidney function, but also to evaluate several clinical disorders. However, most of these studies were performed by radiologists by selecting a region of interest (ROI) (a small window) from the kidney and following the signal change in this region of interest. Unfortunately, such approaches not only require manual interaction of the operators, but also the ROI selection biases the final decision and brings the same issue of over or underestimating the problem in the entire graft, just like in biopsy. Moreover, the manual window selection, and generating a function curve from this window over a time-sequence of images assumes that the kidneys (renal contours) stay exactly the same from scan to scan. However, renal contours may not always exactly match due to patient movements or breathing effects; therefore, image registration schemes should

be applied first before the ROI selection. Also, to automate the algorithm and to cancel the ROI dependency, segmentation algorithms that can separate the kidney from the surrounding structures, and that can further separate the kidney into its cortex and medulla compartments are needed. In the following parts of this section, previous computerized studies that make use of image processing techniques are discussed.

To our best knowledge, the first computerized renal image analysis scheme was developed by Gerig *et al.* [36] in 1992. In this study, the prior contour information for each study is obtained by manually drawing the contour from one image. For the rest of the images, image discontinuities (edges) are detected, and the model curve is matched to these edges using Hough Transform. To extend the algorithm to arbitrary rotation and translation, the model contour is rotated and translated to get the best correlation, giving the registration parameters of the image. The rotation in this scheme was limited to ∓ 4 degrees in 1 degree steps. For the cases of when the patient inadvertently moves or breathes, the detection of kidney contour was severely impeded, therefore, a 50% vote was defined, that is, at least 50% of the kidney needed to be detected for the registration to work. A similar procedure with some extensions was also used by Yim *et al.* in [33].

The handicaps of this image analysis scheme can be listed as (i) the need for manual selection of a contour for each study, (ii) the problems that could be faced in case of a larger movement by the patient, (iii) the great computational expense of Hough Transform (the algorithm was implemented in parallel in [36] and one patient took about an hour to evaluate). Moreover, this registration method is highly dependent on the edge detection filter. Although the strength of edge detection was increased by using an opposed-phase gradient echo imaging that puts a dark line between the water-based kidney and the perirenal fatty tissue; still, the algorithm worked better in smaller areas since increasing the field of view (FOV) parameter caused the algorithm to match more partial contours. Following this same procedure, healthy volunteers and hydronephrosis patients were compared in [26], and DCE-MRI was shown to be a reliable method for kidney analysis.

Noting the lack of special protocols and the consequent problems with edge detection in the registration process, the second image analysis study came from Giele *et al.* [37] for registration in 2001, where three movement correction methods were compared based on image

matching, phase difference movement detection (PDMP) and cross-correlation. In all these methods, a mask is generated from the best image manually, and its similarity to a given image is calculated. Consequently, the (x,y) values that give the highest similarity become the translation parameters for the given image. Among these methods, the PDMD method showed the best performance but only with an 68% accuracy compared to the radiologist's results. More importantly, in all these three registration algorithms, only translational motion was handled and rotational motion was not mentioned, the existence of which has been discussed in a number of studies (see [26, 27, 47]).

For the segmentation of the kidneys, Priester *et al.* in [48] subtracted the average of pre-contrast images from the average of early-enhancement images, and thresholded the subtraction image to obtain a black&white mask kidney image. Following this step, the objects smaller than a certain size were removed and the remaining kidney object was closed with erosion operations and manual interaction to get a kidney contour.

This approach was furthered by Giele *et al.* in [9], by applying an erosion filter to the mask image to get a contour via a second subtraction stage. The possible gaps in this contour were closed by a hull function to get the boundary of the kidney, then via repeated erosions applied to this contour, several rings were obtained, which formed the basics of the segmentation of the cortex from the medulla structures. Of course, in such a segmentation, the medulla structures were intermixed with the cortex structures, so a correlation study had to be applied to better classify the cortical and medullary pixels.

Also in 2001, Boykov *et al.* presented the use of graph cuts using Markov models in [49]. In this algorithm, each voxel is described as a vector of intensity values in time, and initially, several seed points are put on the objects and on the background to give user-defined constraints as well as an expert sample of intensity curves. These expert samples of intensity curves are used to compute a two dimensional histogram which would further be used as a data penalty function in minimizing the energy function in the Markov model. Although the results looked promising, this algorithm was tested only on one kidney volume, and manual interaction was still required.

Following these studies, computerized image analysis schemes for the registration and segmentation of kidneys were introduced by Sun *et al.* [16, 32, 34, 35, 47, 50] in a series of studies

performed on rats and human subjects. The study on humans ([32, 47]) made use of a multi-step registration approach. Initially, the edges are aligned using an image gradient based similarity measure considering only translational motion. Once roughly aligned, a high-contrast image is subtracted from a pre-contrast image to obtain a kidney contour; which is then propagated over the other frames searching for the rigid registration parameters (rotation & translation). For the segmentation of the cortex and medulla, the level sets approach of Chan et.al. [51] was used.

In most of these previous efforts, healthy transplants were used in the image analysis, so the edge detection algorithms were applicable. However, in the case of acute rejection patients, the uptake of the contrast agent is decreased, so edge detection algorithms generally fail in giving connected contours. Therefore, throughout this thesis, we will avoid edge detection schemes although their help is undeniable. Instead, we try to combine the use of gray level and prior shape information.

D. A Note on Protocol Selection

During the development of this thesis, several protocols were tested to obtain the best in terms of both temporal and spatial resolution. At the beginning of this study, our protocol involved 12 temporal sequences from 6 cross-sections. The images were taken at 5mm thickness with no interslice gap, repetition time (TR) 34 msec, field of view (FOV) 42x42 cm and the matrix 256x160. The first image was taken at 0 second of injection and then the imaging was repeated every 30 second for 11 times with the last image acquired 15 minutes after the start of injection. The images of that protocol for one patient is shown in Fig. 13. With such a small image size (256x160) for the whole abdomen, the kidney in the image were even smaller, giving problems in the image segmentation. More importantly, with this protocol, we were selecting the best cross-section to get the perfusion curves; however, the 30 sec. intervals between the image acquisition was forcing us to lose many important data points as shown in Fig. 14. In the second image taken at the 30th second, the contrast agent has reached the cortex and already perfused into it; so the intermediate intensity values are lost.

Modifying the previous protocol and testing the modifications, we have found a couple of important points to consider for best results:

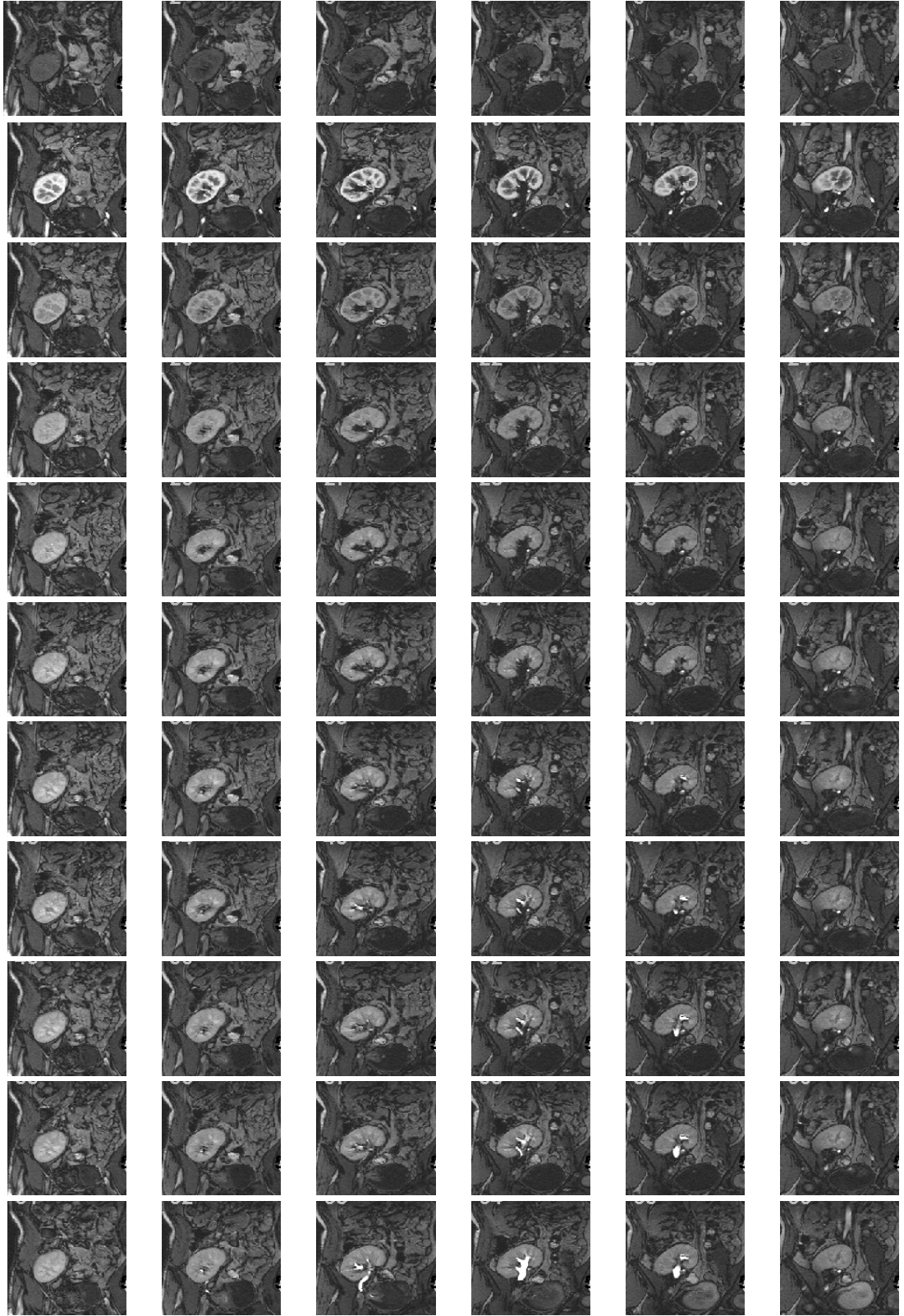
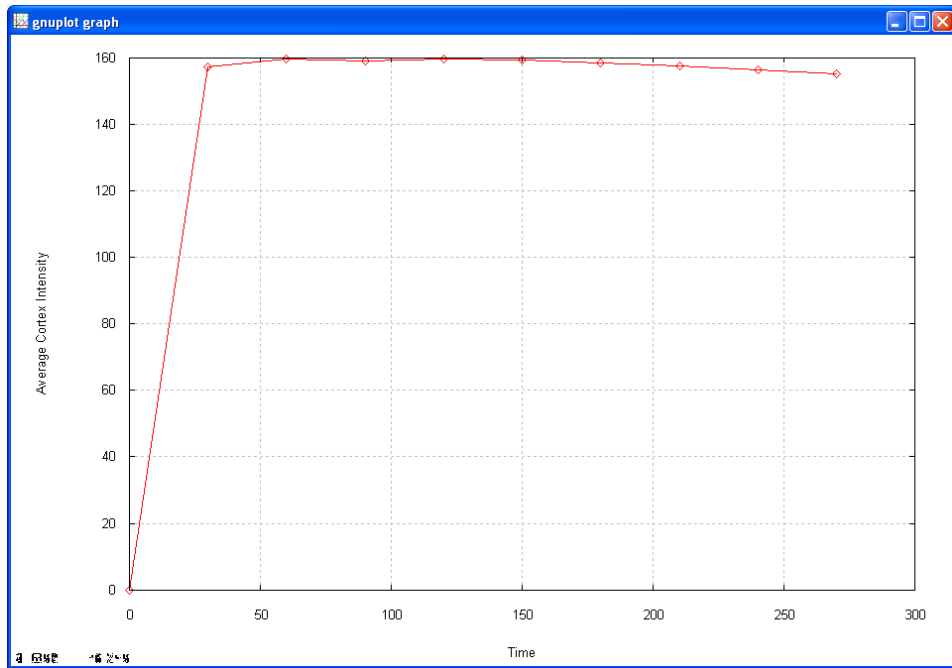
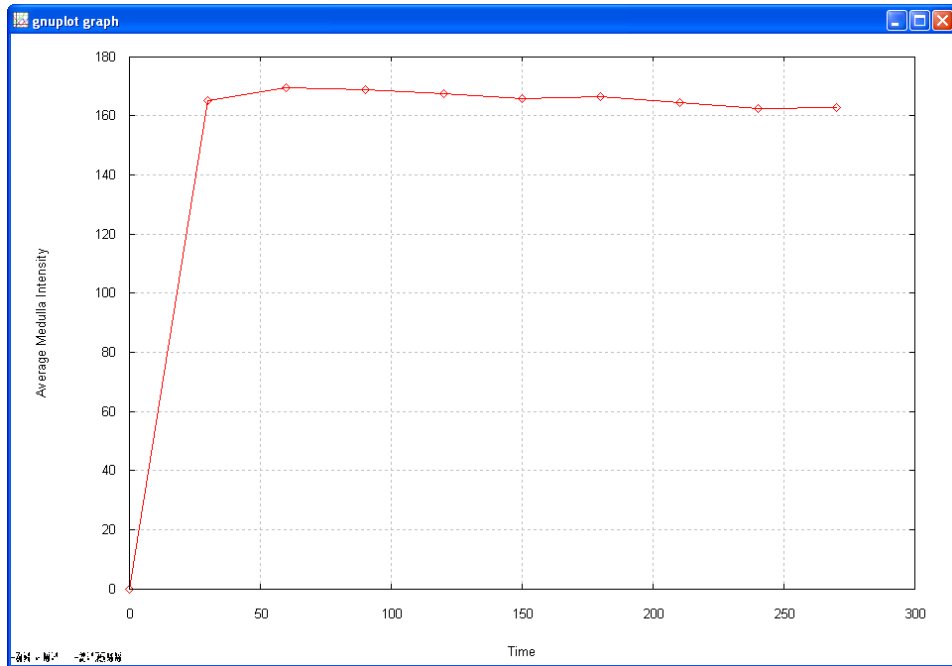


FIGURE 13—Old protocol. An example of the DCE-MRI series for one subject. For each subject, 6 cross-sections are taken with 30 second intervals.



(a)



(b)

FIGURE 14 – Old protocol perfusion curves for cortex (a) and medulla (b). There is a 30 second interval between each scan. At the 30th second (first scan), most of the important perfusion has already occurred so the important intermediate data is lost. Therefore, smaller time intervals are required between each scan.

- The most important characteristics of the signals in the cortex are seen in the first 40-100 seconds. This time interval corresponds to the time where the kidney first takes the contrast agent and passes it to the medulla. Therefore, as many as data points are needed within the first 100 seconds; of course, within the limits of the hardware, and also without compromising too much of the spatial resolution.
- To be able to use the general shape information of the kidneys, the sizes of the images should be fixed, and the FOV should not change from patient to patient.
- To allow automated comparison, the time difference between the scans and the number of scans in the sequence should be fixed.
- The perfusion time is in the order of minutes, so the number of scans should at least cover the first 4 minutes.

With these points in mind, our final protocol gets the scans of only one cross-section from the kidney (to decrease the amount of time spent between the scans), and the time between two scans is 4 seconds – the minimum amount of time that the MRI machine can get images. In the future, when fast image acquisition algorithms are implemented in MRI hardware, the cross-section number can be increased again, and volumetric signal measurements can be performed instead of the current 2D analysis.

CHAPTER III REGISTRATION

In Dynamic Contrast-Enhanced Magnetic Resonance Imaging of the kidney, a contrast agent is given to the patient, and the abdomen is scanned repeatedly and rapidly to observe the perfusion of the contrast agent into the kidney. However, during the scanning process, the patient breathes or moves unintentionally, so the position of the kidney can change from one scan to another. To perform an accurate slice-by-slice comparison of these images, the kidney images should first be aligned to each other. The alignment of two images is called registration, and if only translational and rotational movements are considered, the alignment process is called rigid registration. Figure 15 illustrates the two misaligned kidney images. The rigid registration scheme involves finding a geometric transformation between two images to align one of them to the other for easy comparison of these images; with the purposes of monitoring the changes in intensity over time.

The good news is, after kidney transplantation, the native kidneys are kept in place, and the new kidney is placed to the lower abdomen away from the diaphragm as shown in Fig. 16, thus the transplanted kidney does not show considerable motion due to breathing. The main

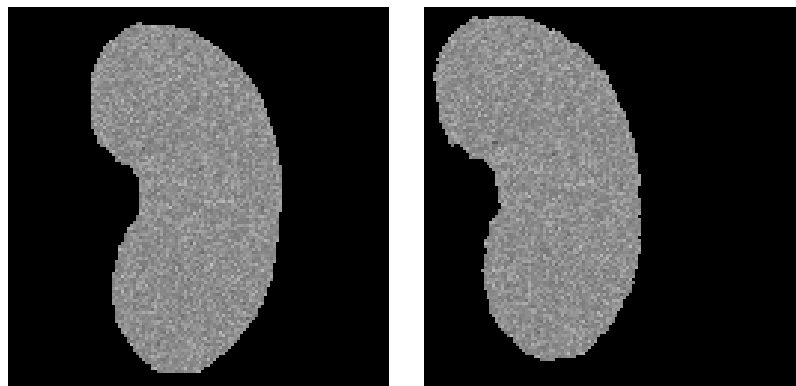


FIGURE 15–Illustration of the misalignment of two images. In these images, compared with one another, the anatomical structure is located at different positions. A rigid registration would translate and rotate the right image to align it with the left image.

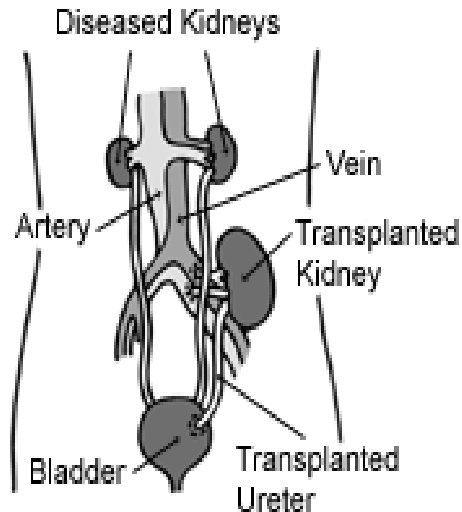


FIGURE 16–The transplanted kidney [4]. After kidney transplantation, the new kidney is placed to the lower abdomen; thus, the transplanted kidney does not show considerable motion due to breathing. The main motion it would experience is due to patient movement.

motion it would experience is due to patient movement; so if the patients are cooperative enough, registration step can even be skipped.

The bad news on the other hand is, if the patients are not cooperative enough and move during the scan, then there are a couple of points to consider in the registration; such as, there are no fiducial markers in the kidney to ease the registration, and not only the kidney moves during the image acquisition but also its intensity changes as the contrast agent perfuse into the cortex. To overcome these problems, rigid registration using mutual information (MI) has been proposed in this thesis to correct the movement of the kidney. Mutual information registration has been proved to align images from different modalities (such as MRI and CT) accurately and robustly [52], and thus, it has been able to handle the contrast change in the kidneys without any preprocessing step or feature extraction.

A. Mutual Information Metric

Mutual information (MI), first introduced by Collignon *et al.* [53] and Viola *et al.* [54] into a registration scheme, is a very general and powerful criterion for image registration as it does not require any assumptions, parameter tuning or limiting constraints, nor preprocessing, feature selection, or initialization of data [55]. Because of its robustness and generality, it has

been used in numerous applications, a survey of which is given in [56].

Mutual information measures the amount of information that one image A contains about the other image B calculated by the Kullback-Leibler measure:

$$I(A, B) = \sum_{a \in A, b \in B} p_{AB}(a, b) \log \frac{p_{AB}(a, b)}{p_A(a)p_B(b)} \quad (1)$$

where a and b are the gray values of images A and B with marginal densities $p_A(a)$ and $p_B(b)$, and $p_{AB}(a, b)$ is the joint distribution of the images' gray values.

In this formulation, if the images are independent, the $p_{AB}(a, b)$ can be written as a product of the marginal densities $p_A(a)$ and $p_B(b)$ giving a "1" in the division, and thus, because $\log(1) = 0$, the mutual information is zero for two statistically independent images. As a result, mutual information is said to measure the dependence of the two images, and it is maximized when there is a maximal dependence between the gray values of the images, i.e. when they are correctly aligned [56].

Another definition of the mutual information can be given using entropy where $H(A)$ and $H(B)$ are the marginal entropies of images A and B ; $H(A/B)$ and $H(B/A)$ are the conditional entropies; and $H(A, B)$ is the joint entropy of the combined images (A, B):

$$\begin{aligned} I(A, B) &= H(A) - H(A/B) \\ &= H(B) - H(B/A) \\ &= H(A) + H(B) - H(A, B) \end{aligned} \quad (2)$$

where the entropies are calculated as:

$$\begin{aligned} H(A) &= - \sum_{a \in A} p_A(a) \log p_A(a) \\ H(A|B) &= - \sum_{a \in A} \sum_{b \in B} p_{AB}(a, b) \log p_{A|B}(a|b) \\ H(A, B) &= - \sum_{a \in A} \sum_{b \in B} p_{AB}(a, b) \log p_{AB}(a, b) \end{aligned} \quad (3)$$

In its basic formulation of Eq. (3), two images are best aligned by a transformation function T when $I(A, B)$ is maximal. However, in the case of a misregistration, the MI may

still increase because of its sensitivity to overlap of the images. Therefore, a more robust mutual information measure named as the normalized mutual information has been proposed in [57] as:

$$NMI(A, B) = \frac{H(A) + H(B)}{H(A, B)} \quad (4)$$

As explained before, the more similar (i.e. the less independent) the images are, the lower the joint entropy compared to the sum of the individual entropies i.e. $H(A, B) \leq H(A) + H(B)$. Therefore, in either the classical MI formulation or in the normalized MI formulation, these formulations are maximized when $H(A, B)$ is minimized. By optimization, the translation and the rotation values that maximize the mutual information are found, and the corresponding following transformation gives the new (x, y) values:

$$\begin{bmatrix} x_{new} \\ y_{new} \end{bmatrix} = \begin{bmatrix} \cos(\theta) & -\sin(\theta) \\ \sin(\theta) & \cos(\theta) \end{bmatrix} \begin{bmatrix} x \\ y \end{bmatrix} + \begin{bmatrix} T_X \\ T_Y \end{bmatrix} \quad (5)$$

where θ is the rotation, T_X and T_Y are the translations.

For the sake of robustness, normalized MI metric measure is used in this thesis. To calculate Eq. (4), one has to calculate the joint densities in Eq. (3). Below, we explain the two ways of calculating the joint densities; density modeling via joint histograms and parzen windowing. These approaches have been very popular because they are non-parametric, i.e. they do not parameterize the data by assuming the data is from a certain family.

1. Density Modeling via Joint Histograms

Practically, each entry in the joint density $p_{AB}(a, b)$ can be calculated by counting the number of times an intensity a in image A coincides with an intensity b in image B ; and the marginal densities $p_A(a)$ and $p_B(b)$ are calculated by summing the joint density $p_{AB}(a, b)$ over a row or a column, respectively. To formulate this mathematically [58], the histogram of intensities for image A and B can be represented as:

$$\begin{aligned}
h_A(a) &= | \{x \mid A(x) = a\} | \\
h_B(b) &= | \{x \mid B(x) = b\} |
\end{aligned}
\tag{6}$$

From these histograms, one can form the joint histogram as:

$$h_{AB}(a, b) = | \{x \mid A(x) = a \text{ and } B(x) = b\} | \tag{7}$$

and calculate the empirical joint density by the normalization:

$$p_{AB}(a, b) = \frac{h_{AB}(a, b)}{\sum_{a' \in A, b' \in B} h_{AB}(a', b')} \tag{8}$$

Then the marginal probabilities can be recovered as:

$$p_A(a) = \sum_{b \in B} p_{AB}(a, b) ; \quad p_B(b) = \sum_{a \in A} p_{AB}(a, b) \tag{9}$$

And the conditional probabilities are obtained as:

$$p_{A|B}(a|b) = \frac{p_{AB}(a, b)}{p_B(b)} ; \quad p_{B|A}(b|a) = \frac{p_{AB}(a, b)}{p_A(a)} \tag{10}$$

These calculations are illustrated in Fig. 17 with two 5×5 images A and B composed of only 8 gray levels for simplicity. The darker parts of the images represent the translated object of interest. From these two images, a pixel by pixel comparison would give the joint histogram such as:

Pixel (1,1) in Image A has gray level 7,

Pixel (1,1) in Image B has gray level 4,

So Entry (7,4) in the histogram should be increased by 1.

Pixel (2,3) in Image A has gray level 1,

Pixel (2,3) in Image B has gray level 5,

So Entry (1,5) in the histogram should be increased by 1.

Once the joint histogram is obtained, the joint density is calculated by dividing the joint histogram by the size of the image as shown in Fig. 18; and the marginals are calculated by the summation of the joint density over a row or a column as given in Fig. 19.

2. Density Modeling via Parzen Windowing

Another frequently used method of density estimation is Parzen windowing. In Parzen windowing, an intensity samples S of size N_s is drawn from the image. Then, the probability $p(a)$ of a is the sum of the contributions of each sample from S to $p(a)$ in accordance with its distance from a . The Parzen estimate can be written as a sample mean with the following equation:

$$p(a) = \frac{1}{N_s} \sum_{s_j \in S} K(a - s_j) \quad (11)$$

where K is generally a Gaussian kernel.

For example, if we take a sample $S = \{1, 5, 6, 9\}$ of size $N_s = 4$, and use a Gaussian kernel $K = \mathfrak{N}(0, \psi)$ with $\psi = 0.09$ then the probability of intensity 2 would be, $p(2) = \frac{1}{4\sqrt{2\pi\psi}} e^{-\frac{(2-1)^2}{2\psi}} + e^{-\frac{(2-5)^2}{2\psi}} + e^{-\frac{(2-6)^2}{2\psi}} + e^{-\frac{(2-9)^2}{2\psi}} = 0.0012852$.

To calculate the entropy, another intensity sample R of size N_r is drawn from the image, and the entropy is calculated with the following equation:

$$H(a) = \frac{1}{N_r} \sum_{r_j \in R} \log p(r_j) \quad (12)$$

In comparison to the previously discussed histogram technique, Parzen windowing gives a smooth solution to the density estimation. However, if the variance ψ is selected to be too large, then important modes in the density may be filtered out during smoothing. Likewise, a small variance value results in a noisy density estimate.

IMAGE A					IMAGE B				
7	5	5	6	7	4	4	5	6	7
7	1	1	2	6	5	7	5	5	6
6	3	1	1	5	6	7	1	1	2
5	1	2	3	4	6	6	3	1	1
5	6	4	4	4	6	5	1	2	3

JOINT HISTOGRAM

		Gray Values of B							
		0	1	2	3	4	5	6	7
Gray Values of A	0	0	0	0	0	0	0	0	0
	1	0	2	0	0	0	1	1	1
	2	0	0	0	1	0	1	0	0
	3	0	1	0	0	0	0	0	1
	4	0	2	1	1	0	0	0	0
	5	0	0	1	0	1	1	2	0
	6	0	0	0	0	0	1	3	0
	7	0	0	0	0	1	1	0	1

FIGURE 17–Calculating the joint histogram from the occurrence of gray levels.

JOINT DENSITY

0	0	0	0	0	0	0	0
0	0.0032	0	0	0	0.0016	0.0016	0.0016
0	0	0	0.0016	0	0.0016	0	0
0	0.0016	0	0	0	0	0	0.0016
0	0.0032	0.0016	0.0016	0	0	0	0
0	0	0.0016	0	0.0016	0.0016	0.0032	0
0	0	0	0	0	0.0016	0.0048	0
0	0	0	0	0.0016	0.0016	0	0.0016

FIGURE 18 – Calculating the joint density from the joint histogram by normalization.

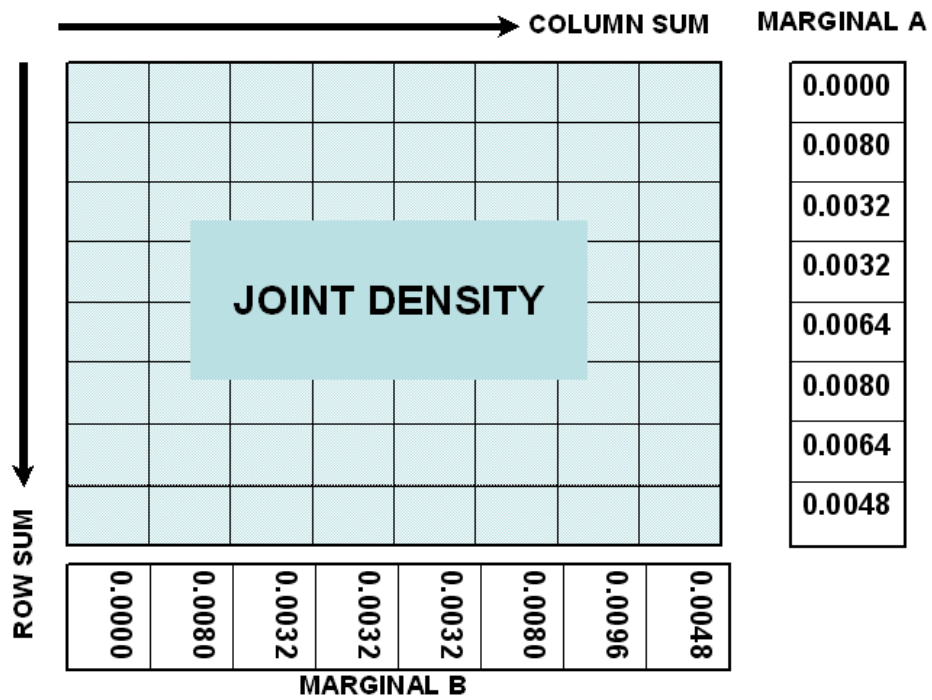


FIGURE 19 – Calculating the marginal densities from the joint density by summing over the rows and columns.

3. Implementation Issues

In the implementation of mutual information, initially, Matlab programming environment was used. In our Matlab code, we modelled the densities with joint histograms, and used genetic algorithms as the search method. However, due to the noise in the joint histograms and the slow nature of genetic algorithms combined with the slow computations of Matlab, the registration algorithm took hours to evaluate. More information on genetic algorithms and details on the parameter settings are given in appendix I (also see [59–66]).

For efficiency, the code was converted into C++ using Viola *et al.* approach [54] (uses parzen windowing for density estimation and gradient descent as the search method), and with the use of ITK libraries [67], the algorithm took only seconds. For the implementation of Viola’s approach, there are a couple of important parameters that need to be selected. Such as, it is common practice to smooth both the images with Gaussian kernels; we selected the variance of these blurring filters to be 2.0 for both images. Also, for the gradient descent optimization the step size (learning rate) is important; i.e., the optimizer becomes unstable if it is selected too large, or it requires more iterations and takes too much time if it is selected too small. In our tests, because of the noisy nature of the images, we tried to keep the learning rate small (0.02) and selected the number of iterations to be 500.

Another important parameter is the number of randomly selected samples from an image for the Parzen windowing as discussed in the previous chapter. If the sample size is selected large, the metric is smoother from one iteration to another; but at the expense of longer computation times. In our implementation, we found *number of samples* = 500 and $\psi = 0.4$ to be reasonable approximations. The current selection of the parameters is listed in Table 1; all of these parameters are adjustable in the prepared GUI (Graphical User Interface) for this thesis, so depending on the quality of the registration, the registration can be iterated easily with new parameters.

B. Validation of Registration

To validate the registration results, we generated realistic phantom images with known translation and rotation parameters, and registered these phantoms to each other. The phan-

TABLE 1
MUTUAL INFORMATION REGISTRATION PARAMETERS

Fixed Image		Moving Image		Number of Spatial Samples	Learning Rate	Number of Iterations
Standard Deviation	Smoothing Variance	Standard Deviation	Smoothing Variance			
0.4	2.0	0.4	2.0	500	0.02	500

tom kidneys have the medulla and cortex structures as in real kidneys; the gray levels of these structures and the background resemble the noise and intensity levels of the original images via the inverse transform method. The inverse transform method takes the densities (normalized histogram) of the cortex, medulla and background as the input, and generates random variables from these densities with similar distributions. These random variables become the gray level values in the phantoms.

To generate a continuous random variable $X \sim F$, the inverse transform can be stated as:

- 1) Generate a uniform random variable U .
- 2) Set $X = F^{-1}(U)$ (where $F^{-1}(x)$ is assumed to exist).

To apply the inverse transform for a discrete random variable $X = \{X_1, X_2, \dots, X_n\}$, the second step is modified as: $\{X = x_j\}$ if $F_X(x_{j-1}) \leq U < F_X(x_j)$.

A pseudo-code for the inverse mapping algorithm for the discrete case is given below:

INVERSE MAPPING ALGORITHM:

BEGIN

Obtain cumulative distribution F from the object of interest

DO

For each pixel $(k1, k2)$ in the region of interest of the mask image

Get $U = \text{rand}()$

find *NumberOfPixels* such that $F \leq U$;

Output_Image($k1, k2$) = *NumberOfPixels*

RETURN Output_Image

END

For validation, we generated realistic phantoms in 3 steps. In the first step, three images with well identifiable cortex and medulla structures were chosen from one patient as shown in Fig. 20 (a, b, c): the first image of his/her sequence, an early enhancement image, a late enhancement image. From these images, the second image (b) was used as a mask, and it was transformed with several rotations and translations as shown in Fig. 21.

In the second step, gray level intensities of the three images were calculated (Fig. 20 (d – f)), and cumulative distribution functions (CDF’s) were obtained (Fig. 20 (g – i)). In the third step, we obtain the realistic phantoms via inverse mapping, using the CDF’s obtained in Step-2. To obtain these phantoms, for each pixel in the mask, a random variable is generated in accord with the distributions calculated in Step-2 (inverse mapping method); which forms the gray level of the phantom images. An example of the phantom images for zero rotations and translation is given in Fig. 20 (j, k, l). In the same way, all the other rotated and translated mask images in Fig. 21 are filled separately with random variables obtained via inverse mapping from the gray level CDF. The set of images generated based on the first image of the sequence (Fig. 20(a)) is shown in Fig. 22; and the set of images generated based on the second image of the sequence shown in Fig. 20(b) is given in Fig. 23.

Finally, all the test images given in Fig. 22 and Fig. 23 were registered to Fig. 20(l). The original rotation and translation values and the estimated results using mutual information registration are given at Tables 2 and 3. The first three columns of these tables show the original transformations, the next three columns are the results obtained by mutual information registration, and the last column is the normalized MI metric (i.e. the similarity measure of the registration). In the tables, we refer to Fig. 20(l) as the reference image.

In the first table (Table 2), mutual information registration is able to handle the transformations with subpixel accuracy for small translations and rotations. For bigger transformations, it deviates with a couple of pixels; but this error in accuracy can easily be handled by decreasing the learning rate of the optimizer and by increasing the number of iterations. In our validation tests, the iterations were limited to 300 only. In the second table (Table 3), the results are still acceptable for small translations and rotations; but again with higher translations and rotations, the MI metric starts to decrease in accuracy. However, in practice, the

TABLE 2
REGISTRATION OF TEST SEQUENCE 1 TO THE REFERENCE IMAGE:
ROBUSTNESS TO TRANSLATION (IN PIXELS) AND ROTATION R (IN DEGREES).

Original			Estimated			MI
R	Translation X	Translation Y	R	Translation X	Translation Y	Metric
0	0	0	-0.13	0.29	0.57	0.43
0	5	0	0.24	5.59	0.09	0.44
0	0	5	0.06	-0.52	5.25	0.44
5	0	0	5.46	-0.69	-0.24	0.44
5	5	0	5.10	4.69	0.30	0.43
5	0	5	5.10	4.69	0.30	0.43
5	5	5	5.16	5.08	5.07	0.43
10	0	0	9.84	-0.50	-0.05	0.44
0	10	10	0.18	9.78	9.75	0.43
10	5	5	10.23	5.10	5.34	0.38
10	10	10	10.04	8.01	11.64	0.44
0	20	20	-0.13	20.16	20.05	0.43
10	20	20	10.11	16.61	22.80	0.43

accuracy of the approach at larger translation and rotation values is not very important as the transplanted kidney is not subject to large movements. Yet, in spite of the noisy nature of the images and low contrast, mutual information registration gives very satisfactory results without the need of any manual correction or parameter tuning (note that one can always set the number of iterations to a very high value and the learning rate to a very small value and no further parameter tuning will be required, but at the expense of speed.)

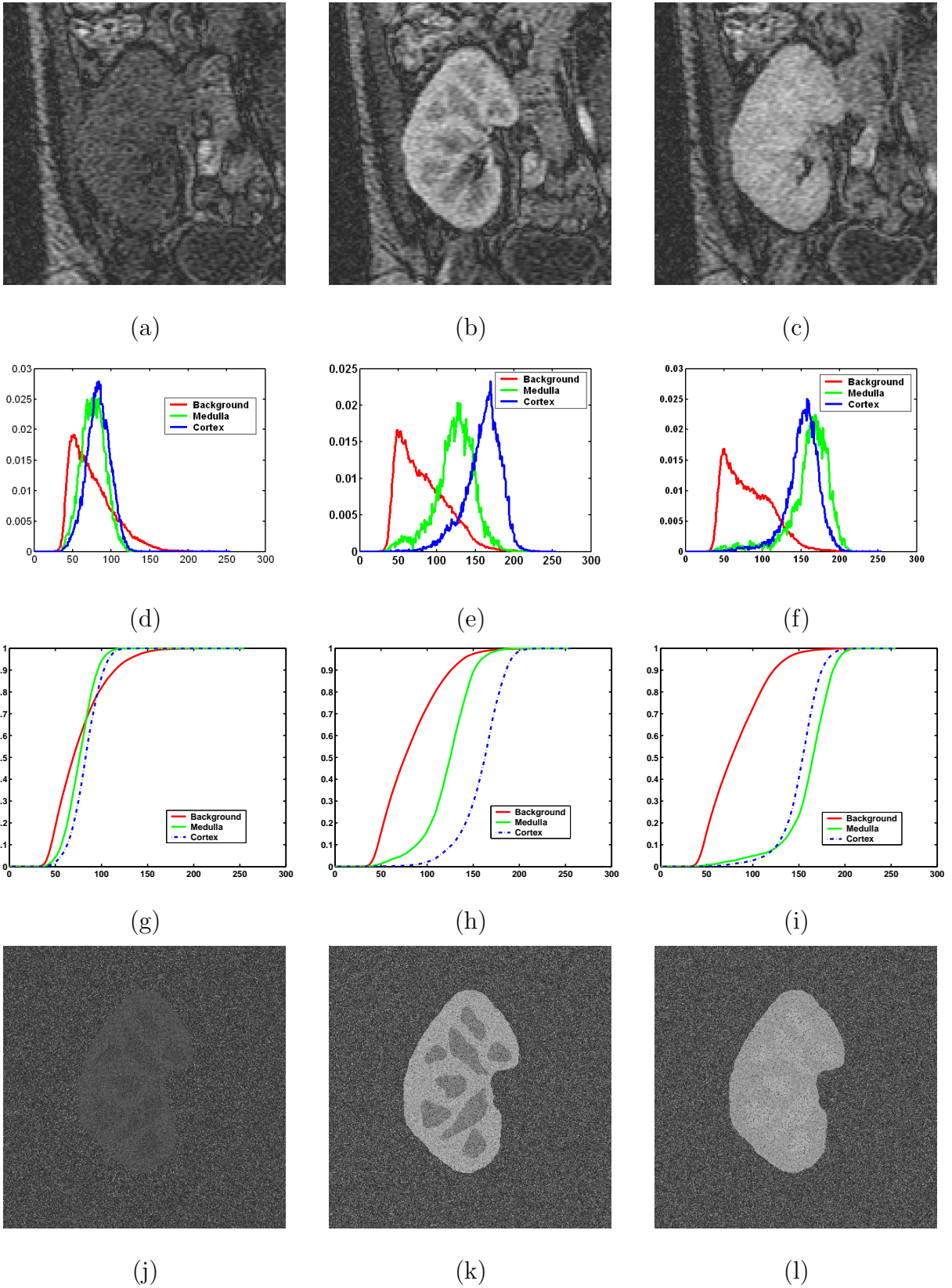


FIGURE 20: Three images from a sequence (a, b, c), their gray level densities (d, e, f) and the cumulative distributions (CDF's) (g, h, i). A mask is obtained from (b), and by inverse mapping, the test images (j, k, l) are obtained for zero translation and rotation.

TABLE 3
REGISTRATION OF TEST SEQUENCE 2 TO THE REFERENCE IMAGE:
ROBUSTNESS TO TRANSLATION (IN PIXELS) AND ROTATION R (IN DEGREES)

Original			Estimated			MI
R	Translation X	Translation Y	R	Translation X	Translation Y	Metric
0	0	0	0.33	-0.35	-1.94	0.02
0	5	0	-1.85	5.54	0.36	0.02
0	0	5	1.33	-1.65	3.81	0.01
5	0	0	2.03	0.01	0.46	0.02
5	5	0	3.24	5.78	1.25	0.02
5	5	5	6.14	6.71	6.30	0.02
10	0	0	6.35	2.02	-0.87	0.02
0	10	10	1.31	8.27	6.01	0.02
10	5	5	6.77	3.57	3.83	0.02
10	10	10	9.82	11.22	9.61	0.02

C. Registration Results

With the observation that mutual information registration gives satisfactory results on phantom images, the registration technique has been applied to real abdomen images and visually tested by checkerboards as shown in Figs. 24 and 25. A checkerboard image is basically obtained by patching one square region from fixed image and another square region from the moving image after registration, and these patches are visualized in one checkerboard image. In a checkerboard image, the expectation is to see continuous contours, which was well observed in our resulting checkerboard images. Had edge based registration been applied to Fig. 25, the double contours around the kidney and the edges of the arteries (bright in (a), dimmed in (b)) would have given problems.

D. Summary

In this thesis, normalized mutual information metric is used as the fitness function of the mutual information registration. Normalized mutual information measures the statistical dependencies between the intensity distributions in both images rather than the actual intensity values themselves. This important property enables the solution to our registration problem as the algorithm is not affected by the image intensity changes due to the contrast agent perfusion.

However, the relatively high noise in the images can sometimes be a problem. With increased noise, the entropy can be determined by the noise instead of the original signal, affecting the performance of the MI registration. To minimize such problems, before we start the registration, we select a small region of interest which includes mostly the kidneys, and perform the random sample selection from this region only. As a result, for small transformations, which is the case with transplanted kidneys, we were able to obtain fairly good registrations.

Two other components of our MI registration scheme are gradient descent method for optimization, and nearest neighborhood for the interpolation. By nearest neighborhood interpolation, compared to other interpolation techniques such as B-splines or linear interpolations, the addition of non-existing intermediate gray level values is avoided. When an accurate registration is accomplished, quantitative comparison of the intensity enhancement in the scans showing the perfusion of the contrast agent is enabled, allowing a better diagnosis for renal rejection.

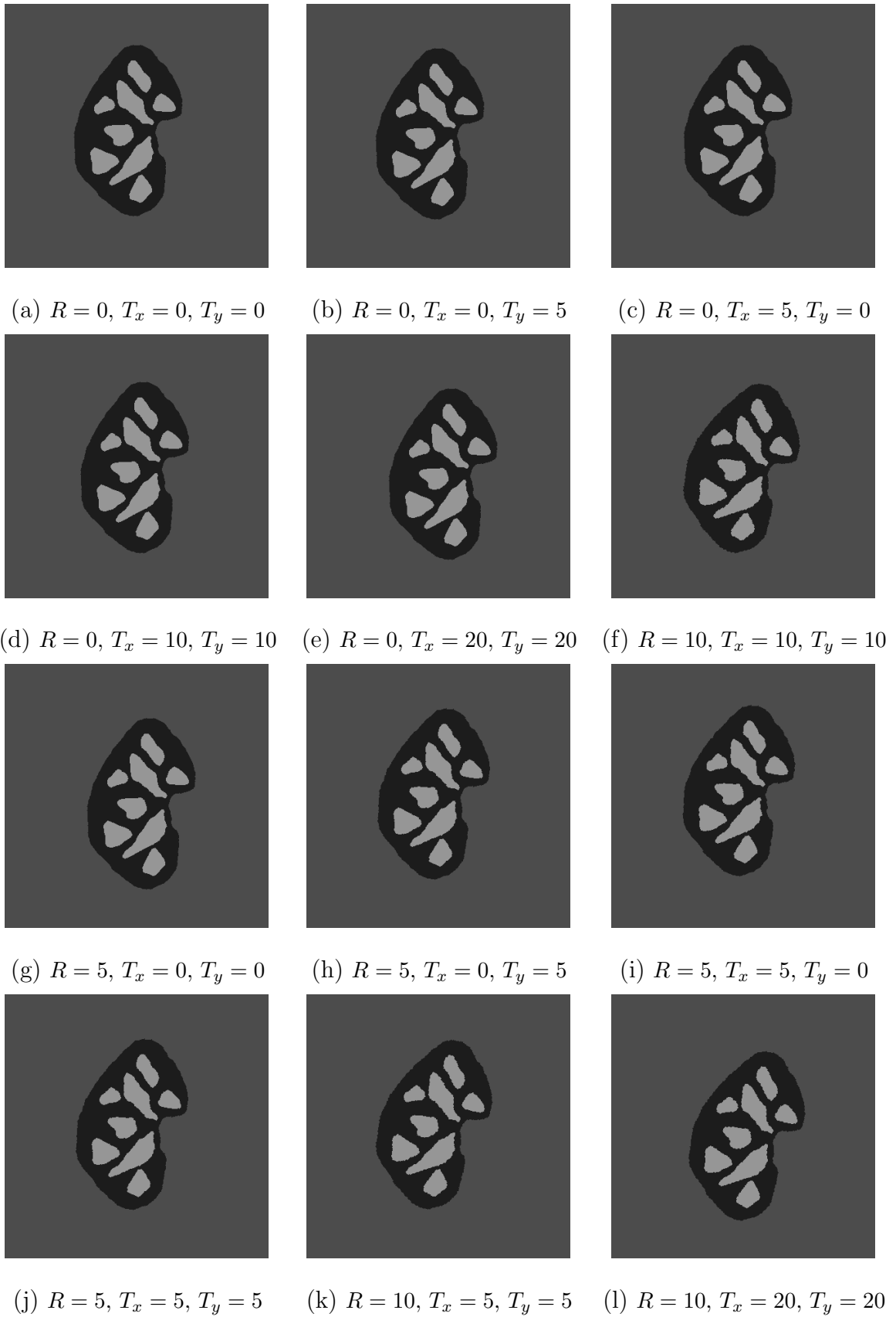
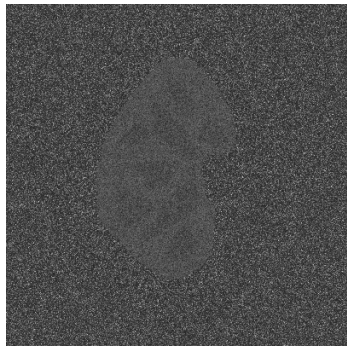
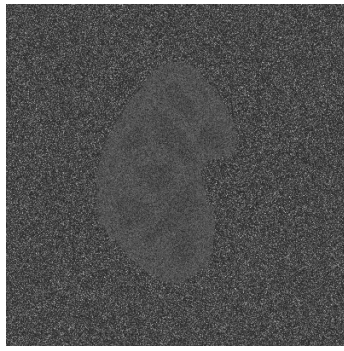


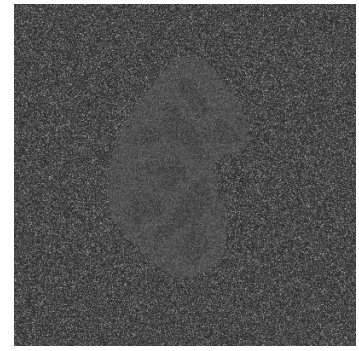
FIGURE 21: A mask image is generated manually based on the real kidney image in Fig. 20(b). This mask is transformed with various rotations (R in degrees) and translations in x direction (T_x) and in y direction (T_y) in pixels.



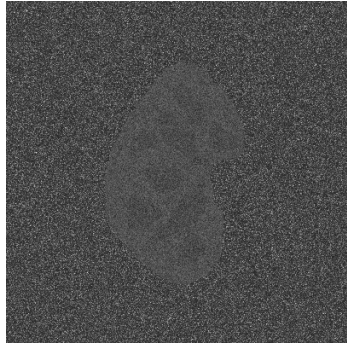
(a) $R = 0, T_x = 0, T_y = 0$



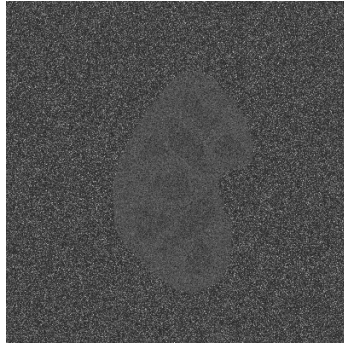
(b) $R = 0, T_x = 0, T_y = 5$



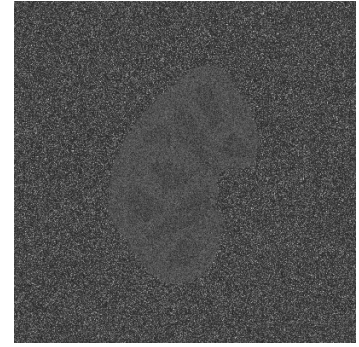
(c) $R = 0, T_x = 5, T_y = 0$



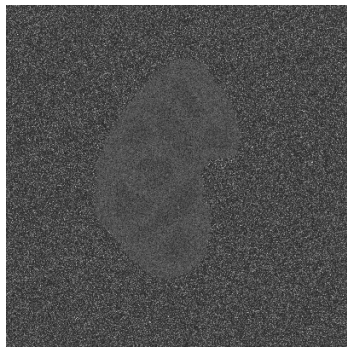
(d) $R = 0, T_x = 10, T_y = 10$



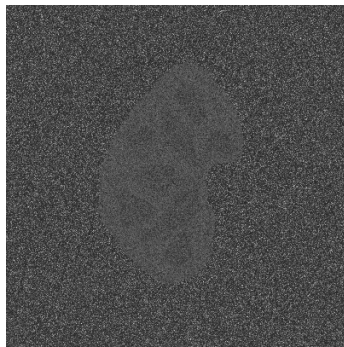
(e) $R = 0, T_x = 20, T_y = 20$



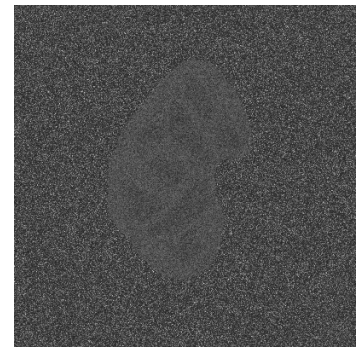
(f) $R = 10, T_x = 10, T_y = 10$



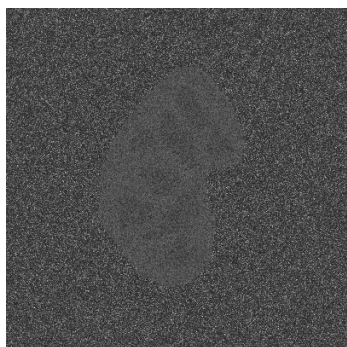
(g) $R = 5, T_x = 0, T_y = 0$



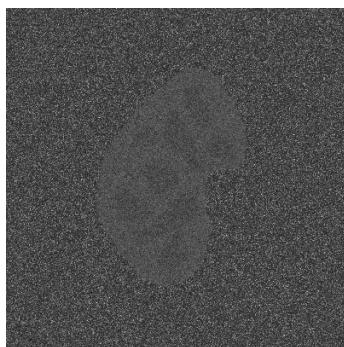
(h) $R = 5, T_x = 0, T_y = 5$



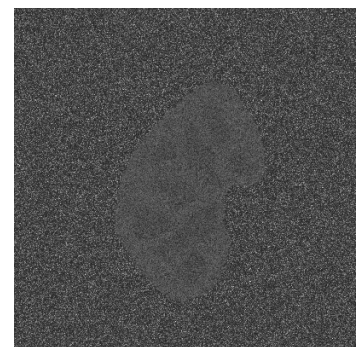
(i) $R = 5, T_x = 5, T_y = 0$



(j) $R = 5, T_x = 5, T_y = 5$

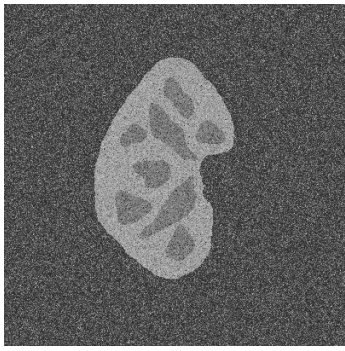


(k) $R = 10, T_x = 5, T_y = 5$

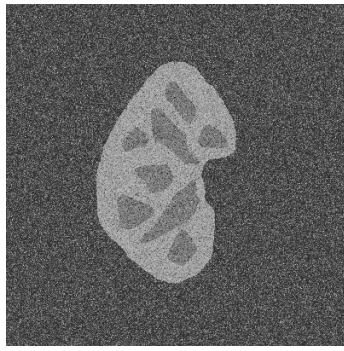


(l) $R = 10, T_x = 20, T_y = 20$

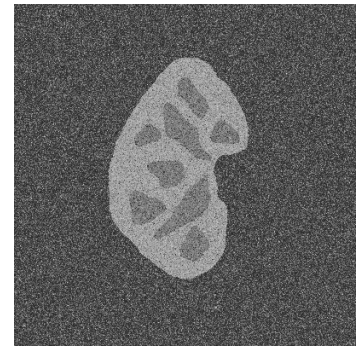
FIGURE 22: Test Sequence 1. Background, cortex and medulla structures in the mask are filled separately with random variables obtained via inverse mapping from the gray level CDF's (Fig. 20(g)) of Fig. 20(a).



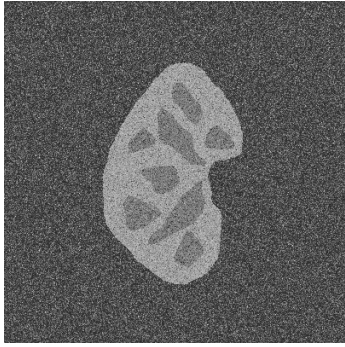
(a) $R = 0, T_x = 0, T_y = 0$



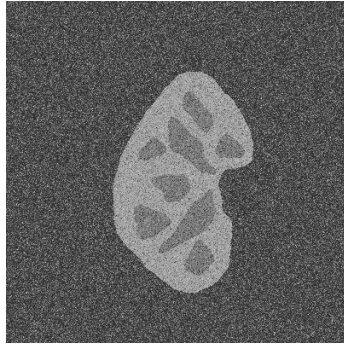
(b) $R = 0, T_x = 0, T_y = 5$



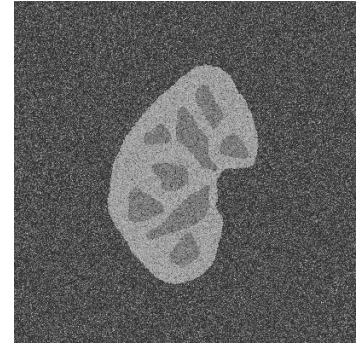
(c) $R = 0, T_x = 5, T_y = 0$



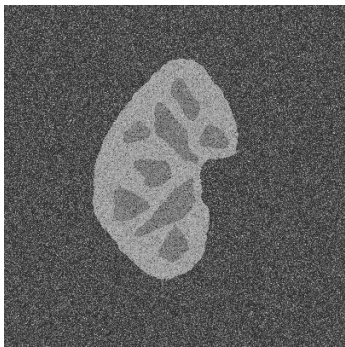
(d) $R = 0, T_x = 10, T_y = 10$



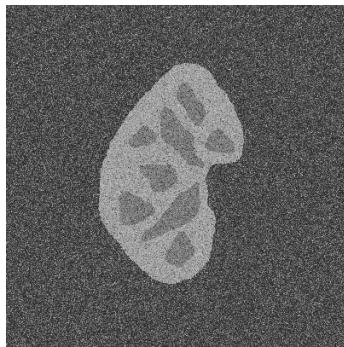
(e) $R = 0, T_x = 20, T_y = 20$



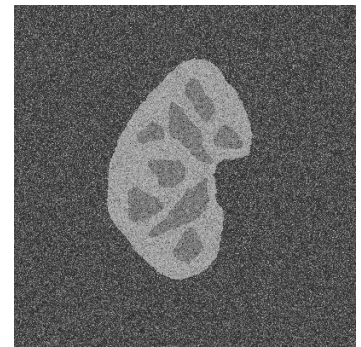
(f) $R = 10, T_x = 10, T_y = 10$



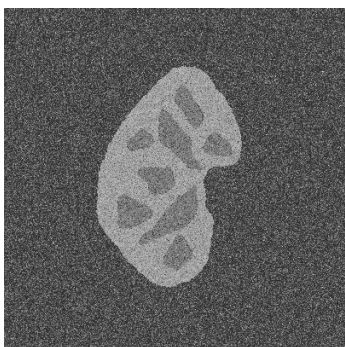
(g) $R = 5, T_x = 0, T_y = 0$



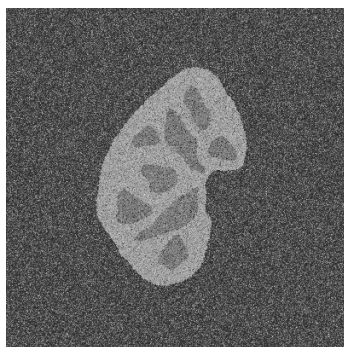
(h) $R = 5, T_x = 0, T_y = 5$



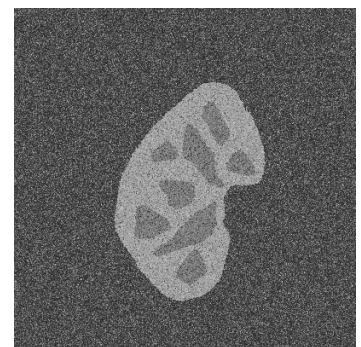
(i) $R = 5, T_x = 5, T_y = 0$



(j) $R = 5, T_x = 5, T_y = 5$



(k) $R = 10, T_x = 5, T_y = 5$



(l) $R = 10, T_x = 20, T_y = 20$

FIGURE 23: Test Sequence 2. Background, cortex and medulla structures in the mask are filled separately with random variables obtained via inverse mapping from the gray level CDF's (Fig. 20(h)) of Fig. 20(b)).

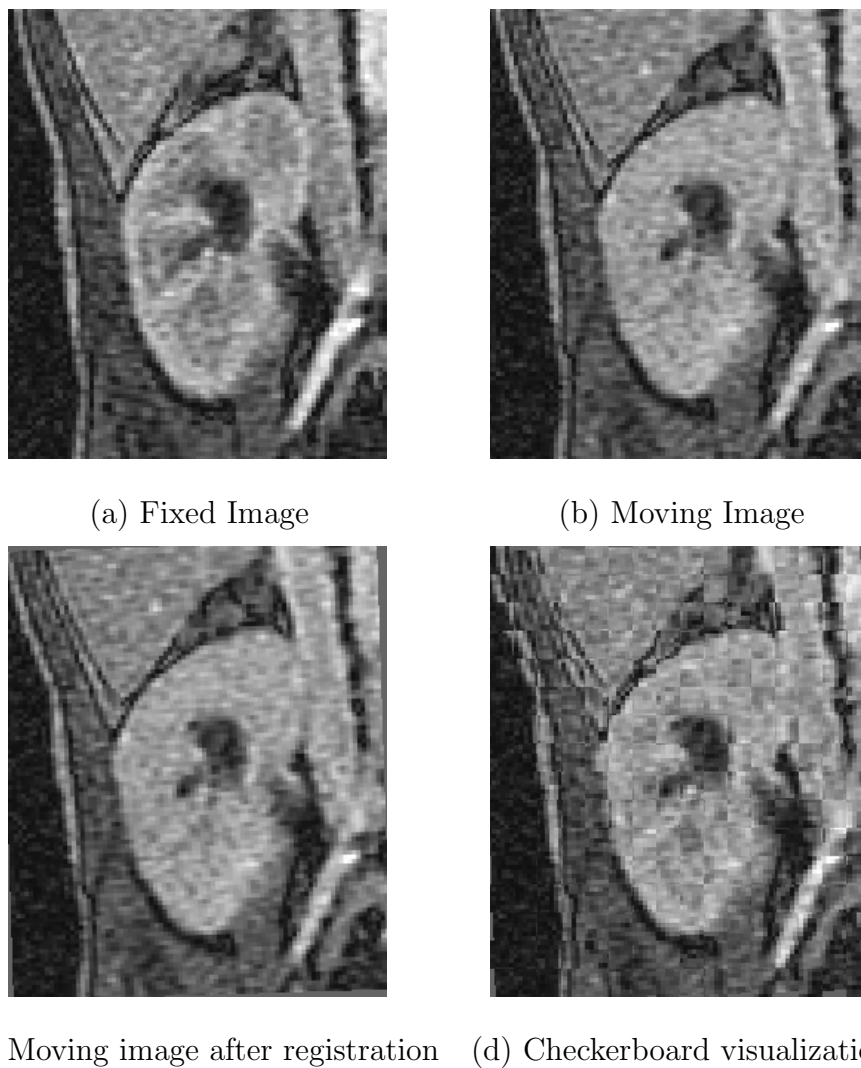


FIGURE 24: Sample registration results for two images from one data set. The moving image in (b) is registered to the fixed image in (a), and the resultant registration is shown in (c). A checkerboard image is generated from (a) and (c) to test the quality of the registration visually. A checkerboard image is basically obtained by patching one square region from the fixed image and another square region from the moving image after registration, and the expectation is to see continuous contours in between the patches, which is very well obtained in (d). Registration results: Rotation $R = 1.82$ degrees, translation in x direction $T_x = 1.48$ pixels, translation in y direction $T_y = 0.77$ pixels, MI metric = 0.27.

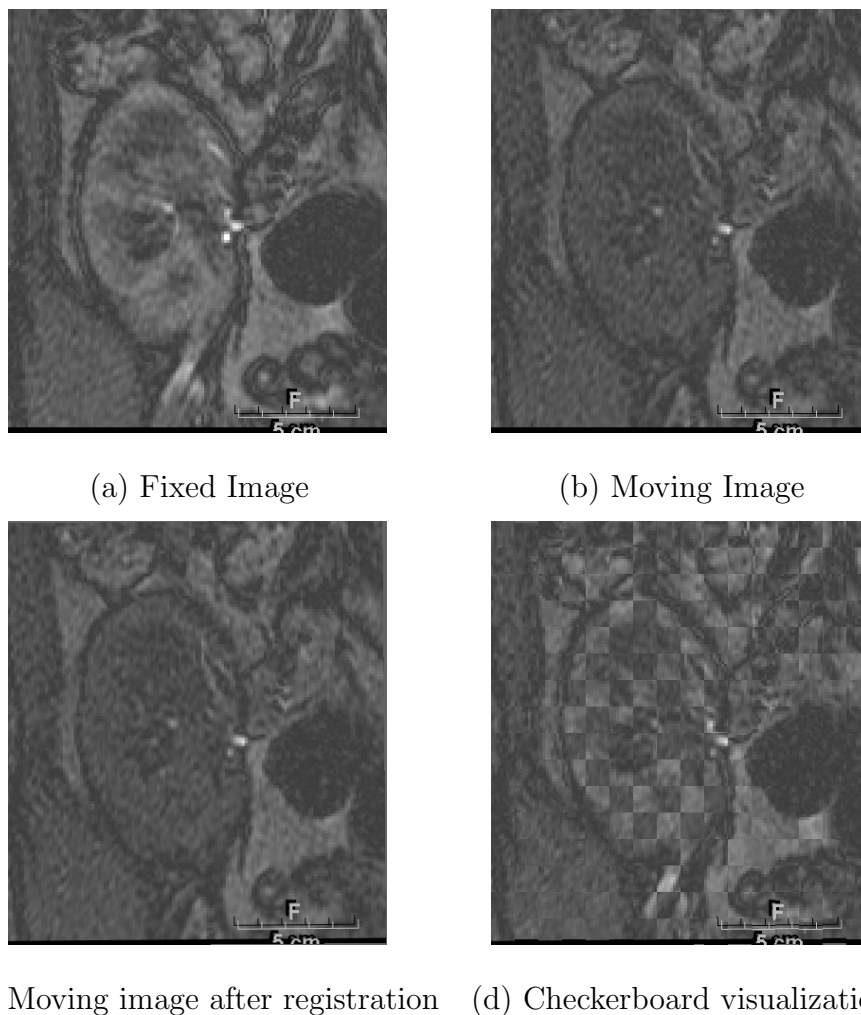


FIGURE 25: Sample registration results for two images from one data set. The moving image in (b) is registered to the fixed image in (a), and the resultant registration is shown in (c). A checkerboard image is generated from (a) and (c) to test the quality of the registration visually. A checkerboard image is basically obtained by patching one square region from the fixed image and another square region from the moving image after registration, and the expectation is to see continuous contours in between the patches, which is very well obtained in (d). Registration results: Rotation $R = 0.47$ degrees, translation in x direction $T_x = 2.33$ pixels, translation in y direction $T_y = -0.10$ pixels, MI metric = 0.18.

CHAPTER IV

SEGMENTATION

Dynamic Contrast Enhanced Magnetic Resonance Imaging (DCE-MRI) offers the ability to obtain separate anatomical information from the cortex and medulla structures of the kidney. Therefore, to allow slice-by-slice comparison of these structures individually, we need to first extract the kidney from the surrounding organs, then segment the kidney into cortex and medulla structures. An illustration of the segmentation framework is given in Fig. 26.

The main challenges in the segmentation step arise from (i) the inherent noisy nature of the DCE-MRI images, and (ii) the decreased contrast agent uptake in acute rejection patients. In the following sections of this chapter, we try to overcome these challenges. In Section A, we segment the kidney from the surrounding organs in an abdomen image, and in Section B, we separate the cortex and medulla structures.

A. Segmentation of the Kidney from the Surrounding Organs

The aim in segmenting the kidney from the surrounding organs is to obtain a connected and closed kidney mask possibly avoiding the pelvis region; as illustrated in Fig. 27. For such a segmentation, the use of the gray level information is obviously useful; but depending only on gradient or gray level information generally fails. Therefore, in Section A.1 of this chapter, we try to incorporate temporal information via image subtraction: an approach that was extensively used by Giele *et al.* [9] and Sun *et al.* [47]. However, in acute rejection patients, the uptake of the contrast agent is decreased resulting in low-contrast images; so the image subtraction algorithms may fail; or even worse, ignore the regions that do not show contrast enhancement because of the advanced degree of the disease. As a solution to this problem, we developed a new segmentation approach that incorporates both the gray level information and the prior shape information. In Section A.2, we give an introduction to the traditional

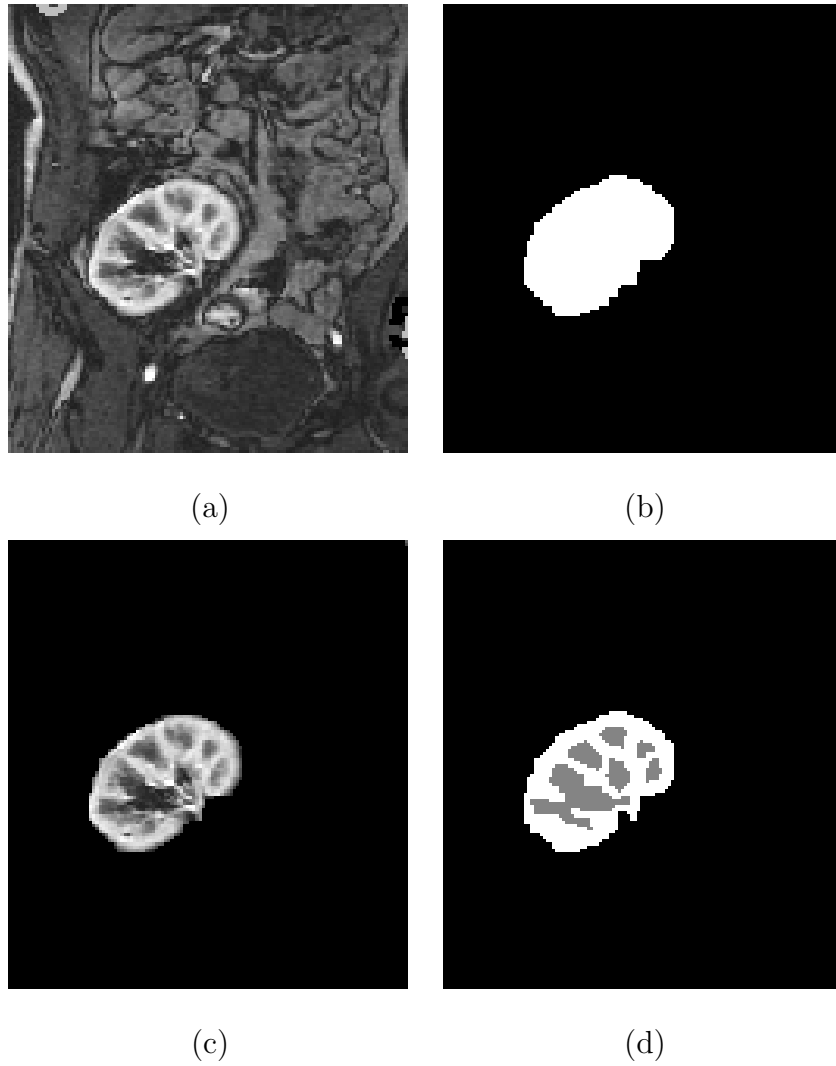


FIGURE 26 – The kidney to be segmented from the surrounding organs (a). The first stage of our segmentation algorithm is to obtain a kidney mask (b). Using this mask, kidney is isolated from the outer structures in (c). In the second stage of the segmentation approach, the kidney is segmented into its cortex (white region) and medulla (gray region) compartments (d).

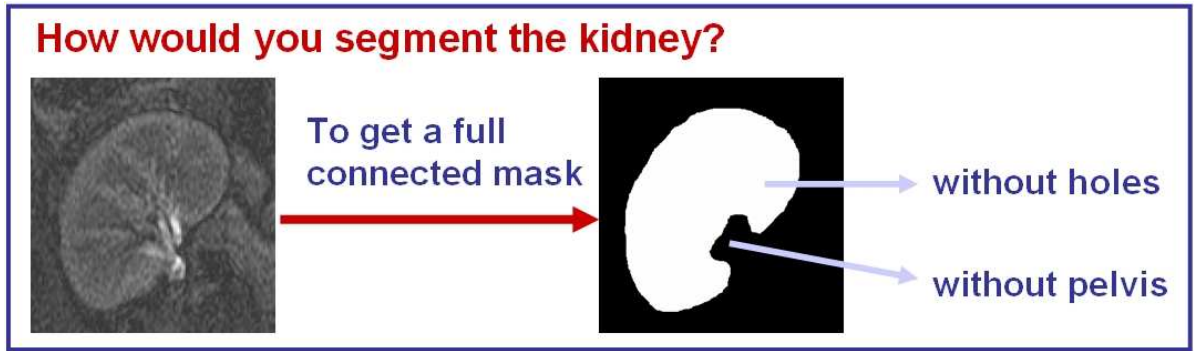


FIGURE 27 – The motivation for segmenting the kidney from the surrounding organs.

deformable models and discuss their advantages & disadvantages; and based on the knowledge of these traditional models, in Section A.3 we introduce a new shape based segmentation approach. Finally, in the results section, we show the accuracy of our segmentation results compared to manual segmentation.

1. Image Subtraction and Connected Component Analysis

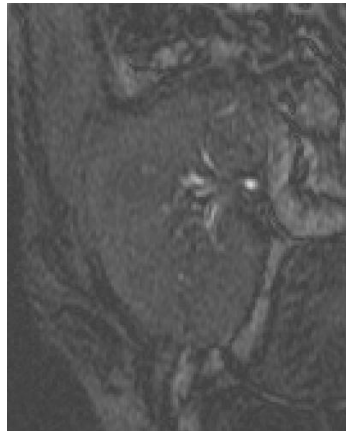
One way of using the temporal information to segment the kidneys is to use image subtraction. In image subtraction, an average of late enhancement images are subtracted from the average of non-enhanced images. In our protocol, the imaging starts as soon as the contrast agent is injected, so before the contrast agent arrives at the kidney, there are around four non-enhanced images for the normal patients, and more than 30 late-enhancement images. By averaging these images, a better signal to noise ratio is obtained; and by subtracting, the tissue that is not enhancing over time is deleted. In Fig. 28, two non-enhanced images (a, b) and two late-enhancement images (c, d) are shown. The average of (a) and (b) is subtracted from the average of (c) and (d). The subtraction image generally falls outside the intensity range; therefore, a scaling is performed on the subtraction image (I_{subt}) to put it back into the range $[0, 255]$:

$$I_{scaled} = 255 \times \frac{I_{subt} - \min(I_{subt})}{\max(I_{subt}) - \min(I_{subt})}$$

After this operation, the resulting image (I_{scaled}) may still contain some background tissue as in Fig. 28(e). To delete this tissue, the biggest connected component in the image is obtained via connected component analysis as shown in Fig. 28(f).



(a)



(b)



(c)



(d)



(e)



(f)

FIGURE 28—Image subtraction. The average of non-enhanced images (a) and (b) are subtracted from the average of enhanced images (c) and (d). The subtraction image is scaled to $[0, 255]$ intensity levels as shown in (e), and the largest connected component is extracted (f).

Although image subtraction is a fast and easy method, it might face some problems:

(i) If the subtraction is applied to the whole abdomen image, sometimes the background tissues that remains after subtraction becomes the largest connected component. A solution to this problem is to crop the images before the connected component analysis.

(ii) The arteries feeding the kidney also change color when the contrast agent perfuse into the kidney. These structures might also be kept in the subtraction image.

(iii) Some tissue might be lost in the subtraction stage which belongs to the kidney but shows little or no enhancement due to noise or due to the disease. Recovering this tissue back is a problem since it significantly affects the diagnosis if the tissue is lost due to disease.

In our software, we allow the user to test the outcome of image subtraction. If the expert is satisfied with the results, then the kidney mask can be used for further analysis. If not, we propose several algorithms in the coming sections.

2. Deformable Models

A traditional deformable model $v(s) = (x(s), y(s))$ $0 \leq s \leq 1$ is a curve as shown in Fig. 29 that deforms over a series of iterations to get aligned with a selected image feature. This image feature is generally the derivative of the image, i.e. the edge information; so that, the curve moves and gets stuck in the regions with larger derivatives where the edges are most defined, as illustrated in Fig. 30. Such a deformation is governed by an energy minimization process where the energy function depends on two terms: the internal energy and the external energy. Internal energy is computed from the contour itself, and it acts to discourage the stretching and the bending of the curve. External energy component on the other hand, is calculated from the image data (such as the edges) at the position where the contour is standing, and it pulls the contour toward the desired features. Therefore, a deformable model moves through the image domain to minimize the total energy:

$$E = E_{\text{int}} + E_{\text{ext}} = \int_0^1 E_{\text{int}}(v(s)) + E_{\text{ext}}(v(s)) ds \quad (13)$$

where $E_{\text{int}}(v(s))$ and $E_{\text{ext}}(v(s))$ denote the internal and external energy components. Tradi-

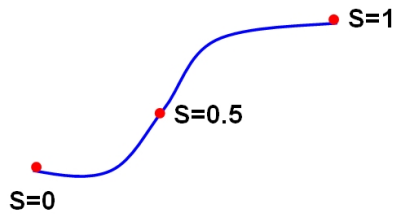


FIGURE 29–A curve can be represented parametrically as $v(s) = (x(s), y(s))$, $0 \leq s \leq 1$

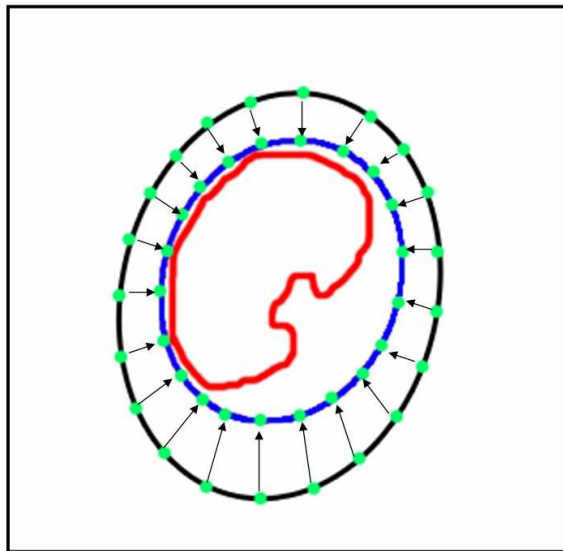


FIGURE 30–The movement of the deformable contour towards the edges. The black contour shows the initial snake at time t . At time $t + 1$, black contour deforms towards the edges (the red kidney outlier) and forms the blue contour. Green dots are the nodes that make up the contours.

tionally, these energies are introduced as:

$$\begin{aligned}
E_{int}(v(s)) &= E_{elastic}(v(s)) + E_{bending}(v(s)) \\
&= \alpha|v'(s)|^2 + \beta|v''(s)|^2 \\
E_{ext}(v(s)) &= -|\nabla\mathbf{Y}(v(s))|^2 \quad \text{or} \\
&= -|\nabla[G(v(s)) * \mathbf{Y}(v(s))]|^2
\end{aligned} \tag{14}$$

where α and β are some weights to control the curve's continuity and curvature, $v'(s)$ and $v''(s)$ are the first and second derivatives of the contour $v(s)$ with respect to s ; \mathbf{Y} is a grayscale image, $G(\dots)$ is a 2D Gaussian kernel and ∇ is the gradient operator. (More information on approximating the derivatives is given in Appendix II).

Minimization of the total energy (Eq. (13)) through the use of variational calculus, leads to solving the corresponding Euler-Lagrange equation:

$$\alpha.v'' - \beta.v'''' = -\nabla E_{ext} \tag{15}$$

To find a solution to Eq. (15), the deformable contour is treated as a function of time and the system is solved iteratively. Kass *et al.* [68] used a matrix inversion to solve this equation; while Williams *et al.* [69] slightly modified the energy terms and introduced a greedy algorithm that allows the snake to move only within a small neighborhood; this neighborhood structure is illustrated in Fig. 31. In the greedy algorithm, an energy value is calculated for all the neighbors (say in the 3x3 window) of a contour point v_i ; then the contour point v_i is moved to the neighboring point with the minimum energy. By moving all the contour points to the neighboring points with minimum energy, the energy equation (Eq. (13)) is minimized iteratively.

But both these and other parametric active contour approaches introduced later on (such as gradient vector flow) have major limitations: (1) they can only handle geometrically simple objects, (2) manual selection of an initial contour is required, (3) the algorithms depend highly on the α and β parameters, and (4) speed-wise they are mostly outperformed by the other segmentation techniques. (For more information, see Appendix III for the Kass solution; Appendix IV for Williams approach, and [68–71].)

Following these studies, geometric deformable models (level sets) were introduced, and have been widely used for their superior ability to split and merge; the results of some these

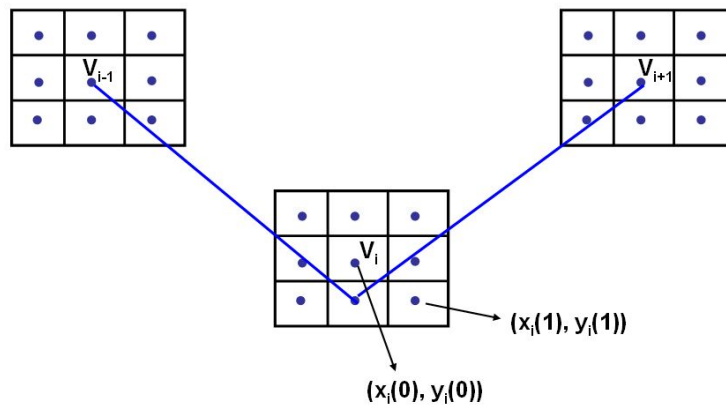


FIGURE 31 – In the greedy algorithm, each point v_i of the contour is moved within a small neighborhood (e.g. 3×3) to the point which minimizes the energy functional.

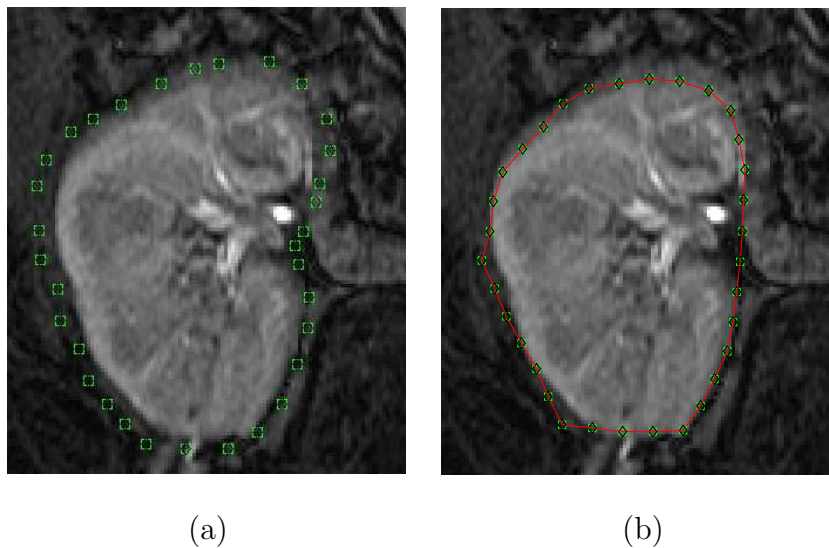


FIGURE 32 – Williams and Shah algorithm. (a) The contour is initialized manually in the close vicinity of the edges. This initial contour deforms to give the segmentation in (b). Note that the algorithm still has problems in penetrating into the concavities.

level sets algorithms (namely the thresholding level sets [67], fast marching level sets [72] and geodesic active contours [73]) are shown in Fig. 33. However; both active contours and level sets tend to fail in the case of noise, poor image resolution, diffused boundaries or occluded shapes, and they do not take advantage of the *a priori* models. Yet, especially in the area of medical imaging, organs have well constrained forms within a family of shapes [74]. Thus, additional constraints based on the shape of the objects has been greatly needed besides the gray level information of these objects.

Therefore, to allow shape driven segmentation, Leventon *et al.* [75] used a shape prior whose variance is obtained thorough PCA, and used this shape prior to evolve the level sets to the maximum *a posteriori* shape. Chen *et al.* [76] calculated an average of a registered training set to be a shape prior, and defined an energy functional which basically minimizes an Euclidean distance between a given point and its shape prior. In [77], a representation of the segmenting curve was generated based on the pose and shape parameters of a training set, which were optimized using a region based energy functional. In [74, 78] a shape prior and its variance obtained from training data are used to define a Gaussian distribution, which is then used in the external energy component of a level sets framework. In Litvin *et al.*'s study [79], a shape boundary prior was formed from the features of the boundary, and this boundary was used in a level set framework. Recently, Tsai *et al.* [80] used a deterministic model to represent the desired shape as a linear combination of weighted signed 2D distance maps and estimated these weights by minimizing a mutual information based cost function. And Yang *et al.* [81] described the shapes with a multidimensional Gaussian probability model of these weights.

Different from the previous studies, our approach is still parametric; therefore the deformable model does not split as in the geometric deformable models (level sets); which is exactly what we want: a closed connected kidney mask. Inspired by the Greedy algorithm of William and Shah, in our approach, the contour points move by comparing the energy at the neighboring points; but with different energy terms which will be explained in the next section. With this new energy component, the contour moves with both the current gray level and the prior shape information; and thus, it does not get stuck in edge points, and handles intricate shapes. Also different from the previous studies, the prior shape information is a density estimation of the signed distance map inside and outside the object of interest; not



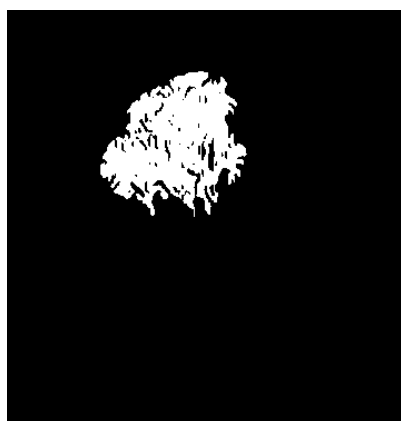
(a)



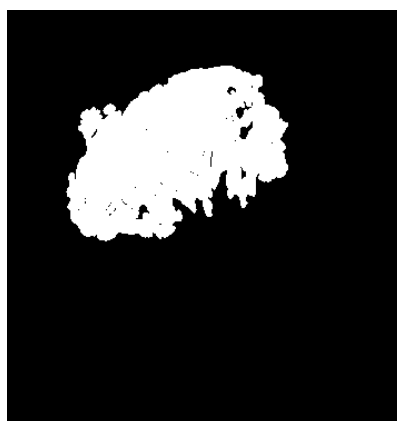
(b)



(c)



(d)



(e)

FIGURE 33–The kidney to be segmented from the surrounding organs (a). The results of some popular segmentation algorithms that depend only on gray level and gradient information: (b) connected thresholding, (c) thresholding level sets, (d) fast marching level sets, (e) geodesic active contours segmentation.

the average image itself. This algorithm overcomes the deformable models' inability to stop in high noise or in the case of missing edges.

3. Proposed Deformable Model

In this section, we introduce a new energy component which deforms the contour based on both the current gray level and the prior shape information. Both of these terms (gray level and prior shape) are represented as density functions, and both of these density functions are estimated using a modified Expectation Maximization (EM) algorithm. Therefore, the algorithm is implemented in 3 steps:

1. For a prior shape;
 - Obtain a signed distance map from a database of prior shapes.
 - Obtain an average kidney shape from the signed distance map.
 - Calculate the average of the occurrences of distances in the signed distance maps as a histogram.
 - Estimate the density of the signed distance map histogram using a modified EM algorithm.
2. For a given kidney;
 - Obtain a histogram (occurrences of gray levels) from the gray levels in the image.
 - Estimate the normalized gray level histogram density using a modified EM algorithm.
3. Combine both density estimations (for shape and for gray level) in an external energy component, and evolve the contour iteratively until whole deformable model (that is, all its current control points) do not change anymore.

The organization of these three steps will be as follows: In the next section, we describe how to estimate the gray level density of a given image using the Expectation Maximization (EM) algorithm. Further, in Section A.3.b, we explain the modified EM algorithm introduced

by Farag *et al.* ([82–84]) to enhance the results of the traditional EM algorithm. Also, a sequential EM algorithm was introduced by Farag *et al.* to give initial good parameter estimates to the modified EM; the details of which is given in Section A.3.c. In Section A.3.d, we explain how to obtain a shape model from a database and how to find its signed distance map. Once a normalized histogram of a signed distance map is found, its density is also estimated using the modified EM algorithm. With the signed distance map density of a prior shape and the gray level density of the gray levels of a current image, we introduce our proposed segmentation algorithm in Section A.3.e.

a. Mixture of Gaussians and the EM Algorithm

Expectation-Maximization (EM) algorithm is a relatively simple method to estimate the parameters of a probability function or a mixture distribution since it does not require the computation of any gradients or Hessians unlike the other optimization techniques [85, 86].

The EM algorithm produces Maximum-Likelihood (ML) estimates of the parameters through a two-step process. In the Expectation step (E-step), the expected value of the data is computed using the current estimates of the parameters, whereas in the Maximization step (M-step), new estimates of the parameters are generated. Below, we provide a detailed explanation of the EM algorithm to estimate the parameters of a mixture of Gaussians.

Let \mathbf{Y} be a gray level image of size N and let $q \in [0, Q]$ denote the gray levels in this image with $f(q)$ being the normalized frequency distribution (histogram) of these gray levels such that $\sum_{q=0}^Q f(q) = 1$. Also, let $\theta = [\mu, \sigma]$ denote the mean μ and the standard deviation σ of a Gaussian density function $\varphi(q|\theta)$ defined as

$$\varphi(q|\theta) = \frac{1}{\sqrt{2\pi\sigma^2}} \exp\left[-\frac{(q-\mu)^2}{2\sigma^2}\right] \quad (16)$$

The empirical density function $f(q)$ can be approximated by a probability density function $p_{\mathbf{w}, \Theta}(q)$ which is a linear combination of K different Gaussians $\varphi(q|\theta_k)$ following the relationship:

$$p_{\mathbf{w}, \Theta}(q) = \sum_{k=1}^K w_k \varphi(q|\theta_k) \quad (17)$$

where w_k 's are the weights of the Gaussian components with the restriction

$$\sum_{k=1}^K w_k = 1 \quad (18)$$

Under the fixed number of mixture components K ; the parameters $\mathbf{w} = \{w_k : k = 1 \dots K\}$ and $\Theta = \{\theta_k : k = 1 \dots K\}$ that maximize the log-likelihood can be found using an Expectation Maximization (EM) algorithm, where the log-likelihood of the empirical image Y with independent signals in the pixels $(i, j) \in \mathbf{N}$ can be written as follows:

$$\begin{aligned}
L(\mathbf{w}, \Theta) &= \frac{1}{|\mathbf{N}|} \log \left(\prod_{(i,j) \in \mathbf{N}} f(Y_{i,j}) \right) \\
&= \frac{1}{|\mathbf{N}|} \log \left(\prod_{q=0}^Q (p_{\mathbf{w}, \Theta}(q))^{|\mathbf{N}|f(q)} \right) \\
&= \sum_{q=0}^Q f(q) \log p_{\mathbf{w}, \Theta}(q)
\end{aligned} \tag{19}$$

where $f(q)$ is the empirical density function and $p_{\mathbf{w}, \Theta}$ is its estimate.

To find the linear combination of Gaussian components with parameters \mathbf{w} and θ that maximize this likelihood, EM algorithm offers an iterative approach through a two step procedure: Expectation and Maximization. Starting with an initial assumption of the parameters $w^{[0]}$ and $\theta^{[0]}$, in the Expectation step of the EM algorithm the relative contributions of the gray levels to each Gaussian component (also called conditional weights, prior probabilities or responsibilities) are calculated. If we define m to be the iteration number starting from 1, one can calculate these conditional weights from the equation:

$$\pi^{[m]}(k|q) = \frac{w_k^{[m-1]} \varphi(q|\theta_k^{[m-1]})}{p_{\mathbf{w}, \Theta}^{[m-1]}(q)} \tag{20}$$

with the condition

$$\sum_{k=1}^K \pi^{[m]}(k|q) = 1; \quad q = 0, \dots, Q \tag{21}$$

Therefore, in the Expectation step, one obtains information about the conditional probabilities π of each Gaussian component under fixed, current estimates of \mathbf{w} and θ , and then this information is used in the Maximization step to find the better estimates of \mathbf{w} and θ that would maximize the log-likelihood function. However, the log-likelihood in Eq. (19) is not dependent on the π values, but on the unknown \mathbf{w} and θ . Therefore, with a little trick, one can modify

the log-likelihood function of Eq. (19) by multiplying its right hand side with the left hand side of Eq. (21) (since the latter is equal to one), so the log-likelihood takes the form:

$$L(\mathbf{w}^{[m]}, \Theta^{[m]}) = \sum_{q=0}^Q f(q) \left[\sum_{k=1}^K \pi^{[m]}(k|q) \log p_{\mathbf{w}, \Theta}^{[m]}(q) \right] \quad (22)$$

In this representation, the log-likelihood is in terms of both the unknown parameters \mathbf{w} and θ that we are trying to estimate, and also in terms of the known parameter π which carries information of the previous iteration. To find the new values of \mathbf{w} and θ that maximize the log-likelihood function, one should solve Eq. (22) independently for \mathbf{w} and θ under the constraint of Eq. (21) with the Lagrange multiplier λ . If we want to solve the log-likelihood for \mathbf{w} , the maximization problem can be written as:

$$\frac{\partial}{\partial w_k} \left[\sum_{q=0}^Q \sum_{k=1}^K f(q) \pi^{[m]}(k|q) \log p_{\mathbf{w}, \Theta}^{[m]}(q) + \lambda \left(\sum_{k=1}^K w_k^{[m]} - 1 \right) \right] = 0 \quad (23)$$

Replacing the term $\log p_{\mathbf{w}, \Theta}^{[m]}(q)$ from Eq. (20) with the equal terms:

$$\log p_{\mathbf{w}, \Theta}^{[m]}(q) = \log w_k^{[m]} + \log \varphi(q|\theta_k^{[m]}) - \log \pi^{[m+1]}(k|q) \quad (24)$$

the solution of Eq. (23) for \mathbf{w} turns into the following equation:

$$\sum_{q=0}^Q f(q) \pi^{[m]}(k|q) \frac{1}{w_k^{[m]}} + \lambda = 0$$

For $\lambda = -1$, the weight parameter \mathbf{w} is found as:

$$w_k^{[m]} = \sum_{q=0}^Q f(q) \pi_k^{[m]}(k|q) \quad (25)$$

Following the same procedure as above and assuming Gaussian distributions, one can solve the log-likelihood equation (22) for μ and σ using the equations (16) and (24), and reach to the well-known equations for μ and σ :

$$\begin{aligned} \mu_k^{[m]} &= \frac{1}{w_k^{[m]}} \sum_{q=0}^Q q f(q) \pi_k^{[m]}(k|q) \\ (\sigma_k^{[m]})^2 &= \frac{1}{w_k^{[m]}} \sum_{q=0}^Q \left(q - \mu_k^{[m]} \right)^2 f(q) \pi_k^{[m]}(k|q) \end{aligned} \quad (26)$$

To put it together, after the initialization of the parameters \mathbf{w} and $\boldsymbol{\theta}$, the EM iterations start aiming to estimate the parameters $\boldsymbol{\pi}$, \mathbf{w} , $\boldsymbol{\mu}$ and $\boldsymbol{\sigma}$. In the E-step, a posterior probability $\boldsymbol{\pi}$ is assigned to each Gaussian component by Eq. (20). In the M-step, the log-likelihood is maximized and the corresponding \mathbf{w} and $\boldsymbol{\theta}$ values are computed by Eq. (25) and Eq. (26). The iterations to compute the E-step and M-step continue until the parameters \mathbf{w} and $\boldsymbol{\theta}$ don't change with the iterations. A pseudo-code summarizing these steps can be given as:

```

initialize  $\boldsymbol{\theta}^{[0]}$ ,  $\mathbf{w}^{[0]}$ ,  $error_1$ ,  $error_2$ ,  $m = 0$ 

do  $m = m+1$ 

E-step: Estimate the conditional probabilities  $\boldsymbol{\pi}^{[m]}$  from Eq.(20)
        using the previous estimates of  $\boldsymbol{\theta}^{[m-1]}$  and  $\mathbf{w}^{[m-1]}$ .

M-step: Compute Maximum Likelihood estimate of parameters
         $\boldsymbol{\theta}^{[m]}$ ,  $\mathbf{w}^{[m]}$  from Eq.(25-26) using  $\boldsymbol{\pi}^{[m]}$  of the E-step.

until  $(\boldsymbol{\theta}^{[m]} - \boldsymbol{\theta}^{[m-1]}) < error_1$  and  $(\mathbf{w}^{[m]} - \mathbf{w}^{[m-1]}) < error_2$ 

```

To conclude, given a normalized histogram of an image, we can approximate this histogram with a density function composed of a linear combination of Gaussians whose weights \mathbf{w} and density parameters $\boldsymbol{\theta}$ are found with an iterative approach: the Expectation-Maximization (EM) algorithm. EM algorithm starts with initializing the \mathbf{w} and $\boldsymbol{\theta}$ parameters. Then in the Expectation step, the conditional probabilities $\boldsymbol{\pi}$ are calculated from the known parameters \mathbf{w} and $\boldsymbol{\theta}$, and in the Maximization step, the log-likelihood of the empirical density is maximized by finding the new estimates of \mathbf{w} and $\boldsymbol{\theta}$ by the knowledge of the $\boldsymbol{\pi}$ values.

However, it is very clear that, this linear combination of positive Gaussians ignores the more complex densities that could be composed of positive and negative Gaussians as shown in Fig. 34. Moreover, the traditional EM algorithm depends largely on the initialization; without a good initialization that is in the close vicinity of the optimal parameters, there is no guarantee that the convergence will be to a global maximum [85]. To overcome these two problems, Farag *et al.* [82–84] introduced a modified EM algorithm that can approximate the density function with a linear combination of positive and negative Gaussians, and they also

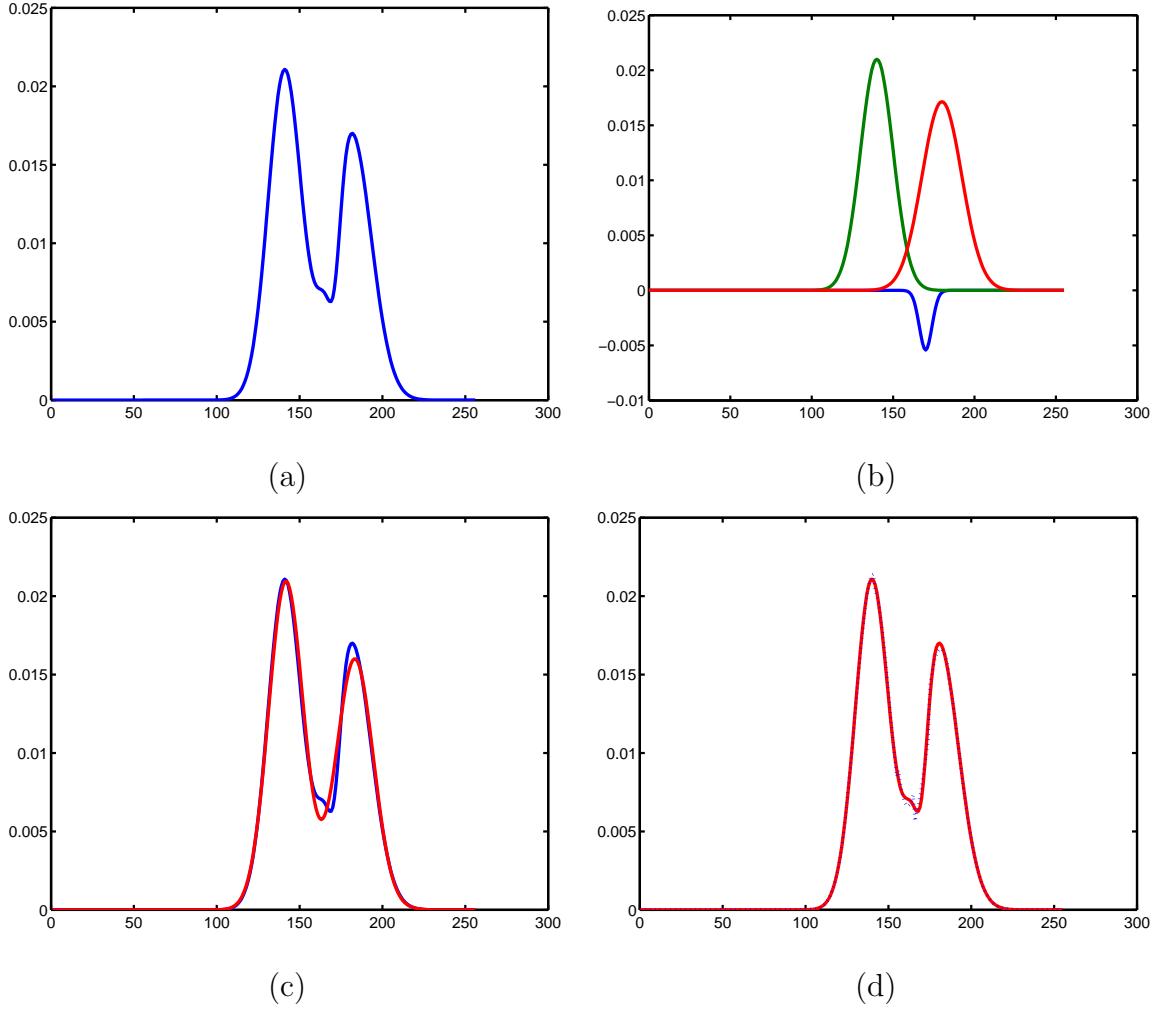


FIGURE 34 – (a) A test density $f(q)$ composed of the three Gaussian components given in (b). (c) The approximation $p(q)$ (shown in red) to $f(q)$ (shown in blue) using the traditional EM algorithm. The traditional EM algorithm could not capture the density due to the negative Gaussian component. (d) The modified EM algorithm (shown in blue) introduced by Farag *et al.* offers a better approximation to the empirical density (shown in red) as it can capture the negative Gaussian component.

introduced a sequential EM-based initialization algorithm to start the modified EM algorithm with good initial parameters. The following sections summarize these two algorithms.

b. Mixture of Gaussians with Positive and Negative Components

As an extension to the previous section to obtain better accuracy, the density function can be approximated with a linear combination of both C_p positive and C_n negative Gaussians given as:

$$p_{\mathbf{w}, \boldsymbol{\theta}}(q) = \sum_{r=1}^{C_p} w_{p,r} \varphi(q|\theta_{p,r}) - \sum_{l=1}^{C_n} w_{n,l} \varphi(q|\theta_{n,l}) \quad (27)$$

with the restriction

$$\sum_{r=1}^{C_p} w_{p,r} - \sum_{l=1}^{C_n} w_{n,l} = 1 \quad (28)$$

Under the fixed number of positive and negative components, C , the model parameters $\mathbf{w} = \{w_c; c = 1, \dots, C\}$ and $\Theta = \{\theta_c : c = 1, \dots, C\}$ maximizing the image likelihood can be found using a modified EM algorithm introduced by Farag *et al.* [82–84]. In this algorithm, the log-likelihood of the empirical data is just the same as before (see Eq. (19)), but the conditional weights are modified as:

$$\pi_p^{[m]}(r|q) = \frac{w_{p,r}^{[m-1]} \varphi(q|\theta_{p,r}^{[m-1]})}{p_{\mathbf{w},\Theta}^{[m-1]}(q)}; \quad \pi_n^{[m]}(l|q) = \frac{w_{n,l}^{[m-1]} \varphi(q|\theta_{n,l}^{[m-1]})}{p_{\mathbf{w},\Theta}^{[m-1]}(q)} \quad (29)$$

such that the following conditions holds:

$$\sum_{r=1}^{C_p} \pi_p^{[m]}(r|q) - \sum_{l=1}^{C_n} \pi_n^{[m]}(l|q) = 1; \quad q = 0, \dots, Q \quad (30)$$

As in the previous section, multiplying Eq. (30) with Eq. (19), the log-likelihood can be written as:

$$L(\mathbf{w}^{[m]}, \Theta^{[m]}) = \sum_{q=0}^Q f(q) \left[\sum_{r=1}^{C_p} \pi_p^{[m]}(r|q) \log p_{\mathbf{w},\Theta}^{[m]}(q) \right] - \sum_{q=0}^Q f(q) \left[\sum_{l=1}^{C_n} \pi_n^{[m]}(l|q) \log p_{\mathbf{w},\Theta}^{[m]}(q) \right] \quad (31)$$

From Eq. (29), the $\log p_{\mathbf{w},\Theta}^{[m]}(q)$ term in the first and second brackets can be replaced respectively with

$$\log p_{\mathbf{w},\Theta}^{[m]}(q) = \log w_{p,r}^{[m]} + \log \varphi(q|\theta_{p,r}^{[m]}) - \log \pi_p^{[m+1]}(r|q)$$

and

$$\log p_{\mathbf{w},\Theta}^{[m]}(q) = \log w_{n,l}^{[m]} + \log \varphi(q|\theta_{n,l}^{[m]}) - \log \pi_n^{[m+1]}(l|q)$$

The conditional Lagrange maximization of the log-likelihood of Eq. (31) under the restriction of Eq. (28) for Gaussian distribution gives:

$$\begin{aligned} w_{c,r}^{[m]} &= \sum_{q=0}^Q (q) \pi_c^{[m]}(r|q) \\ \mu_{c,r}^{[m+1]} &= \frac{1}{w_{c,r}^{[m+1]}} \sum_{q \in \mathbf{Q}} q \cdot f(q) \pi_c^{[m]}(r|q) \\ (\sigma_{c,r}^{[m+1]})^2 &= \frac{1}{w_{c,r}^{[m+1]}} \sum_{q \in \mathbf{Q}} (q - \mu_{c,i}^{[m+1]})^2 \cdot f(q) \pi_c^{[m]}(r|q) \end{aligned}$$

where ‘c’ stands for ‘p’ or ‘n’, respectively.

So the EM-steps are performed in the same way of the traditional EM algorithm, and the iterations are terminated when the log-likelihood of Eq. (31) begins to decrease. However, if the initialization is incorrect, this algorithm may diverge from the very beginning. Thus, a sequential initialization algorithm has been introduced by Farag *et al.* to start the modified EM with a good estimate of the Gaussian parameters.

c. *Sequential EM-Based Initialization*

The sequential algorithm first estimates the dominant components of a distribution, say for an abdomen image, it would try to find two dominant components: one for the kidney and one for the other tissues. Afterwards, it compares the error between the empirical distribution and the dominant mixture of Gaussians, and tries to approximate this error with the traditional EM algorithm. Below, we explain the algorithm step by step with the corresponding illustrative figures (Figs. 35-37).

1. Given an image as in Fig. 35(a), calculate its empirical density $f(q)$ as in Fig. 35(b), and estimate this density with a dominant mixture of two Gaussians $p_2(q)$ (one for kidney one for other tissues) using the traditional EM algorithm as shown in Fig. 35(c)-(d).
2. Find the error between $p_2(q)$ by $\Delta(q) = f(q) - p_2(q)$ as shown in Fig. 36(a).
3. Split the error into positive and negative parts such that $\Delta_p(q) = \max(\Delta(q), 0)$, $\Delta_n(q) = -\min(\Delta(q), 0)$.
4. Compute the scaling factor $s_f = \int_{-\infty}^{\infty} \Delta_p(q) dq + \Delta_n(q) dq$.
5. If $s_f < \text{threshold}$, terminate with $p_2(q)$ as the distribution.
6. Otherwise scale-up the deviations $\frac{1}{s_f} \Delta_p$ and $\frac{1}{s_f} \Delta_n$ to consider them as two new empirical densities as shown in Fig. 36(b).
7. Assume the number of the zero crossings as the number of the Gaussian components C_p and C_n and approximate the positive and negative components (P_p and P_n) with the traditional EM algorithm as shown in Fig. 36(c)-(d).
8. Scale down the Gaussians P_p and P_n .

9. The desired approximation $P_c = P_2 + P_p + P_n$ as shown in Fig. 37(a), and the number of classes is $C = 2 + C_p + C_n$.
10. Determine which Gaussian component belongs to which class as illustrated in Fig. 37(b) with the following steps:
 - i) Assign the gaussians with mean bigger than the dominant class 1 (μ_1) to class 1.
 - ii) Assign the Gaussians below the mean of dominant class 2 (μ_2) to class 2.
 - iii) For the mean values in the range $[\mu_1, \mu_2]$, apply thresholding where threshold value is the one that minimizes the classification error $e(t)$:

$$e(t) = \int_{-\infty}^t p(q|2)dq + \int_t^{\infty} p(q|1)dq.$$

With the sequential algorithm, an initial estimate of densities of the two classes are obtained.

d. Shape Modeling

To obtain a prior shape model for the kidney, we used a database of ten subjects as shown in Fig. 38. As a first step, we manually segmented the kidneys from these 10 subjects as shown in Fig. 39. Then we obtained the 2D shape model of a kidney with the following steps:

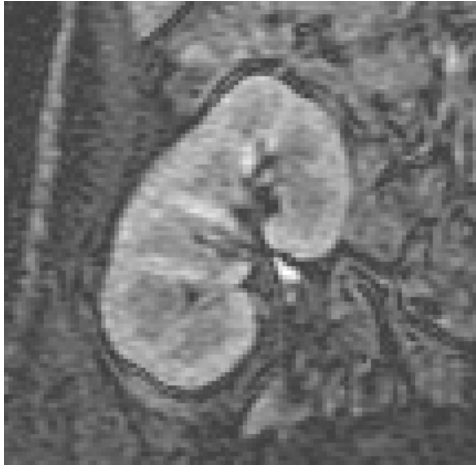
1. Align the segmented data set using affine registration. In 2D affine registration, the transformation matrix is given

$$\begin{bmatrix} x_{new} \\ y_{new} \\ 1 \end{bmatrix} = \begin{bmatrix} 1 & 0 & T_X \\ 0 & 1 & T_Y \\ 0 & 0 & 1 \end{bmatrix} \begin{bmatrix} s_c & 0 & 0 \\ 0 & s_c & 0 \\ 0 & 0 & 1 \end{bmatrix} \begin{bmatrix} \cos(\theta) & -\sin(\theta) & 0 \\ \sin(\theta) & \cos(\theta) & 0 \\ 0 & 0 & 1 \end{bmatrix} \begin{bmatrix} x \\ y \\ 1 \end{bmatrix} \quad (32)$$

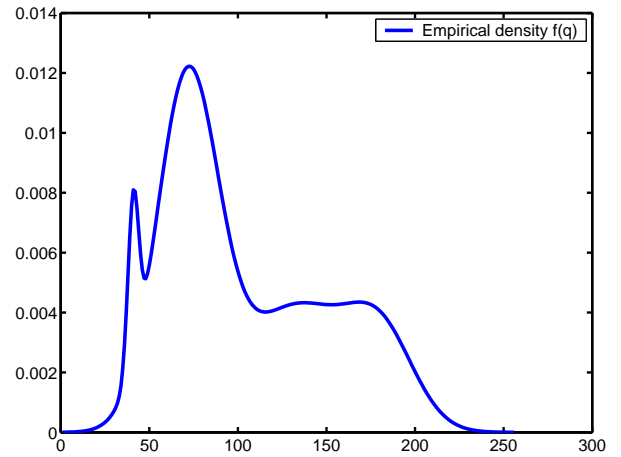
where θ is the rotation, s_c is the scaling parameter, T_X and T_Y are the translations.

$$\begin{aligned} x_{new} &= x s_c \cos(\theta) - y s_c \sin(\theta) + T_X \\ y_{new} &= x s_c \sin(\theta) + y s_c \cos(\theta) + T_Y \end{aligned} \quad (33)$$

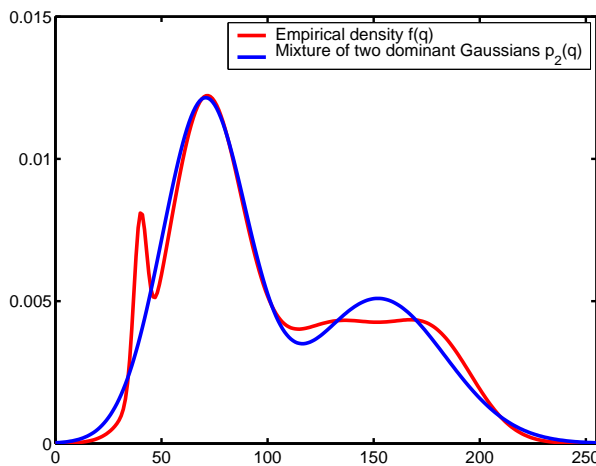
By solving these equations for θ , s_c , T_X and T_Y , affine registration handles rotations, translations and also scaling. The results of affine registration is shown in Fig. 40, and



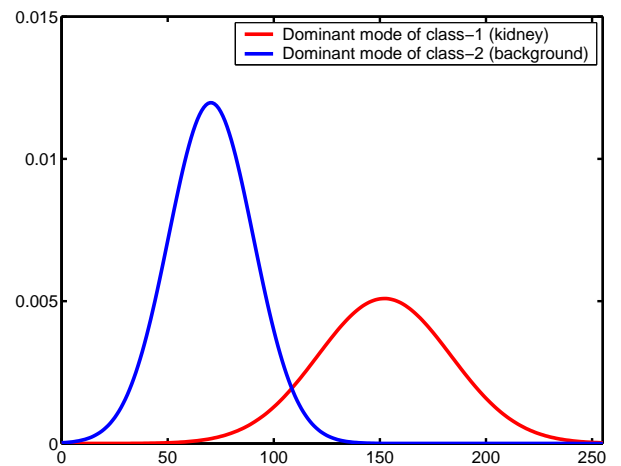
(a)



(b)



(c)



(d)

FIGURE 35—A kidney image (a) with its empirical density $f(q)$ given in (b). The empirical density $f(q)$ we want to estimate (in red), and its approximation with two dominant modes using the traditional EM algorithm (in blue) (c). The two dominant modes (d) corresponding to the density estimation of $class_1$ (the kidney) and $class_2$ (the background) found by the traditional EM algorithm .

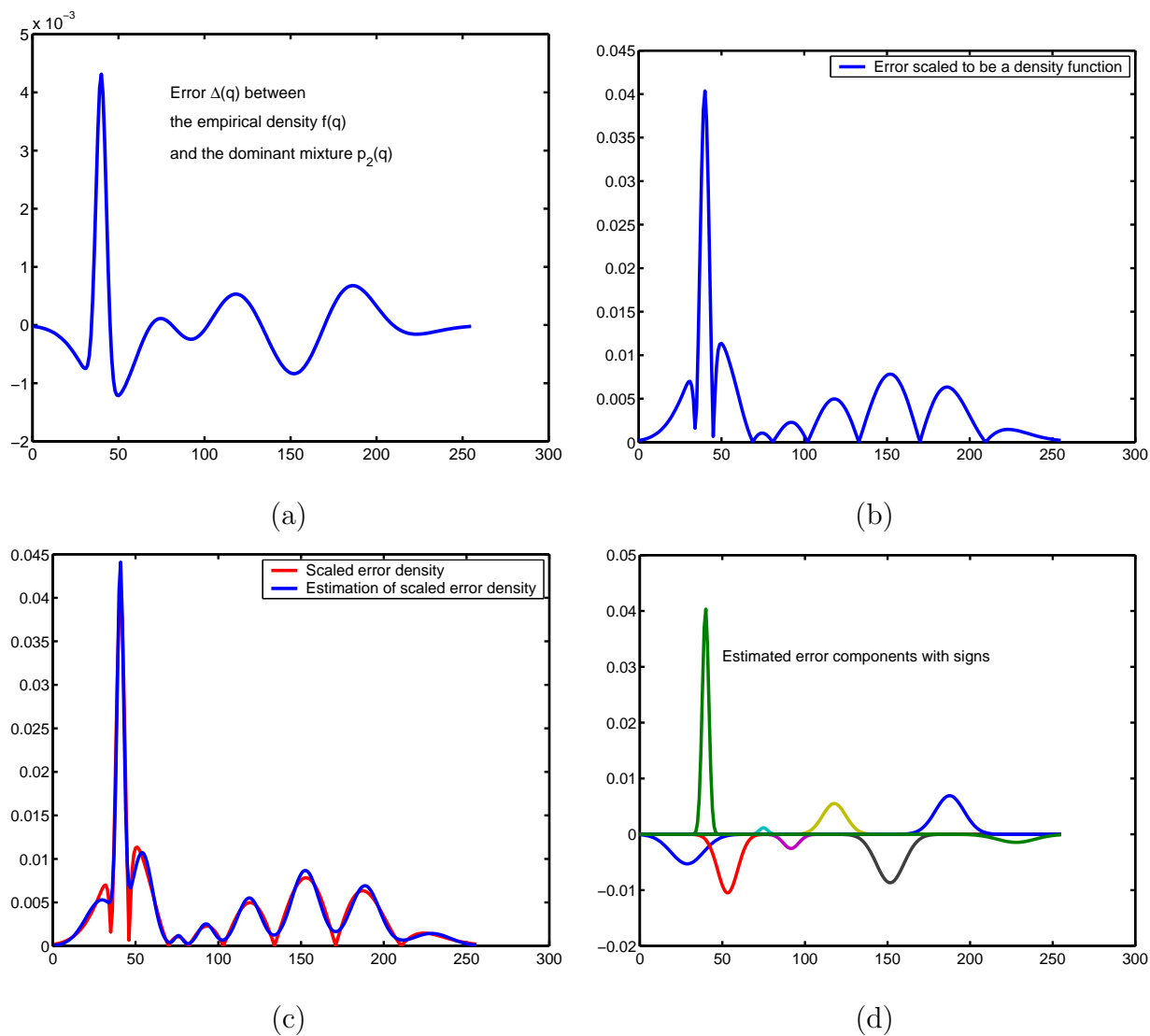


FIGURE 36—(a) The error $\Delta(q)$ between the empirical density $f(q)$ and the two dominant modes shown in Fig. 35 (c). (b) Error is scaled to represent a density function. (c) Estimation of error density and the components forming this error density with signs given in (d).

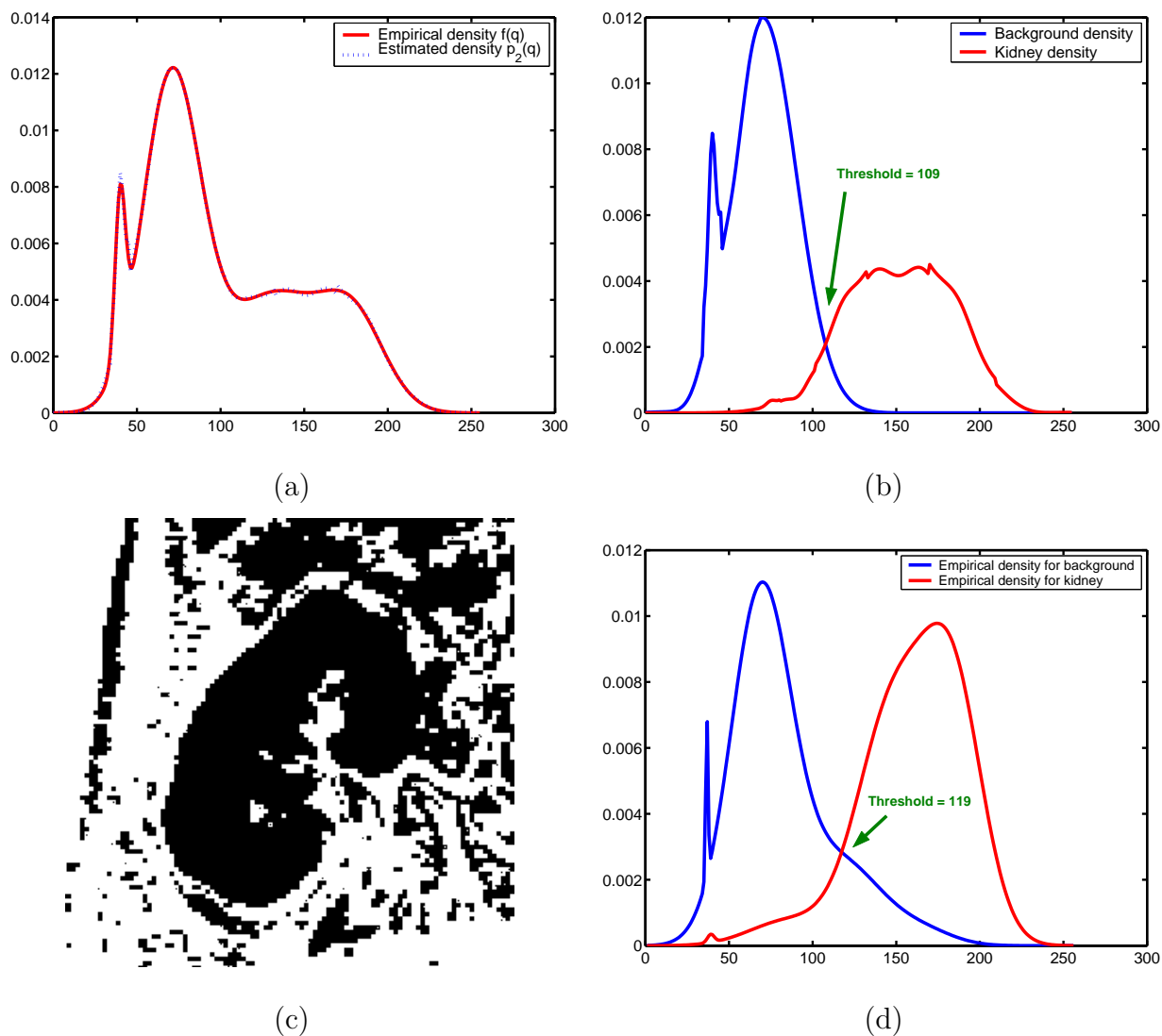


FIGURE 37—(a) The empirical density $f(q)$ shown in red and its estimation $p_2(q)$ shown in blue. (b) Step-10 of the Sequential EM algorithm assigns the error components to the two dominant classes so as to minimize the error between the empirical density $f(q)$ and its estimation $p(q)$, and finds the threshold to be 109. If only this threshold was used in segmentation, the segmentation result would be as in (c). When the kidney and background are segmented manually, the densities of these two classes are as in (d), and the threshold after manual segmentation is 119. Note the similarity between the automatically estimated density in (b) and the manually obtained density in (d).

the registration parameters are given in Table 4. In Fig. 40, the gray parts represent the interpolated pixels that fall out of the box (this is just to show the effect of registration). The final registered database is given in Fig. 41.

2. From the database given in Fig. 41, find the 2D edge V of the kidneys as shown in Fig. 42.
3. For each edge image, calculate the signed distance function $S_d(i, j)$. Signed distance function basically calculates the Euclidean distance between a point on the image and the closest point to it on the contour, and gives a positive distance value if the point on the image is inside the object, or gives a negative distance otherwise. In mathematical terms, signed distance function $S_d(i, j)$ can be represented as:

$$S_d(i, j) = \begin{cases} 0 & (i, j) \in V \\ d((i, j), V) & (i, j) \in R_V \\ -d((i, j), V) & \text{Otherwise} \end{cases} \quad (34)$$

where R_V is the region which lies inside the shape and $d((i, j), V)$ is the minimum Euclidean distance between the image location (i, j) and the curve V . This representation is invariant to translation and rotation.

4. Calculate the occurrences of distance values (i.e. generate distance map histograms) for all the database, and estimate their density with the modified EM algorithm. These densities are shown in Fig. 44.
5. Add the densities found in the previous step and obtain an average density function, as shown in Fig. 45(a).
6. Average the signed distance values calculated in Step 3. If average signed distance $S_{av}(i, j)$ of a pixel (i, j) is positive, assign the pixel to be kidney, otherwise make it a background in the average shape image. With this step, an average kidney as shown in Fig. 45(b) is obtained. It is worth noting the similarity of this average kidney to the kidney images found in anatomy books.

With these steps, shape modeling is completed, and an average signed distance density (Fig. 45(a)), as well as an average kidney shape (Fig. 45(a)) is obtained. Further, the average

TABLE 4
AFFINE REGISTRATION OF THE KIDNEY DATABASE

Img. No.	Scale	R	Center X	Center Y	T_X	T_Y	Metric
1	1.05	9.77	501.06	400.80	-21.34	50.51	311.46
2	0.98	26.92	499.78	394.34	-35.13	12.36	370.03
3	0.86	9.59	511.44	388.83	-28.19	-27.32	271.49
4	1.14	14.47	501.27	397.88	1.56	29.69	459.36
5	0.87	-13.61	503.54	402.42	-40.98	-9.53	476.67
6	0.97	15.78	502.38	398.81	-33.02	45.89	181.80
7	0.93	27.26	496.61	397.57	-18.79	38.06	343.37
9	0.97	14.48	507.35	401.51	-34.05	44.19	229.79
10	1.05	2.72	506.59	401.24	-11.20	-4.47	204.13

signed distance is estimated using the modified EM algorithm as explained in the previous chapter to get the marginal densities of the kidney and the background classes. Figure 46 shows the steps of the modified EM algorithm. At the end of shape modeling, there are the only two things that are kept and used in the deformable model formulation; the average marginal densities (Fig. 46) and the average kidney shape (Fig. 45(b)). Any new kidney image that needs to be segmented is firstly registered to this average kidney shape, then the average signed distance density is used in the deformable contour energy calculations.

e. Energy Function

In this section, we describe an energy formulation that depends on the both the current gray level and the prior shape information. A given abdomen image to be segmented is firstly aligned with affine transformation to the average kidney shown previously in Fig. 45(b). Then the signed distance map density given in Fig. 45(a) is combined with the gray level density estimation of the current image in an energy formulation as follows:

$$E_{ext}(v(i)) = \begin{cases} -p_g(q|k)p_s(d|k) & \text{if } k = k^* \\ p_g(q|k)p_s(d|k) & \text{if } k \neq k^* \end{cases}$$

In this formulation, k is the region label with $k = 1$ representing the background and $k = 2$ representing the kidney region, q is the gray level and d is the signed distance; where $p_s(d|k)$

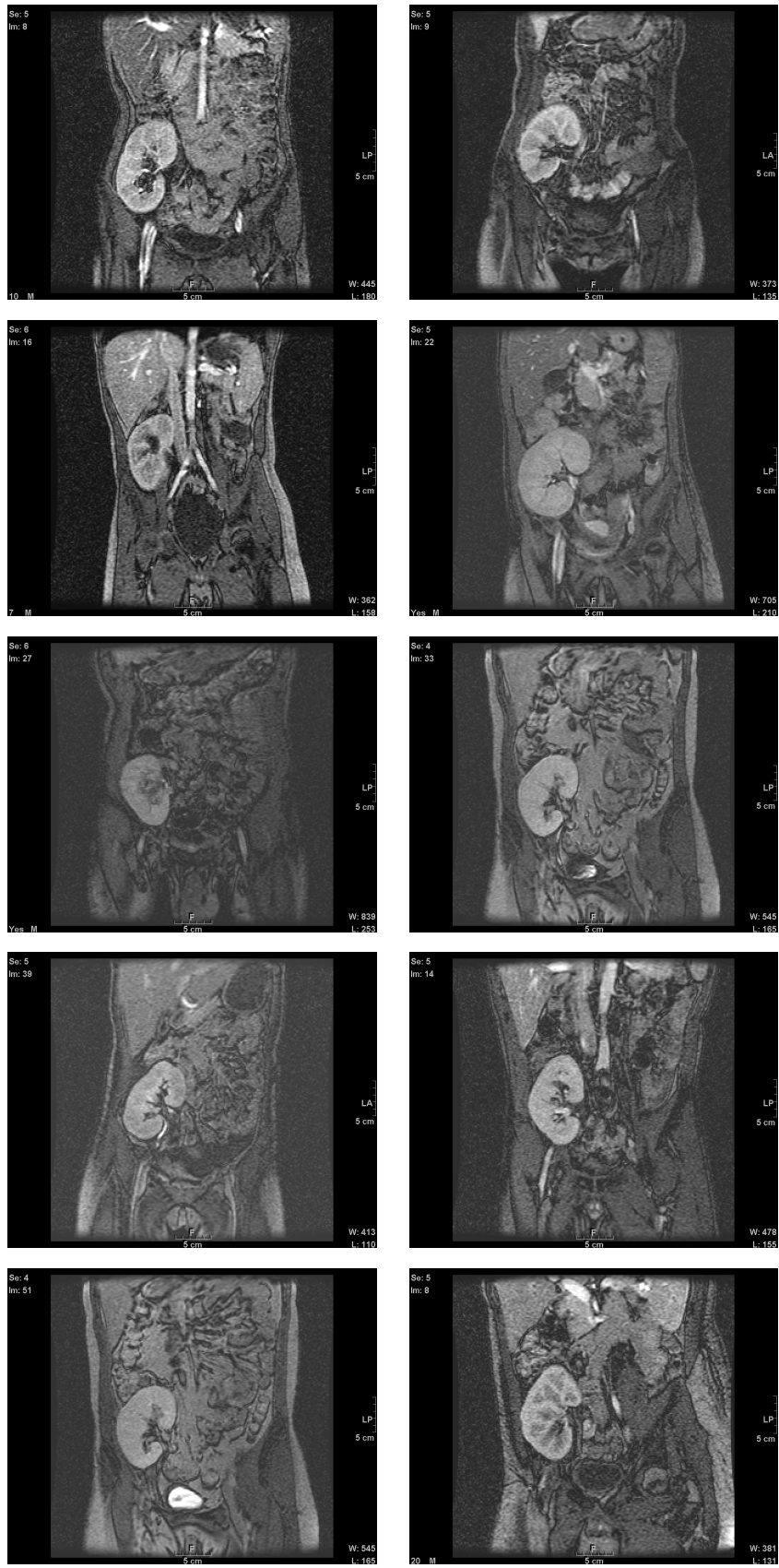


FIGURE 38–Kidney database from 10 subjects.

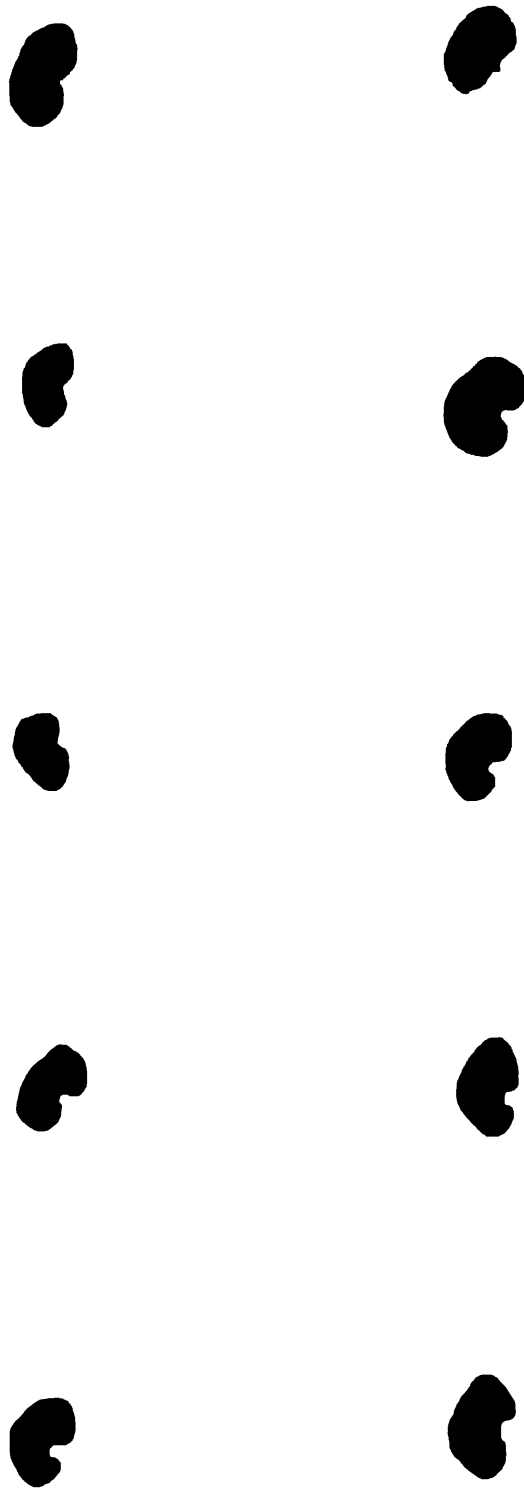


FIGURE 39—Segmented database from 10 subjects.

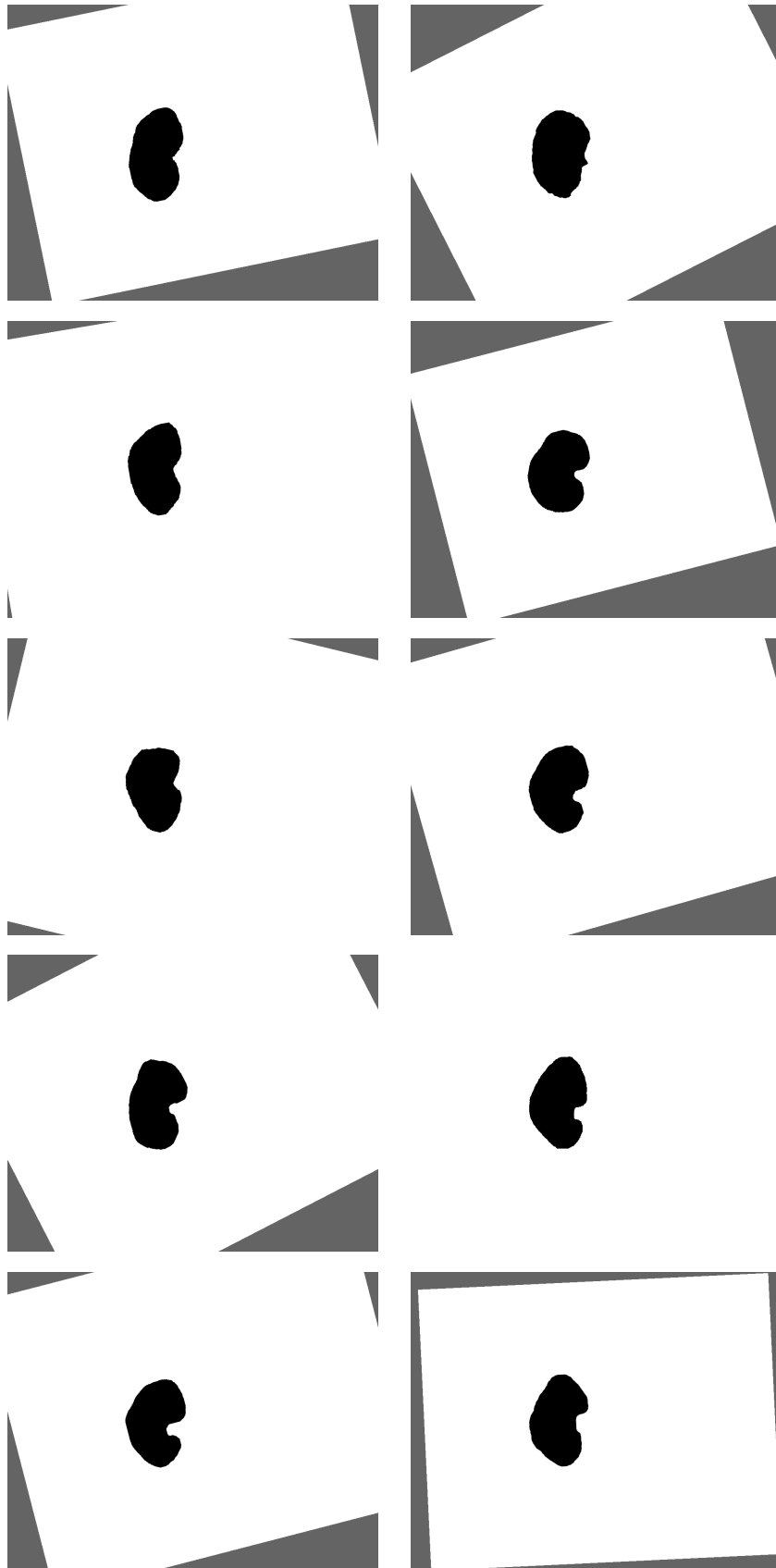


FIGURE 40 – Affine registration of the database.

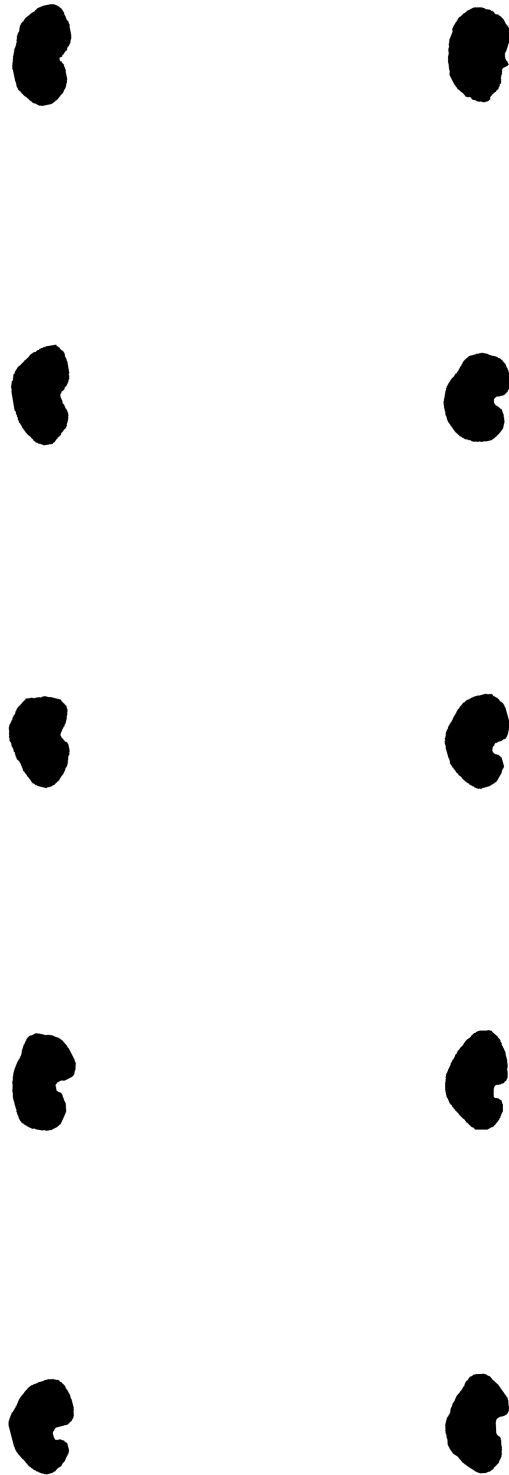


FIGURE 41 – Final registered database from 10 subjects.

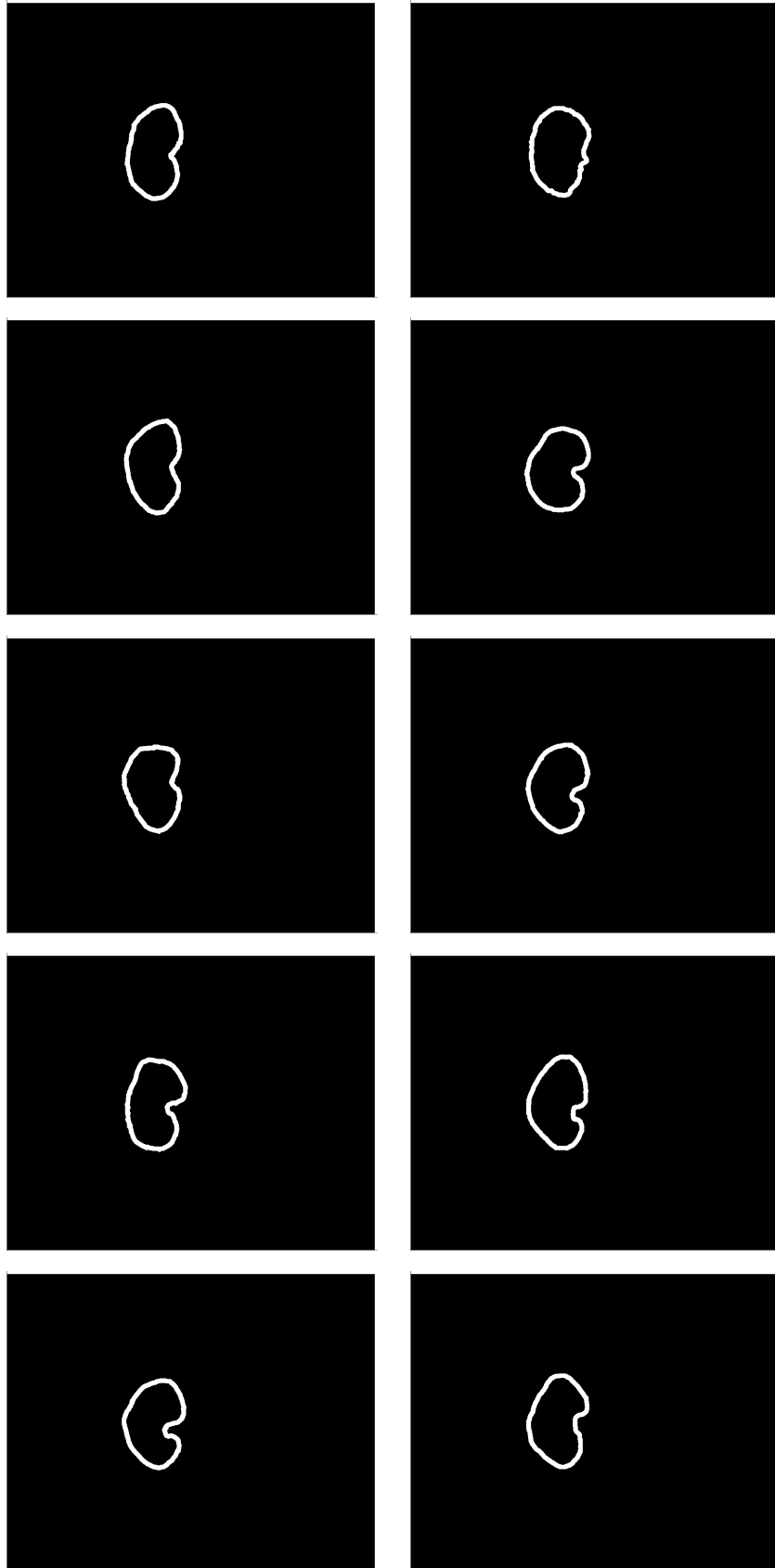


FIGURE 42–Boundaries of the aligned kidneys from 10 subjects.

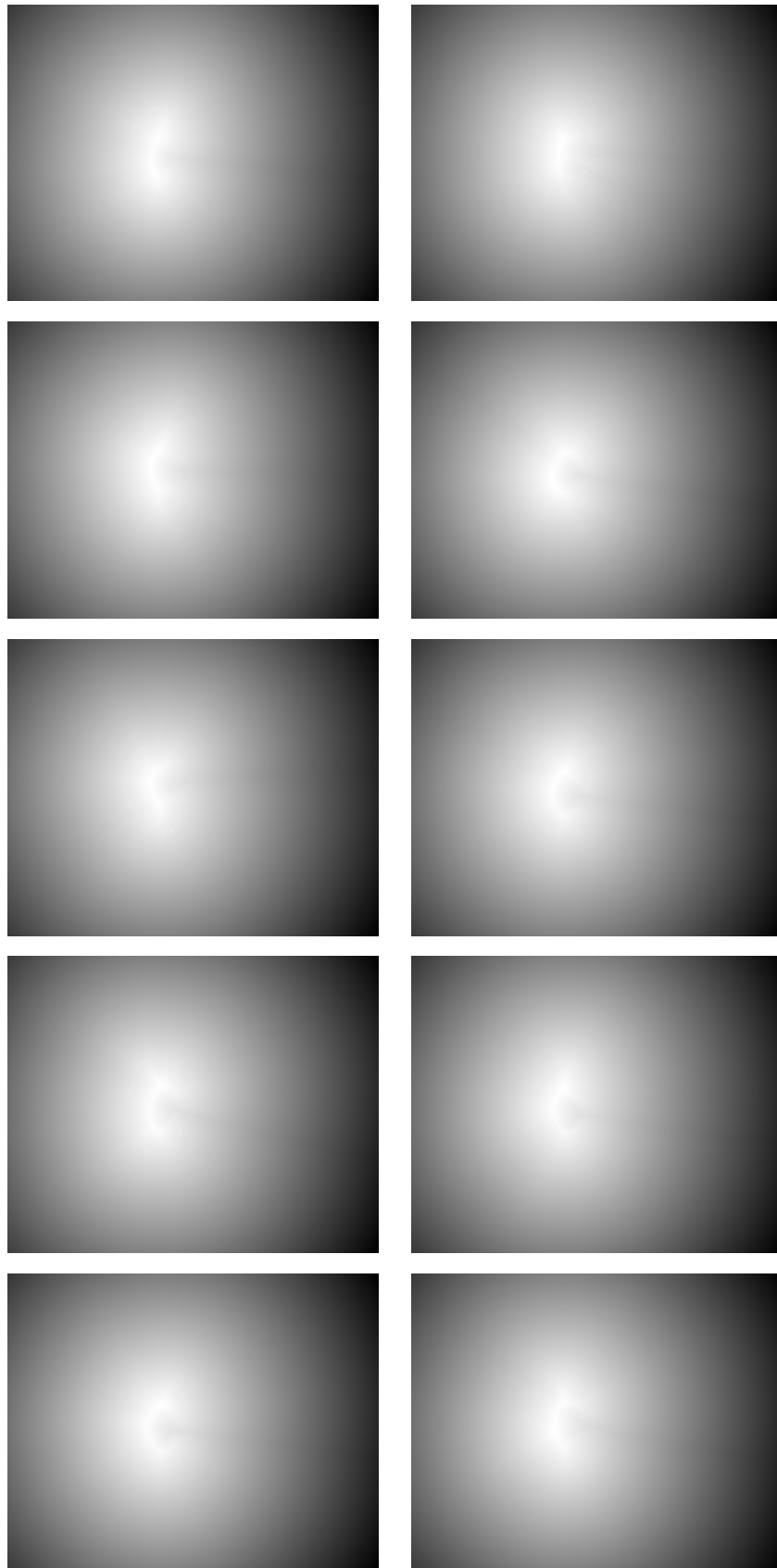


FIGURE 43–Signed distance maps of the 10 subjects.

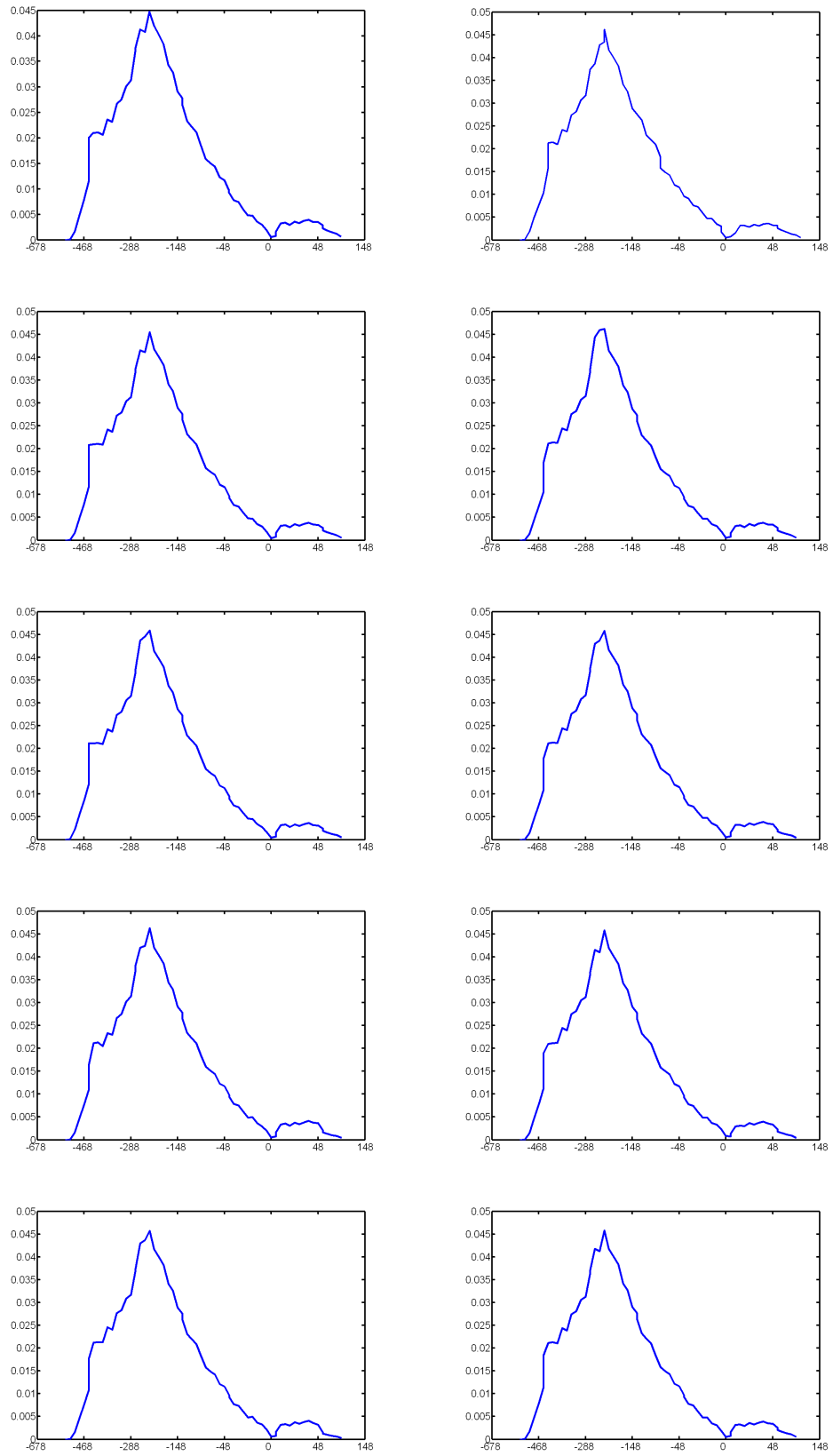
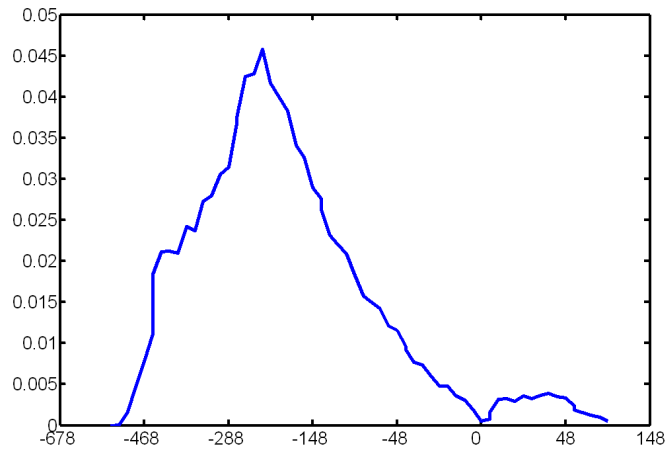
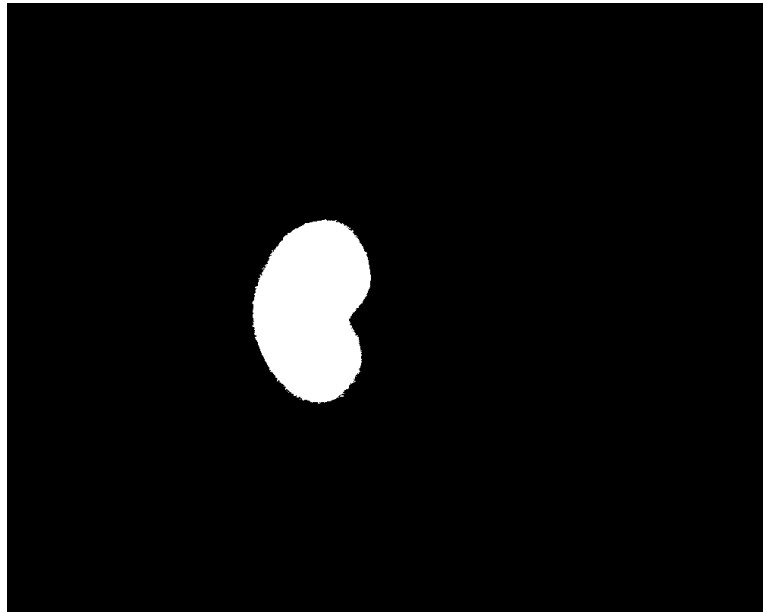


FIGURE 44– Signed distance map densities of the 10 subjects.



(a) The average signed distance map density.



(b) The average kidney shape obtained by averaging the signed distance maps.

FIGURE 45 – (a) The average density obtained by averaging the densities given in Fig. 44. (b) The average kidney shape obtained from the signed distance maps given in Fig. 43. After averaging the signed distance maps, the pixels with positive signed distance map values are assigned to be white indicating the kidney region, the pixels with negative signed distance map values are assigned to be black indicating the background.

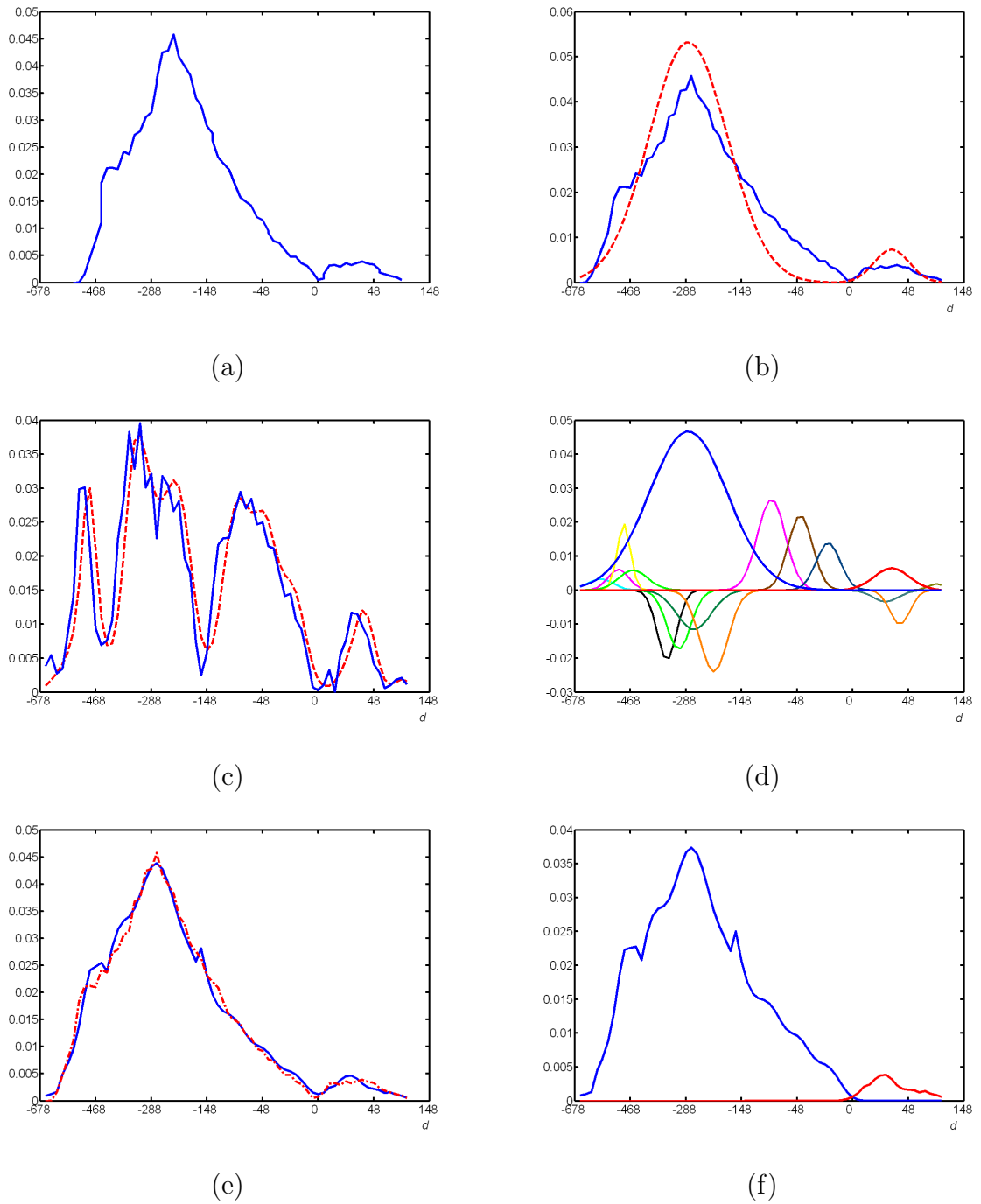


FIGURE 46—(a) The average signed distance map density. (b) The estimated two dominant modes which presents the kidney area and its background, (c) the scaled-up absolute deviation of the approximation, (d) the positive and negative LCDG components, (e) Final density estimation, and (f) the densities for two classes (red is for the kidney, blue is for the background).

is the density that describes the signed distance map inside and outside the object, and $p_g(q|k)$ is the density estimation of the gray level. With this energy function, the stochastic external force for each control point $v(i)$ of the current deformable model evolves in a region k^* in accord with the greedy algorithm. At each iteration of the greedy algorithm, the neighborhood of each control point $v(i)$ is analyzed, and the neighboring pixel ensuring the smallest total energy becomes the new position for that control point as shown in Fig. 47. The iterations continue until the whole deformable model (that is, all its current control points) do not change anymore. The proposed algorithm of segmenting the region k^* is as follows:

1. Initialize the deformable model with a seed point (or with several seed points) inside the kidney region.
2. Initialize $KidneyCounter = 0$, $BackgroundCounter = 0$.
3. For each control point $v(i)$ on the current deformable contour:
 - For each neighbor of the control point outside the current contour (red regions in Fig. 47):
 - (a) Calculate the smallest signed distance d to the boundary of the prior shape.
 - (b) Assume the point belongs to the background region $k \neq k^*$ (i.e. $k = 1$);
 - i. For the distance value d , get the corresponding density value from the signed distance density estimation $p_s(d|k = 1)$.
 - ii. For the gray level value q of this pixel, get the corresponding density value from the gray level density estimation $p_g(q|k = 1)$.
 - iii. Calculate the energy as the multiplication of the two values:
$$E_{ext1}(v(i)) = p_g(q|k = 1)p_s(d|k = 1)$$
 - (c) Assume the point belongs to the kidney region $k = k^*$ (i.e. $k = 2$);
 - i. For the distance value d , get the corresponding density value from the signed distance density estimation $p_s(d|k = 2)$.
 - ii. For the gray level value q of this pixel, get the corresponding density value from the gray level density estimation $p_g(q|k = 2)$.

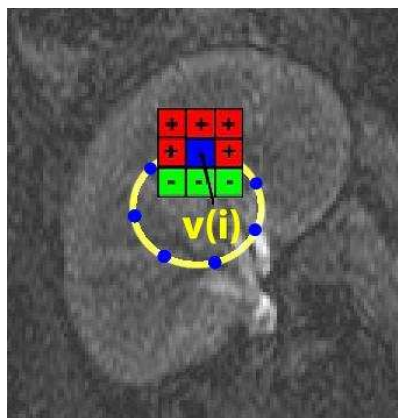


FIGURE 47–The initialization of the deformable contour. Blue dots show the contour points making up the yellow deformable contour. For each of the control points $v(i)$, greedy algorithm looks at the 3×3 neighborhood and moves to the point with lowest energy. Moving to the outer points (red pixels) makes the contour grow whereas moving inside (green pixels) makes the contour shrink.

iii. Calculate the energy as the multiplication of the two values:

$$E_{ext2}(v(i)) = p_g(q|k = 2)p_s((d|k = 2)$$

(d) If $|E_{ext1}| > |E_{ext2}|$,

$$KidneyCounter = KidneyCounter + 1;$$

else

$$BackgroundCounter = BackgroundCounter + 1;$$

- When all the neighboring points are checked, if

$KidneyCounter > BackgroundCounter$, grow the contour towards the neighbor point with minimum energy (or maximum $|E_{ext2}|$).

In Fig. 48, the movement of the proposed deformable model is illustrated. For the gray level of the current point, $p_g(q|k = 1)$ and $p_g(q|k = 2)$ are calculated from the gray level density; and for the signed distance between the current point and the boundary of the prior shape, $p_s(d|k = 1)$ and $p_s(d|k = 2)$ are calculated from the signed distance map density. Then the energy is calculated from the multiplication of these values.

To summarize, in this section we introduced a new external energy component which is composed of two terms: the gray level density estimation of the image, and the signed-distance map density of the *a priori* shape. In this formulation, we assumed that an abdomen image consists of two classes: background tissue (class 1) and kidney (class 2). For a given pixel in the

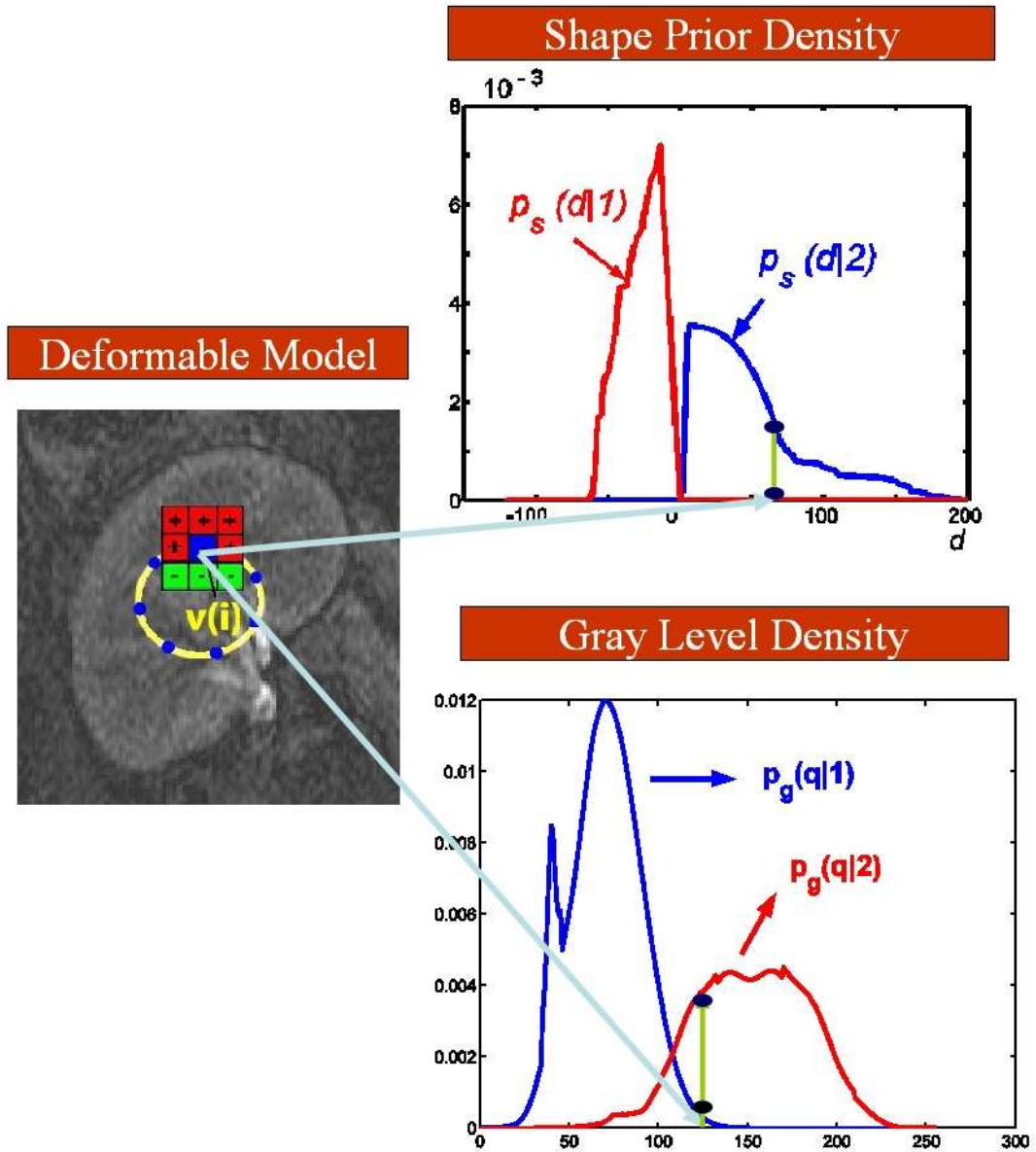


FIGURE 48 – The proposed deformable model in the kidney. For each of the neighbors of the control point $v(i)$, four values are calculated to form the external energy: two values from the signed distance density estimation ($p_s(d|k=1)$ and $p_s(d|k=2)$), and two values from the gray level density estimation ($p_g(q|k=1)$ and $p_g(q|k=2)$).

abdomen image, we calculated the energy component firstly assuming that the pixel belongs to the kidney class, secondly assuming that the pixel belongs to the other tissues. From these two values, we were able to assign the pixel to the class which gave a bigger multiplication value. Therefore; the deformable model is pulled by the energy which is a combination of both the gray level and the prior shape information. If the gray level shows big discontinuities in the kidney, it forces the deformable to stop. As such, the deformable is not allowed to go far beyond a certain shape because of the attractive force of the prior shape. With this deformable model evolution, a connected kidney mask is obtained, and the kidney is segmented from the rest of the abdomen image. In the next step, the cortex and medulla structures are segmented from this segmented kidney, with another deformable model evolution which is explained in the next section.

B. Segmentation into Cortex and Medulla

To be able to get two separate renograms for signal analysis, it is necessary to segment the kidney into cortex and medulla regions as shown in Fig. 49. For this purpose, we allow separate deformable models to grow in the regions determined by the seed points selected at the beginning of the segmentation framework, this time with the slightly modified only gray level dependent energy function:

$$E_{ext}(v(i)) = \begin{cases} -p_g(q|k) & \text{if } k = k^* \\ p_g(q|k) & \text{if } k \neq k^* \end{cases}$$

where the density is estimated with the modified EM algorithm as before, but this time considering only the gray level distribution inside the segmented kidney for an early enhancement image. Therefore, the deformable model successfully moves within a lower and upper threshold to capture the medulla regions. And since the kidney mask was obtained in the previous step, the regions staying outside the medulla is the cortex. Results of the kidney segmentation as well as the cortex and medulla segmentation are given in the following section.

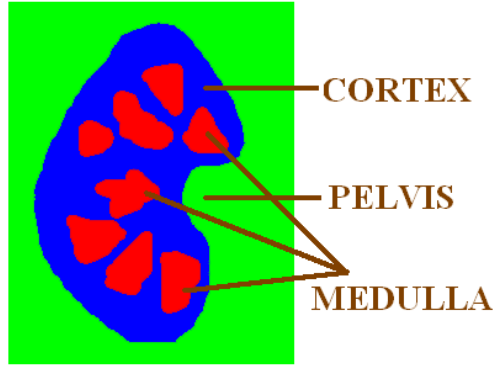


FIGURE 49 – Segmenting the kidney into cortex and medulla.

C. Segmentation Results

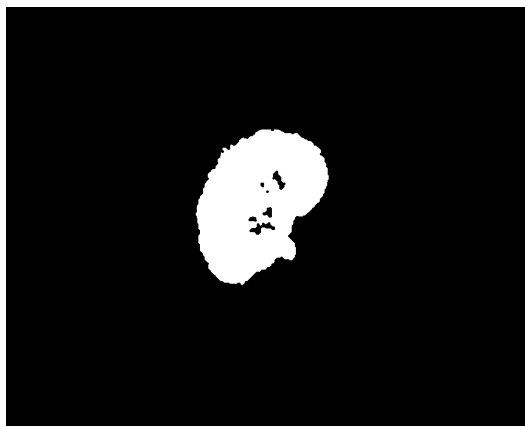
The segmentation results of seven patients are given in the following figures. First a late enhancement image is selected from the time-series of scans to segment the kidney from the background. As a general experience, the images around number 20 are good for this purpose. This image is segmented with the introduced deformable model algorithm, and its results are compared to the manual segmentation of the kidney from the background. The small black regions left inside the kidney are not due to segmentation errors, they are the arteries or other tissue connecting the kidneys, and they do not show contrast enhancement or show contrast enhancement with different patterns. At the second step, the kidney is segmented into cortex and medulla with the algorithm described in Section B. These results are indeed very satisfactory, and they are later used to plot the perfusion curves in the next chapter.



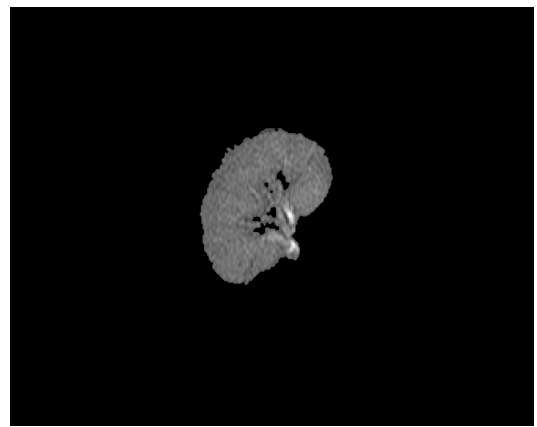
(a)



(b)



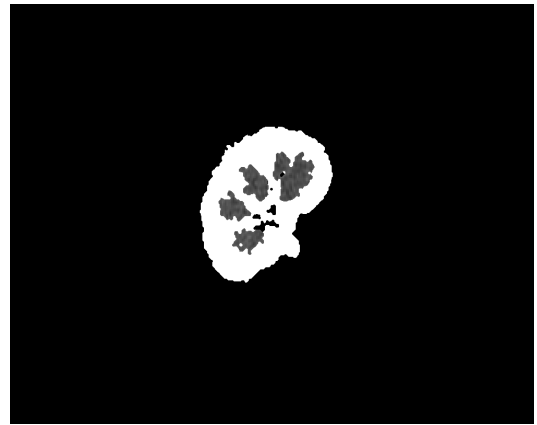
(c)



(d)



(e)

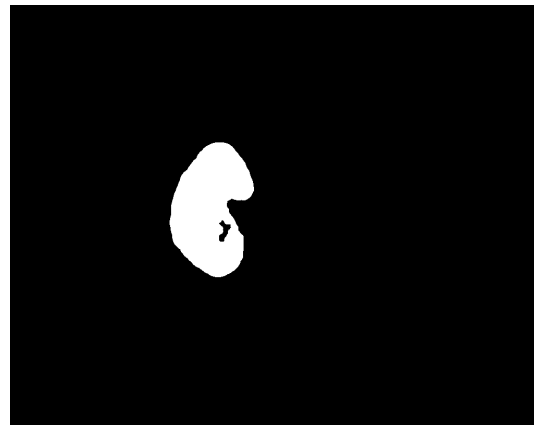


(f)

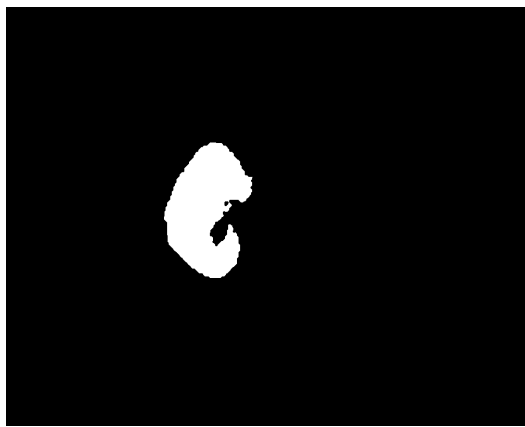
FIGURE 50–(a) A late enhancement image to segment. (b) Manual segmentation. (c) Segmentation result with error 11.51% w.r.t the area of the manually segmented kidney. (d) Segmented kidney. (e) An image from the sequence where cortex and medulla can be identified best. (f) The resultant cortex and medulla segmentation based on (e). Gray level parts are the medulla structures and the rest is the cortex.



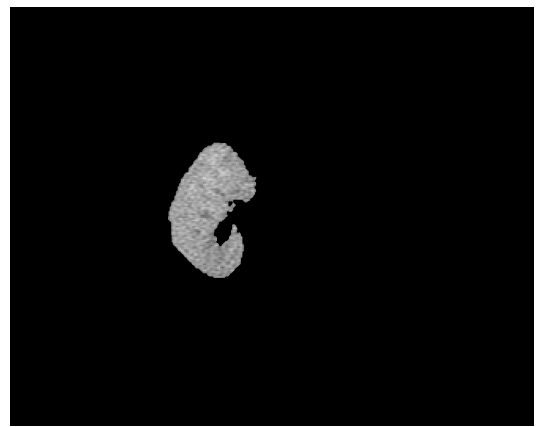
(a)



(b)



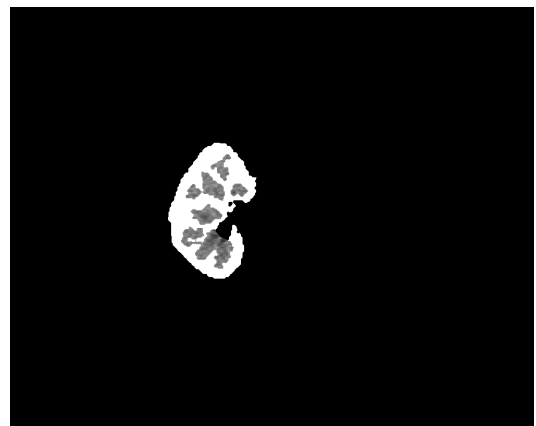
(c)



(d)

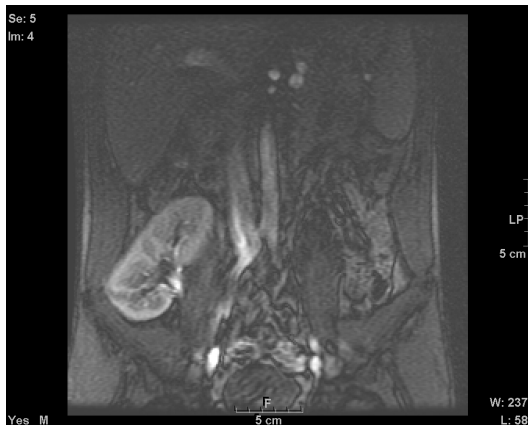


(e)



(f)

FIGURE 51 – (a) A late enhancement image to segment. (b) Manual segmentation. (c) Segmentation result with error 7.60% w.r.t the area of the manually segmented kidney. (d) Segmented kidney. (e) An image from the sequence where cortex and medulla can be identified best. (f) The resultant cortex and medulla segmentation based on (e). Gray level parts are the medulla structures and the rest is the cortex.



(a)



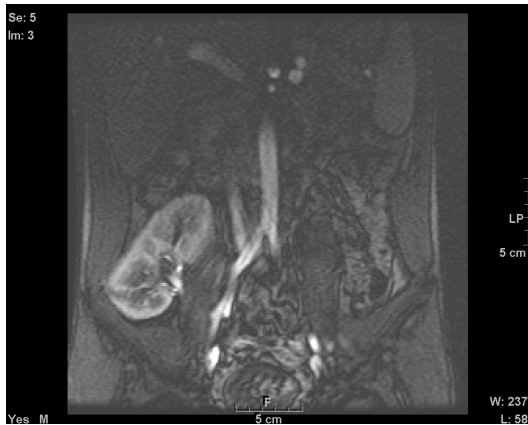
(b)



(c)



(d)



(e)

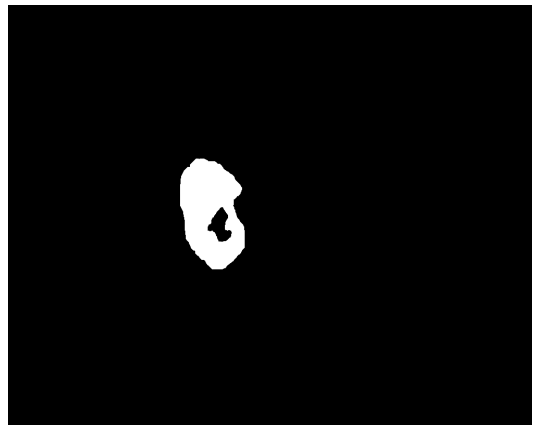


(f)

FIGURE 52–(a) A late enhancement image to segment. (b) Manual segmentation. (c) Segmentation result with error 11.36% w.r.t the area of the manually segmented kidney. (d) Segmented kidney. (e) An image from the sequence where cortex and medulla can be identified best. (f) The resultant cortex and medulla segmentation based on (e). Gray level parts are the medulla structures and the rest is the cortex.



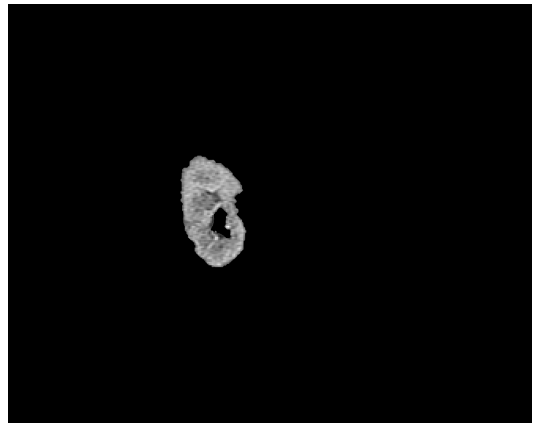
(a)



(b)



(c)



(d)



(e)

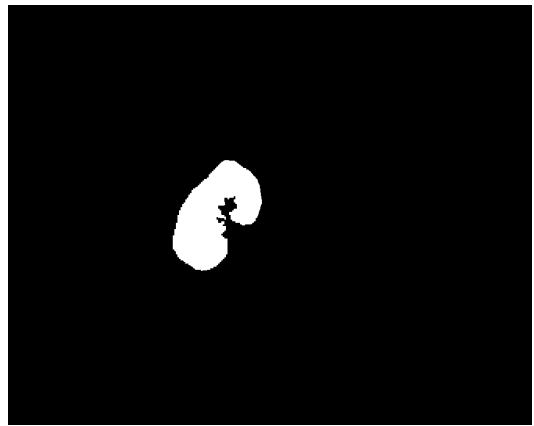


(f)

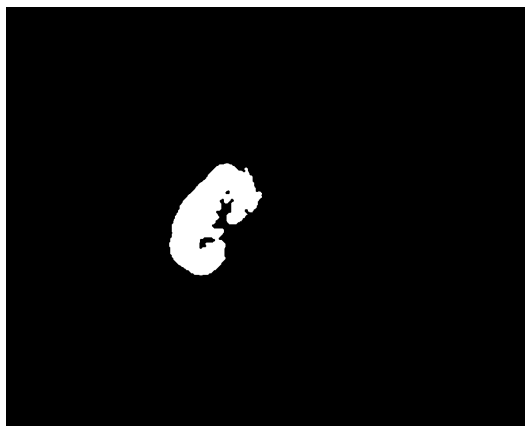
FIGURE 53 – (a) A late enhancement image to segment. (b) Manual segmentation. (c) Segmentation result with error 8.29% w.r.t the area of the manually segmented kidney. (d) Segmented kidney. (e) An image from the sequence where cortex and medulla can be identified best. (f) The resultant cortex and medulla segmentation based on (e). Gray level parts are the medulla structures and the rest is the cortex.



(a)



(b)



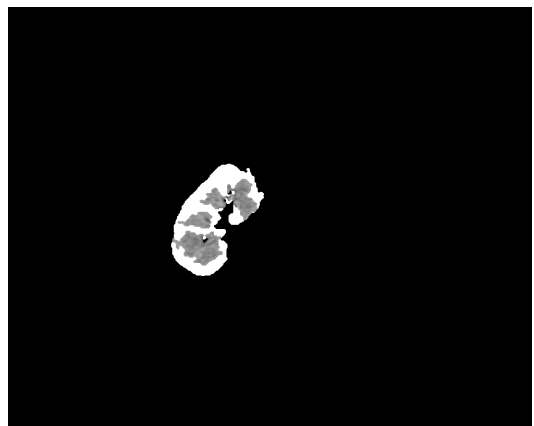
(c)



(d)



(e)

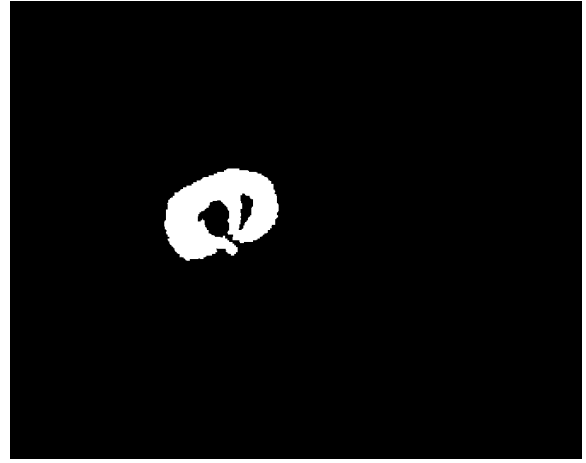


(f)

FIGURE 54–(a) A late enhancement image to segment. (b) Manual segmentation. (c) Segmentation result with error 12.19% w.r.t the area of the manually segmented kidney. (d) Segmented kidney. (e) An image from the sequence where cortex and medulla can be identified best. (f) The resultant cortex and medulla segmentation based on (e). Gray level parts are the medulla structures and the rest is the cortex.



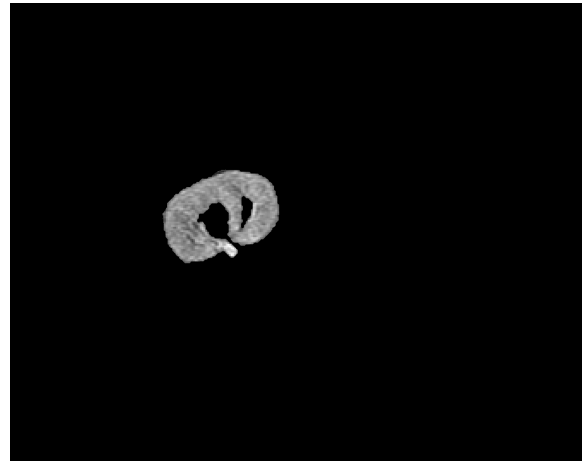
(a)



(b)

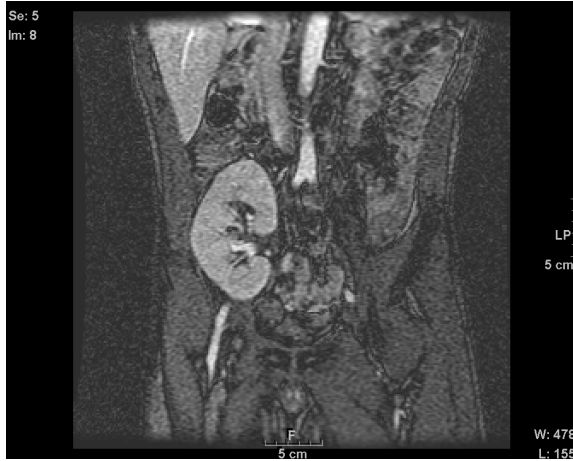


(c)

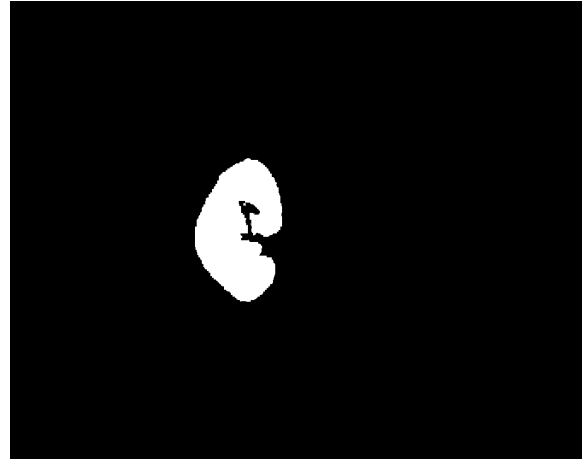


(d)

FIGURE 55 – (a) A late enhancement image to segment. (b) Manual segmentation. (c) Segmentation result with error 7.47% w.r.t the area of the manually segmented kidney. (d) Segmented kidney. In this patient, medulla was not identifiable.



(a)



(b)



(c)



(d)

FIGURE 56 – (a) A late enhancement image to segment. (b) Manual segmentation. (c) Segmentation result with error 6.32% w.r.t the area of the manually segmented kidney. (d) Segmented kidney. In this patient, medulla was not identifiable.

CHAPTER V

EVALUATION OF THE PERFUSION SIGNALS

After the breathing and movements are compensated via registration and the kidney is segmented from the surrounding anatomical structures, we would like to understand if the kidney is healthily accepted or if it is undergoing rejection. For this purpose, the mean gray level value for each region of interest (cortex and medulla) at each time point is calculated for the whole time-series of a patient's scans and it is plotted over time giving a 1D mean intensity vs. time signal. These signals are called perfusion curves or renograms: specifically, if the mean gray level is obtained only from the cortex, it is called a cortical renogram; or it is called a medullary renogram if the signal is obtained from the medulla of the kidney. A cortical renogram shows the Gd-DTPA concentration in the blood plasma, and a medullary curve represents the Gd-DTPA in the medullary vascular and medullary tubular phases [24]. Therefore, the enhancement pattern of the cortex as indicated by the cortical renogram tells how well the kidney is doing in glomerular filtration; whereas the pattern of a cortical renogram reflects the condition of the tubules [8]. Consequently, these separate renograms for the cortex and medulla bring the superiority of DCE-MRI to nuclear scans or other non-invasive methods, as DCE-MRI provides the ability to distinguish the diseases that affect the cortex (such as acute renal rejection and acute renal necrosis) from the diseases that affect primarily the medulla (such as toxic nephropathy) or the diseases that affect the medulla in the early stages (such as urinary tract obstruction and tubulointerstitial diseases) [9, 87].

As a first step to understand the patterns of the signals in such diseases, in this thesis, we focus on understanding the behavior of the renograms for normal and acute rejection transplants (as acute rejection is the most important type of renal dysfunction). The basics of the renogram patterns in healthy kidneys were introduced in Chap. II. Shortly summarizing, in normal transplants, *cortex* receives the contrast agent within the first 2–3 images (8–12 seconds) after the intravenous bolus injection of the contrast agent. Then the signal

intensity increases immediately in about 40 seconds, and reaches a maximum with the first 100 seconds. Afterwards, the signal starts to drop slowly to its initial value while the urine is formed [9, 18, 26]. *Medulla* receives the contrast agent after the glomerular filtration process, which is slow [9]. Therefore, the signal in the medulla increases 10–20 seconds after cortical enhancement, and reaches its maximum value within 20–30 seconds. The patterns of the medullary renograms generally follow the cortical renograms, but can somewhat be different reflecting the water reabsorption in the tubules & collecting ducts [27]. From this functional information, the most characteristic property of the cortical renograms can be listed as the rapid signal increase with a definite peak, and a slow decay; whereas, the medullary renograms don't show definite peaks and slowly reach a steady state following the cortical signals [88].

In acute rejection cases, in the 1980's in [89–91], the normal (non-enhanced) cortico-medullary differentiation was noted to decrease due to the lengthening of the T1 value of the cortex (probably because of tissue oedema). Coming to 1990's, Szolar *et al.* [18] had shown that the MR images show a delayed perfusion pattern and the cortical enhancement is reduced compared to normals. In [18] and [24], it was noted that in acute rejection patients, the increase in signal intensity (SI) occurred slowly in the cortex reaching its peak at the end of the time sequence, indicating an alteration of renal cortical microcirculation. In [88], the reduced cortical enhancement and the delayed peak of the cortical curve were confirmed, and also a slow constant uprise of the inner medullary curves were mentioned. In [92], maximum gradient, peak intensity, initial mean signal, and final and initial mean signal differences were found to be pathologic for acute rejection patients.

With this functional & anatomical information of the kidney, and with the review of the literature, we have been able to plot a basic figure (Fig. 57) illustrating the ideal cortical perfusion patterns of normal acute rejection kidneys in the extreme cases.

To plot the renograms, we propagate the prepared cortex and medulla masks over the time sequence while we calculate the average intensity on the cortex and on the medulla for each scan. Then we plot these average intensities for each scan as a function of time. Figure 58 shows the renograms of four patients: 1 normal, 2 acute rejection and 1 chronic glomerulopathy proved by biopsy. The normal patient shows the expected abrupt increase to the higher signal intensities and the valley with a small slope. The acute rejection patients show a delay in

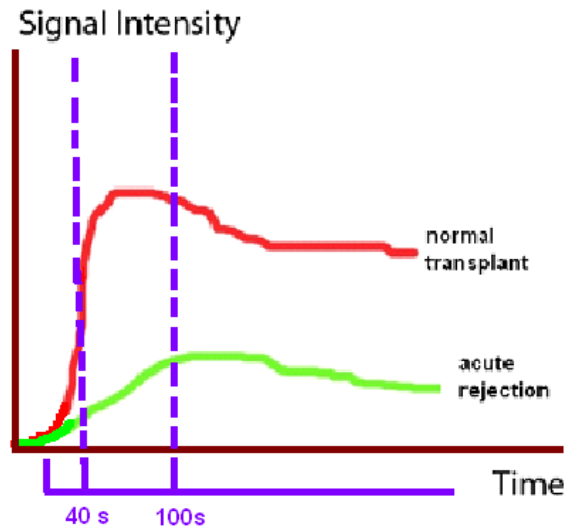


FIGURE 57– Ideal cortical perfusion patterns of normal and acute rejected kidneys

reaching their peak signal intensities.

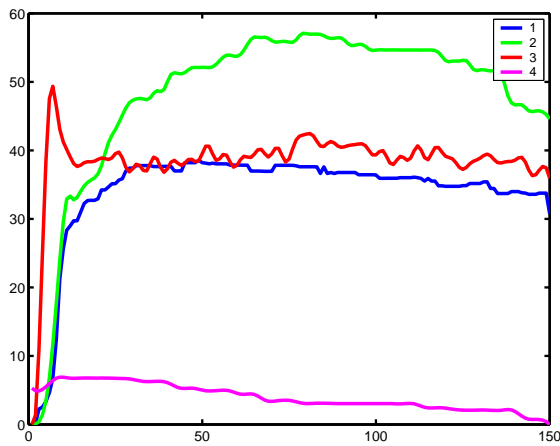
With these observations, we have determined the following parameters in cortical renograms to be of utmost importance in classification:

- Cortico-medullary contrast (CMC) [89]

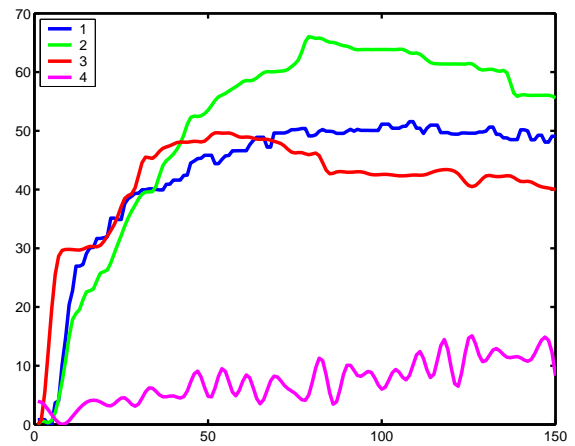
$$CMC = \frac{SI(cortex) - SI(medulla)}{SI(cortex) + SI(medulla)} \times 100\%$$

- Relative peak signal intensity = Maximum SI - Minimum SI
(i.e. the signal is normalized to start from zero values to cancel the bias of the MRI on the image intensity.)
- Time to peak signal intensity
- Maximum gradient = Relative peak signal intensity / Time to peak signal intensity
- Initial gradient = First peak signal intensity / Time to first peak signal intensity
- Final mean signal: The mean intensity after the signal reaches the steady state.

Also for the medullary renograms, again the time to peak signal intensity and the slope at the end of the acquisition are of utmost importance.



(a) Cortex intensity vs. scan number



(b) Medulla intensity vs. scan number

FIGURE 58—(a) Normalized cortex signals from 4 subjects. (b) Normalized medulla signals from 4 subjects. There are 4 seconds between each scan. Subjects 1&2 are acute rejection, subject 3 is normal and subject 4 is chronic glomerulopathy proved by biopsy. In the cortex curves, the normal patient shows the expected abrupt increase in intensity and the fast decrease, followed by a constant valley and a slow decrease. On the other hand, these abrupt patterns are not seen in acute rejection patients, there is no definite peak, and the time to reach the peak intensity is delayed. Also in medullary curves, the normal patient reaches the first peak faster than others. Subject 4 shows that DCE-MRI is also powerful to distinguish other diseases.

CHAPTER VI

CONCLUSIONS

Dynamic Contrast Enhanced Magnetic Resonance Imaging (DCE-MRI) is the only non-invasive test that provides high spatial and temporal resolution of a single kidney, and allows to evaluate the state of the cortex and medulla structures separately. To quantitatively analyze the DCE-MR images and to differentiate between acute rejection cases and normal transplants, this thesis introduced a general framework for image analysis. For motion compensation, mutual information registration has been used, and for segmentation, a novel deformable model algorithm has been proposed. At the final stage, the segmented kidney is propagated over the whole sequence, and average intensity vs. time signals are plotted. From these plots, a number of important image features have been extracted. While additional follow-up is necessary, this framework introduces a solid foundation for future development. The prepared software is ready to be tested by doctors in pure C++ language, and a user friendly graphical user interface (GUI) is designed with Qt (an open source library by Trolltech Inc.) to ease this process (see Figs. 59, 60 and 61). The whole project is compilable under Windows, Unix and Linux. Also, a web page is describing the project has been made available at: <http://www.cvip.louisville.edu/wwwcvip/frames/mainFrames/Research.htm>

Based on the experience gained from this thesis, the following future work (in both software and hardware) is believed to enhance the results:

- At the registration step, mutual information may fail due to the effect of the noise on the entropy, and so does edge detection. In this thesis, the kidney images were from transplants, so a big movement was not observed and registration did not play a crucial role. However, if the algorithms are to be applied to native kidneys to differentiate other diseases, more advanced noise-resistant registration algorithms would be needed.
- In the segmentation step, the temporal information of the images was used only during

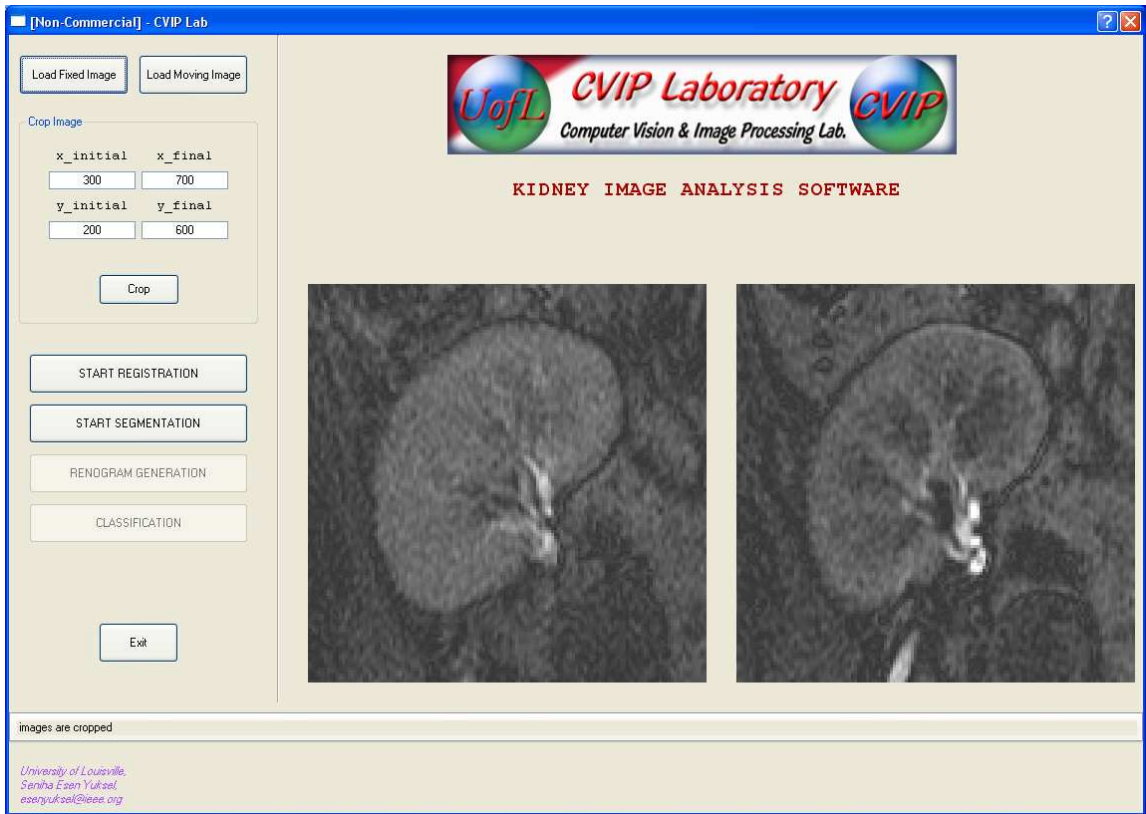


FIGURE 59 – Main page of the software

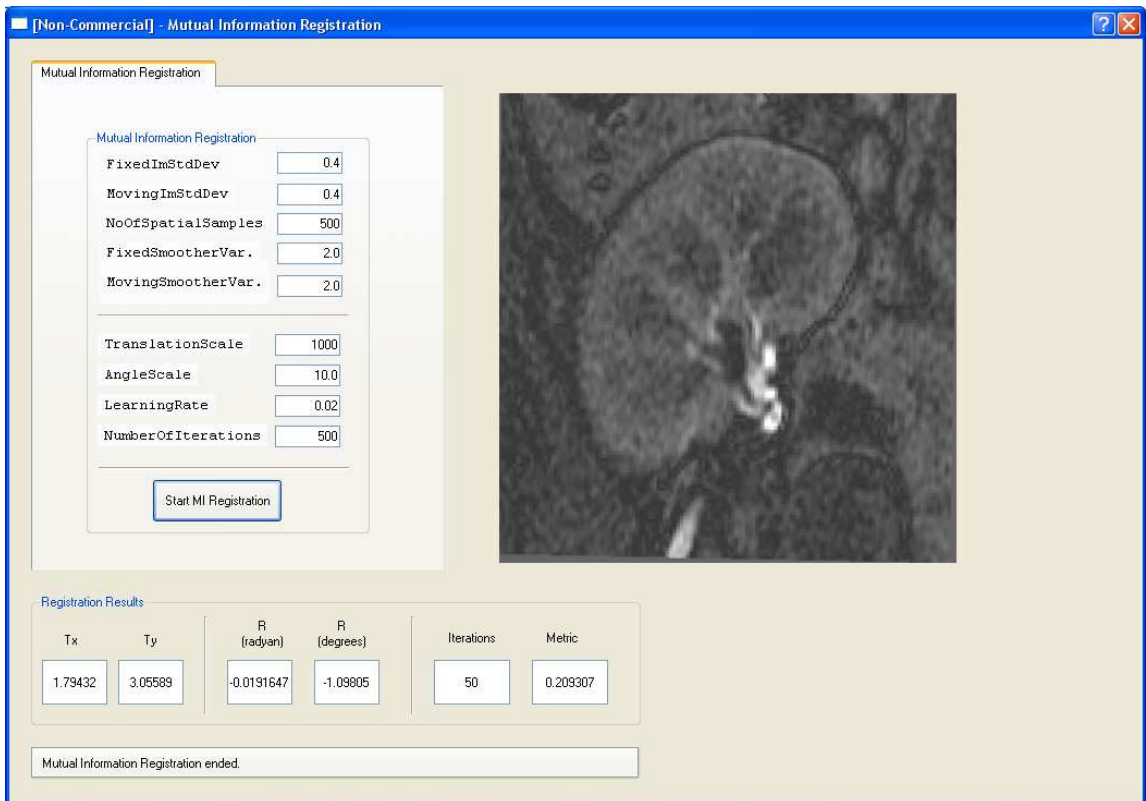


FIGURE 60 – Registration page of the software

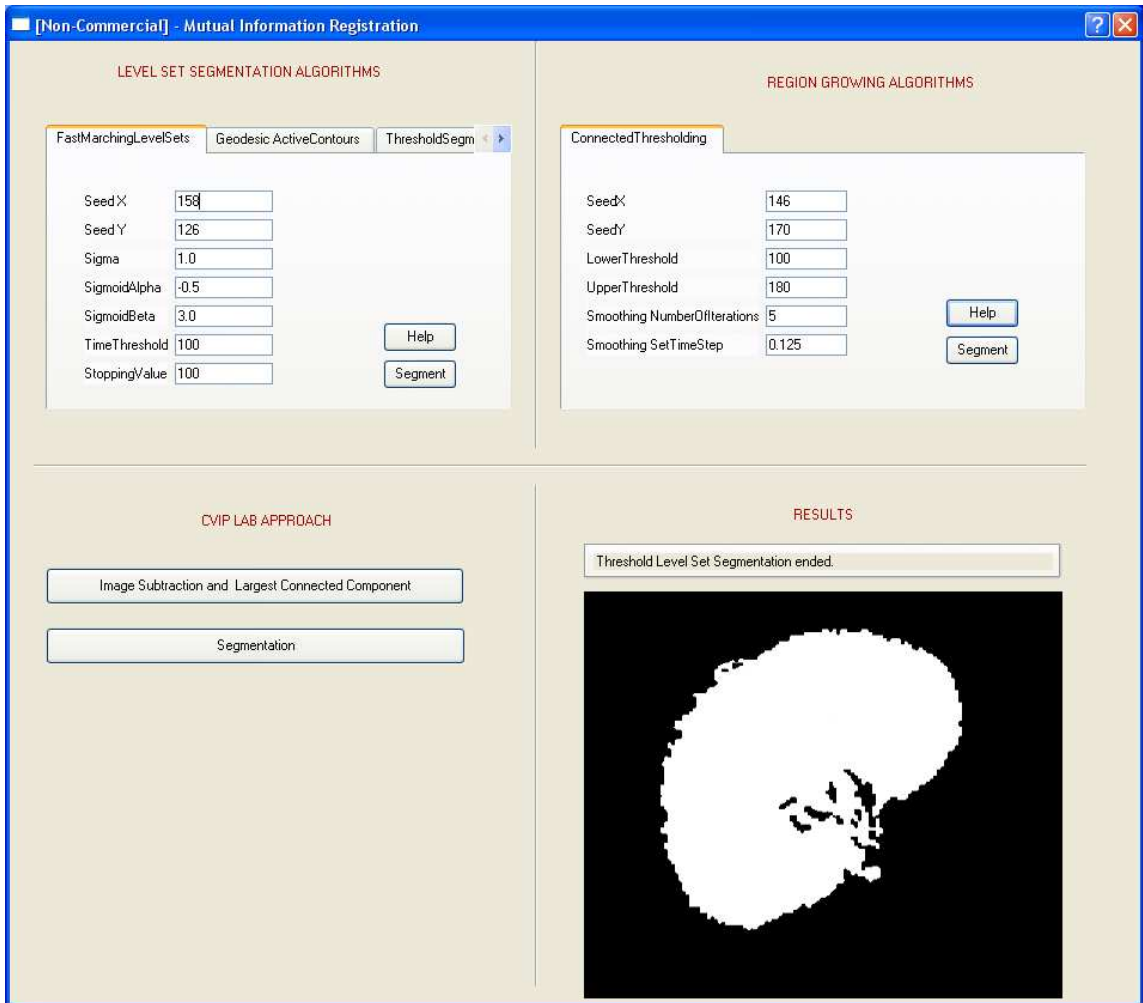


FIGURE 61 – Segmentation page of the software

the image subtraction phase. An algorithm that can segment each pixel based on its temporal behavior with relation to the temporal behavior of its spatial neighbors would be very helpful (such as a Random Markov field with included temporal information). Such methods would also allow better classification of the generally intermixed medullary and cortical tissue which are very hard to differentiate considering also the noise and the partial volume effects.

- In obtaining the perfusion curves, we averaged all the cortex tissue or all the medulla tissue. Separating the cortex into upper and lower cortex, or separating the medulla into outer and inner compartments might help in locating where the disease is occurring.
- In the classification step, with the evaluation of more patients, if the normal perfusion characteristics of the contrast agent can be formulated mathematically, deviations from this parametric curve would give a universal metric.
- For better statistical classifiers, the results of urine and blood tests, ultrasound and DCE-MRI can be combined. Especially, 3-D ultrasound imaging such as color Doppler and Power Doppler have found many studies in the renal allograft evaluation, and monitoring the patient daily with these easy to use imaging modalities may bring earlier detection of renal rejection – or least help to exclude other diseases from the diagnosis.
- With the evaluation of more patients, Dynamic MRI can be tested to diagnose other diseases such as acute tubular necrosis, cyclosporin toxicity or post-transplant lymphoproliferative disorders which show similar kind non-functioning after transplantation.
- To facilitate shorter scan times, new acquisition techniques have been proposed in the literature such as sensitivity encoding for MRI (SENSE), simultaneous acquisition of spatial harmonics (SMASH), sensitivity profiles from an array of coils for encoding and reconstruction in parallel (SPACE-RIP) and Reduced-Encoding Imaging by Generalized-series Reconstruction (RIGR). If DCE-MRI is going to be in clinical practice in the near future, such algorithms should be implemented in commercial equipments to handle rapid imaging with less noise.

This thesis introduced novel algorithms and gave very promising results; however, before

DCE-MRI can be put into medical practice, many more patients should be tested; DCE-MRI should be validated against acceptable standards; and much more should be done in both the image acquisition and in the image processing. With such further studies, we believe that DCE-MRI will have an important impact on the clinical management of patients with renal diseases.

REFERENCES

- [1] (2005) Kidney transplantation. Capital Health. [Online]. Available: <http://www.cdha.nshealth.ca/transplantservices/kidney.html>
- [2] (2005) Kidney transplant information guide. The Institute of Human Virology. [Online]. Available: <http://www.ihv.org/guides/images/kidney.jpg>
- [3] B. Russell, “Detailed structure of a nephron,” 2004. [Online]. Available: <http://ms.yuba.cc.ca.us/vet02/bio/photos/bio48.jpg>
- [4] *Your Kidneys and How They Work*, NIH Publication, National Kidney and Urologic Diseases Information Clearinghouse, July 2003. [Online]. Available: <http://kidney.niddk.nih.gov/kudiseases/pubs/yourkidneys/>
- [5] “2000 annual report of the U.S. scientific registry of transplant recipients and the organ procurement and transplantation network: Transplant data 1990-1999,” U.S. Department of Health and Human Services, Health Resources and Services Administration, Office of Special Programs, Division of Transplantation, Rockville, MD; United Network for Organ Sharing (UNOS), Richmond, VA, 2000.
- [6] R. Sharma, R. Gupta, H. Poptani, C. Pandey, R. Gujral, and M. Bhandari, “The magnetic resonance renogram in renal transplant evaluation using dynamic contrast-enhanced MR imaging,” *Radiology*, vol. 59, pp. 1405–1409, 1995.
- [7] B. Kasiske and W. Keane, *The kidney*, 5th ed. Philadelphia: PA Saunders, 1996, ch. 24, pp. 1137–1173.
- [8] H. Bennett and D. Li, “MR imaging of renal function,” *Magn Reson Imaging Clin N Am*, vol. 5(1), pp. 107–126, Feb 1997.
- [9] E. Giele, “Computer methods for semi-automatic MR renogram determination,” Ph.D. dissertation, Department of Electrical Engineering, Eindhoven University of Technology, Eindhoven, 2002.
- [10] A. Taylor and J. Nally, “Clinical applications of renal scintigraphy,” *AJR*, vol. 164, pp. 31–41, 1995.
- [11] R. Katzberg, M. Buonocore, M. Ivanovic, C. Pellot-Barakat, R. Ryan, K. Whang, J. Brock, and C. Jones, “Functional, dynamic and anatomic MR urography: feasibility and preliminary findings,” *Academic Radiology*, vol. 8, pp. 1083–1099, 2001.
- [12] M. Tublin, R. Bude, and J. Platt, “The resistive index in renal Doppler sonography: where do we stand?” *American Journal of Roentgenology*, vol. 180(4), pp. 885–892, 2003.

- [13] J. H. L. Chow, F. G. Sommer and K. Li, "Power Doppler imaging and resistance index measurement in the evaluation of acute renal transplant rejection," *J Clin Ultrasound*, vol. 29, pp. 483–490, 2001.
- [14] K. Turetschek, C. Nasel, P. Wunderbaldinger, K. Diem, K. Hittmair, and G. H. Mostbeck, "Power Doppler versus color Doppler imaging in renal allograft evaluation," *Journal of Ultrasound in Medicine*, vol. 15(7), pp. 517–522, 1996.
- [15] H. Trillaud, P. Merville, P. Tran Le Linh, J. Palussiere, L. Potaux, and N. Grenier, "Color Doppler sonography in early renal transplantation follow-up: resistive index measurements versus power Doppler sonography," *AJR Am J Roentgenol.*, vol. 171(6), pp. 1611–5, dec 1998.
- [16] D. Yang, Q. Ye, M. Williams, Y. Sun, T. C. C. Hu, D. S. Williams, J. M. F. Moura, and C. Ho, "USPIO enhanced dynamic MRI: Evaluation of normal and transplanted rat kidneys," *Magnetic Resonance in Medicine*, vol. 46, pp. 1152–1163, 2001.
- [17] K. Lorraine and C. Racusen, *Atlas of Diseases of the Kidney*. Current Medicine Inc., 1999, vol. 1, ch. 10. [Online]. Available: <http://www.kidneyatlas.org/>
- [18] D. Szolar, K. Preidler, F. Ebner, F. Kammerhuber, S. Horn, M. Ratschek, G. Ranner, P. Petritsch, and J. Horina, "Functional magnetic resonance imaging of the human renal allografts during the post-transplant period: preliminary observations," *Magnetic Resonance Imaging*, vol. 15(7), pp. 727 – 735, 1997.
- [19] L. Chan, *Atlas of Diseases of the Kidney*. Current Medicine Inc, 1999, vol. 5, ch. 9. [Online]. Available: <http://www.kidneyatlas.org/>
- [20] Z. Liang and P. C. Lauterbur, "An efficient method for dynamic magnetic resonance imaging," *IEEE Trans. on Medical Imaging*, vol. 13(4), pp. 677–686, Dec 1994.
- [21] D. C. Kimber, C. E. Gray, C. E. Stackpole, M. A. Miller, A. B. Drakontides, and L. C. Leavell, *Kimber-Gray-Stackpole's Anatomy and Physiology*. New York: Macmillan, 1977.
- [22] W. Kapit, R. Macey, and E. Meisami, *The Physiology Coloring Book*, C. M. Wilson, Ed. HarperCollins Publishers, 1987.
- [23] P. Choyke, J. Frank, M. Girton, S. Inscoe, M. Carvlin, J. Black, H. Austin, and A. Dwyer, "Dynamic Gd-DTPA-enhanced MR imaging of the kidney: experimental results," *Radiology*, vol. 170, pp. 713–720, 1989.
- [24] K. Preidler, D. Szolar, H. Schreyer, F. Ebner, R. Kern, H. Holzer, and J. Horina, "Differentiation of delayed kidney graft function with gadolinium-DTPA-enhanced magnetic resonance imaging and Doppler ultrasound," *Invest Radiol.*, vol. 31(6), pp. 364–71, Jun 1996.
- [25] J. Frank, P. Choyke, H. Austin, and M. Girton, "Functional MR of the kidney," *Magnetic Resonance in Medicine*, vol. 22(2), pp. 319–323, Dec 1991.
- [26] G. von Schulthess, W. Kuoni, G. Gerig, S. Duewell, and G. Krestin, "Semiautomated ROI Analysis in Dynamic MRI-Studies, Part II: Application to Renal Function Examination, First Experiences," *Journal of Computer Assisted Tomography*, pp. 733–741, 1991.
- [27] G. Krestin, "Magnetic resonance imaging of the kidneys: Current status," *Magnetic Resonance Quarterly*, vol. 10, pp. 2–21, 1994.

- [28] G. Krestin, G. Friedmann, and W. Steinbrich, "Gd-DTPA enhanced fast dynamic MRI of the kidneys and adrenals," *Diagn. Imaging Int*, vol. 4, pp. 40–44, 1988.
- [29] G. Krestin, G. Friedmann, and W. Steinbrich, "Quantitative evaluation of renal function with rapid dynamic gadolinium-DTPA enhanced MRI," Book of abstracts, Society of Magnetic Resonance in Medicine, p. 643, 1988.
- [30] J. Frank, P. Choyke, and M. Girton, "Gadolinium-DTPA enhanced dynamic MR imaging in the evaluation of cisplatin nephrotoxicity," *J. Comput Assist Tomogr*, vol. 13, pp. 448–459, 1989.
- [31] L. Knespova and G. Krestin, "Magnetic resonance in the assessment of renal function," *Eur Radiol.*, vol. 8, pp. 201–211, 1998.
- [32] Y. Sun, M. Jolly, and J. M. F. Moura, "Integrated registration of dynamic renal perfusion MR images," in *Proc. 2004 IEEE International Conference on Image Processing*, 2004, pp. 1923–1926.
- [33] P. Yim, H. Marcos, M. McAuliffe, D. McGarry, I. Heaton, and P. Choyke, "Registration of time-series contrast enhanced magnetic resonance images for renography," in *Proc. 14th IEEE Symp. Computer Based Medical Systems*, 2001, pp. 516–520.
- [34] Y. Sun, J. Moura, and C. Ho, "Subpixel registration in renal perfusion MR image sequence," in *Proc. 2004 IEEE Int. Symp. Biomedical Imaging*, 2004, pp. 700–703.
- [35] Y. Sun, J. Moura, D. Yang, Q. Ye, and C. Ho, "Kidney segmentation in MRI sequences using temporal dynamics," in *Proc. 2002 IEEE Int. Symp. Biomedical Imaging*, 2002, pp. 98–101.
- [36] G. Gerig, R. Kikinis, W. Kuoni, G. van Schulthess, and O. Kubler, "Semiautomated ROI analysis in dynamic MRI studies: Part I: image analysis tools for automatic correction of organ displacements," *IEEE Trans. Image Processing*, vol. 11:(2), pp. 221–232, 1992.
- [37] E. Giele, J. de Priester, J. Blom, J. den Boer, J. van Engelshoven, A. Hasman, and M. Geerlings, "Movement correction of the kidney in dynamic MRI scans using FFT phase difference movement detection," *J. Magn Reson Imaging*, vol. 14(6), pp. 741–749, Dec 2001.
- [38] R. Voshenrich, M. Kallerhoff, H. Grone, U. Fischer, M. Funke, L. Kopka, G. Siebert, R. Ringert, and E. Grabbe, "Detection of renal ischemic lesions using Gd-DTPA enhanced turbo Flash MRI: experimental and clinical results," *J. Comput Assist Tomogr*, vol. 20(2), pp. 236–243, Mar-Apr 1996.
- [39] H. Munechika, D. Sullivan, L. Hedlund, C. Beam, H. Sostman, R. Herfkens, and N. Pelc, "Evaluation of acute renal failure with magnetic resonance imaging using gradient-echo and Gd-DTPA," *Invest. Radiol.*, vol. 26(1), pp. 22–27, Jan 1991.
- [40] M. Carvlin, P. Arger, H. Kundel, L. Axel, L. Dougherty, E. Kassab, and B. Moore, "Acute tubular necrosis: use of gadolinium-DTPA and fast MR imaging to evaluate renal function in the rabbit," *J. Comput Assist Tomogr*, vol. 11(3), pp. 488–95, May-Jun 1987.
- [41] L. Dalla-Palma, G. Panzetta, R. Pozzi-Mucelli, G. Galli, M. Cova, and S. Meduri, "Dynamic magnetic resonance imaging in the assessment of chronic medical nephropathies with impaired renal function," *Eur Radiol*, vol. 10(2), pp. 280–286, 2000.

- [42] R. Kikinis, G. von Schulthess, P. Jager, R. Durr, M. Bino, W.Kuoni, and O. Kubler, "Normal and hydronephrotic kidney: evaluation of renal function with contrast-enhanced MR imaging," *Radiology*, vol. 165(3), pp. 837–42, Dec 1987.
- [43] R. Semelka, H. Hricak, E. Tomei, A. Floth, and M.Stoller, "Obstructive nephropathy: evaluation with dynamic Gd-DTPA-enhanced MR imaging," *Radiology*, vol. 175, pp. 797–803, 1990.
- [44] N. Beckmann, J. Joergensen, K. Bruttel, M. Rudin, and H. Schuurman, "Magnetic resonance imaging for the evaluation of rejection of a kidney allograft in the rat," *Transpl Int.*, vol. 9(3), pp. 175–83, 1996.
- [45] T. El-Diasty, O. Mansour, and A. Farouk, "Diuretic contrast enhanced mru versus ivu for depiction of non dilated urinary tract," *Abd Imaging*, vol. 28, pp. 135–145, 2003.
- [46] D. Laurent, K. Poirier, J. Wasvary, and M. Rudin, "Effect of essential hypertension on kidney function as measured in rat by dynamic MRI," *Magn. Reson. Med.*, vol. 47(1), pp. 127–131, Jan 2002.
- [47] Y. Sun, "Registration and segmentation in perfusion mri: Kidneys and hearts," Ph.D. dissertation, Dept. of Elect. and Comp. Eng., Carnegie Mellon University, Pittsburg, 2004.
- [48] J. de Priester, A. Kessels, E. Giele, J. den Boer, M. Christiaans, A. Hasman, and J. van Engelshoven, "MR renography by semiautomated image analysis: performance in renal transplant recipients," *J. Magn Reson Imaging*, vol. 14(2), p. 134140, Aug 2001.
- [49] Y. Boykov, V. Lee, H. Rusinek, and R. Bansal, "Segmentation of dynamic N-D data sets via graph cuts using Markov models," in *Proceedings of the 4th International Conference on Medical Image Computing and Computer-Assisted Intervention (MICCAI)*, 2001, pp. 1058–1066.
- [50] Y. Sun, D. Yang, Q. Ye, M. Williams, J. Moura, F. Boada, Z. Liang, and C. Ho, "Improving spatiotemporal resolution of USPIO-enhanced dynamic imaging of rat kidneys," *Magnetic Resonance Imaging*, vol. 21, pp. 593–598, 2003.
- [51] T. F. Chan and L. Vese, "Active contours without edges," *IEEE Trans. on Image Processing*, vol. 10(2), pp. 266–277, Feb 2001.
- [52] F. Maes, A. Collignon, D. Vandermeulen, G. Marchal, and P. Suetens, "Multimodality image registration by maximization of mutual information," *IEEE transactions on Medical Imaging*, vol. 16, no. 2, pp. 187–198, 1997.
- [53] A. Collignon, F. Maes, D. Delaere, D. Vandermeulen, P. Seutens, and G. Marchal, "Automated multimodality image registration using information theory," in *Proceedings of Information Processing in Medical Images*, 1995, pp. 263–274.
- [54] P. Viola and W. Wells, "Alignment by maximization of mutual information," in *Proc. 5th Int. Conf. Computer Vision*, 1995, pp. 16–23.
- [55] F. Maes, D. Vandermeulen, and P. Suetens, "Comparative evaluation of multiresolution optimization strategies for multimodality image registration by maximization of mutual information," *Medical Image Analysis*, vol. 3, pp. 373–386, 1999.

- [56] J. Pluim, J. Maintz, and M. Viergever, “Mutual information based registration of medical images: A survey,” *IEEE Trans on Medical Imaging*, vol. 22, no. 8, pp. 986–1004, Aug 2003.
- [57] C. Studholme, D. L. G. Hill, and D. J. Hawkes, “An overlap invariant entropy measure of 3d medical image alignment,” *Pattern Recognition*, vol. 32, no. 1, pp. 71–86, 1999.
- [58] C.-L. Tsai, “Overview of mutual information registration,” lecture notes, July 2003.
- [59] J. R. Filho, P. Treleaven, and C. Alippi, “Genetic-algorithm programming environments,” *Computer*, vol. 27, no. 6, pp. 28–43, 1994.
- [60] J. H. Holland, *Adaptation in natural and artificial systems*. Cambridge, MA, USA: MIT Press, 1992.
- [61] M. Srinivas and L. Patnaik, “Genetic algorithms: A survey,” *Computer*, vol. 27, no. 6, pp. 17–26, 1994.
- [62] J. Heitkotter and D. Beasley, “Hitch hiker’s guide to evolutionary computation,” 2000. [Online]. Available: <http://www.cs.bham.ac.uk/Mirrors/ftp.de.uu.net/EC/clife/www/>
- [63] R. O. Duda, P. E. Hart, and D. G. Stork, *Pattern Classification*, 2nd ed. Wiley-Interscience, 2000.
- [64] J. Grefenstette, “Optimization of control parameters for genetic algorithms,” *IEEE Trans. Syst. Man Cybern.*, vol. 16, no. 1, pp. 122–128, 1986.
- [65] K. A. D. Jong and W. M. Spears, “An analysis of the interacting roles of population size and crossover in genetic algorithms,” in *PPSN I: Proceedings of the 1st Workshop on Parallel Problem Solving from Nature*, 1991, pp. 38–47.
- [66] A. Potvin, “Matlab-GA,” Genetic algorithms toolbox for Matlab, 1993. [Online]. Available: <http://www.wior.uni-karlsruhe.de/bibliothek/Genetic/non/matlabga>
- [67] L. Ibanez, W. Schroeder, L. Ng, J. Cates, and the Insight Software Consortium, *The ITK Software Guide*. Kitware, Inc., Jun 2005. [Online]. Available: <http://www.itk.org/>
- [68] A. W. M. Kass and D. Terzopoulos, “Snakes: Active contour models,” *Int. J. Computer Vision*, vol. 1, pp. 321–331, 1987.
- [69] D. J. Williams and M. Shah, “A fast algorithm for active contours and curvature estimation,” *CVGIP: Image Underst.*, vol. 55, no. 1, pp. 14–26, 1992.
- [70] J. Ivins and J. Porrill, “Everything you always wanted to know about snakes (but were afraid to ask),” Artificial Intelligence Vision Research Unit, University of Sheffield, AIVRU Technical Memo 86, Mar 2000.
- [71] C. Xu and J. Prince, “Gradient vector flow demonstration using matlab,” Matlab code, Jun 1997. [Online]. Available: <http://iacl.ece.jhu.edu/projects/gvf/>
- [72] J. Sethian, *Level Set Methods and Fast Marching Methods*. Cambridge University Press, 1996.
- [73] V. Caselles, R. Kimmel, and G. Sapiro, “Geodesic active contours,” *Int. J. Comput. Vision*, vol. 22, no. 1, pp. 61–79, 1997.

- [74] M. Rousson and N. Paragios, “Shape priors for level set representations,” in *ECCV '02: Proceedings of the 7th European Conference on Computer Vision-Part II*, 2002, pp. 78–92.
- [75] M. Leventon, W. L. Grimson, , and O. Faugeras, “Statistical shape influence in geodesic active contours,” in *Proc. IEEE CVPR*, 2000, pp. 1316–1324.
- [76] Y. Chen, S. Thiruvenkadam, H. Tagare, F. Huang, and D. Wilson, “On the incorporation of shape priors into geometric active contours,” in *Proc. IEEE VLISM*, 2001, pp. 145–152.
- [77] A. Tsai, A. J. Yezzi, W. M. W. III, C. Tempany, D. Tucker, A. Fan, W. E. L. Grimson, and A. S. Willsky, “Model-based curve evolution technique for image segmentation,” in *Proc. IEEE CVPR*, 2001, pp. 463–468.
- [78] N. Paragios, “A level set approach for shape-driven segmentation and tracking of the left ventricle,” *IEEE Trans. on Medical Imaging*, vol. 22, pp. 773–776, 2003.
- [79] A. Litvin and W. Karl, “Levelset based segmentation using data driven shape prior on feature histograms,” in *IEEE Workshop on Statistical Signal Processing*, 2003, pp. 166–169.
- [80] A. Tsai, W. Wells, S. Warfield, and A. S. Willsky, “Level set methods in an em framework for shape classification and estimation,” in *Proceedings of the International Conference on Medical Image Computing and Computer-Assisted Intervention (MICCAI)*, 2004, pp. 1–9.
- [81] J. Yang and J. Duncan, “3d image segmentation of deformable objects with joint shape-intensity prior models using level sets,” *Medical Image Analysis*, vol. 8, pp. 285–294, 2004.
- [82] A. A. Farag, A. El-Baz, and G. Gimel’farb, “Density estimation using modified expectation-maximization for a linear combination of gaussians,” in *Proc. IEEE Int. Conf. Image Processing*, vol. 3, 2004, pp. 1871 – 1874.
- [83] A. Farag, A. El-Baz, and G. Gimel’farb, “Precise segmentation of multi-modal images,” *IEEE Transactions on Image Processing*, to be published.
- [84] G. Gimel’farb, A. A. Farag, and A. El-Baz, “Expectation-maximization for a linear combination of gaussians,” in *Proc. of International Conference on Pattern Recognition*, vol. 3, 2004, pp. 422 – 425.
- [85] T. Moon, “The expectation-maximization algorithm,” *IEEE Signal Processing Mag.*, vol. 13, pp. 47–60, Nov 1996.
- [86] R. Redner and H. F. Walker, “Mixture densities, maximum-likelihood estimation and the em algorithm (review),” *SIAM Rev.*, vol. 26, no. 2, pp. 195–237, 1984.
- [87] R. Semelka, K. Corrigan, S. Ascher, J. Brown, and R. Colindres, “Renal corticomedullary differentiation: observation in patients with differing serum creatinine levels,” *Radiology*, vol. 190, pp. 149–152, 1994.
- [88] Y. J. Wang and S. Morcos, “Magnetic resonance imaging and renal function,” *Kidney Forum*, pp. 59–63, 2000.
- [89] L. te Strake, L. Kool, L. Paul, A. Tegzess, J. Weening, J. Hermans, J. Doornbos, R. Bluemmel, and J. Bloem, “Magnetic resonance imaging of renal transplants: its value in the differentiation of acute rejection and cyclosporin A nephrotoxicity,” *Clin Radiol.*, vol. 39(3), pp. 220–228, May 1988.

- [90] M. Geisinger, B. Risius, M. Jordan, M. Zelch, A. Novick, and C. George, "Magnetic resonance imaging of renal transplants," *American Journal of Roentgenology*, vol. 143, pp. 1229 – 1234, 1984.
- [91] L. Schultze, L. te Strake, L. Paul, A. Tegzess, J. Bloem, and J. et.al., "Magnetic resonance imaging of renal transplants," in *Proceedings of the European Dialysis and Transplant Association*, vol. 22, 1985, pp. 609 – 613.
- [92] A. Agildere, N. Tarhan, G. Bozdagi, A. Demirag, E. Niron, and M. Haberal, "Correlation of quantitative dynamic magnetic resonance imaging findings with pathology results in renal transplants: A preliminary report," *Transplantation Proceedings*, vol. 31(8), pp. 3312–3316, Dec 1999.

APPENDICES I

GENETIC ALGORITHMS

Mutual information gives a quantitative measure of the spatial alignment between the two images; and in the case of optimum alignment, mutual information is maximized. To find this optimum alignment, the best translation and rotation parameters should be searched within the solution space.

The search methods in the literature can be classified into three titles; (i) Enumerative Techniques, (ii) Direct Methods (such as Fibonacci, Newton) and, (iii) Guided Random Search Techniques (such as Simulated Annealing and Genetic Algorithms) [59]. Among these methods, genetic algorithms (GA), first introduced by Holland [60], are general-purpose, domain independent, adaptive and robust search algorithms that mimic the evolution in nature where the fittest individuals survive through selection, crossover and mutation mechanisms [59, 61]. Genetic Algorithms select a group of candidate solutions (population) from the search space, crossover the fittest of these solutions to make fitter solutions. They also allow mutations to these solutions, which introduces new solutions to the system to avoid the local maximum points. Therefore, in a reasonable amount of time, Genetic Algorithms (GA) can provide a very close solution to the global optimum.

In computer environments, a GA generates an initial population, and each element of this population is encoded into a string (chromosome), which is the solution to the problem. Therefore, to find the best solution, this chromosome is manipulated in a cycle of stages as listed [59]:

1. Create a population of strings (chromosomes),
2. Evaluate the fitness of all the individuals (strings) in the population,
3. Select the best strings from the fitness values,

4. Create a new population by genetic manipulation of the strings using reproduction, crossover and mutation.

Step-1 in the above cycle is illustrated in Fig. I(a), with a population of four chromosomes represented by 0's and 1's. Each of these chromosomes is a potential solution to the problem, and to select the best solutions, a fitness function is calculated for each chromosome. The fitness function is the objective function, i.e., it is the function to be optimized, so the higher the fitness of a chromosome, the better the solution is, which is just like in nature where the fitter individuals have higher chances of survival.

Step-3 of the above cycle is the selection process, where the fittest individuals survive while the weaker ones perish. The selection of the chromosomes occurs actually during the mating process as in Fig. I(b). Each string is allocated a slot in a roulette wheel, where the slot size is proportional to the strength (normalized fitness value) of that string. The decision of which individuals mate with each other is made by rotating this wheel. Therefore, the probability that the fitter individuals will mate is higher than the probability of the mating of the weak individuals, which decreases the occurring of the weaker strings. Assuming that L is the string length, a c value between 1 to L is randomly picked for each mating pair to determine the cross-over point between the mating pairs. At the same time a P_c value is selected between $[0,1]$ to decide if the cross-over will happen or not [61]. Pursuant to these two parameters, the pairs exchange their genetic information as shown in Fig. I(b).

After crossover, strings are subject to mutation, the flipping of the bit from 0 to 1 or vice versa, with mutation probability P_m . Mutation is very important in introducing the lost genetic material; such as, if after crossover, all the bits were 0, then mutation can bring back a 1 to the population.

To summarize all these processes in an example, in Fig. I, the fitness function is selected as $f = x^2$ over the interval $[0-31]$, where x is the five-digit binary string. For each string (chromosome), the strength is calculated, the normalized value of each fitness values by the total fitness of the population. Obviously, for this fitness function, the highest fitness value is 100%; and one would expect the fitness to increase from generation to generation in the GA cycle. As expected, going from Fig. I (a) to (c), the least fitted solution is discarded and better solutions are formed. In this thesis however, the fitness function is the Mutual Information

as explained in the previous chapter, the maximization of which gives the best alignment for registration.

The pseudo code below from [62] and [63] describes the process as a whole :

BASIC GENETIC ALGORITHM:

```
BEGIN
Initialize Population {
     $F_d$  ( desired fitness)
     $P_c$  (Crossover Probability)
     $P_m$  (Mutation Probability)
     $L$  N-bit chromosomes
}
DO
    Determine the fitness of each chromosome,  $f_i, i = 1, \dots, L$ 
    Rank the chromosomes
    DO
        Select two chromosomes with highest score
        Crossover the pair at a randomly chosen bit
        Mutate each bit with probability  $P_m$ 
        Remove the parent chromosomes
    UNTIL N offsprings have been generated
UNTIL any chromosome's score  $f$  exceeds  $F_d$ 
RETURN highest fitness chromosome (best classifier)
END
```

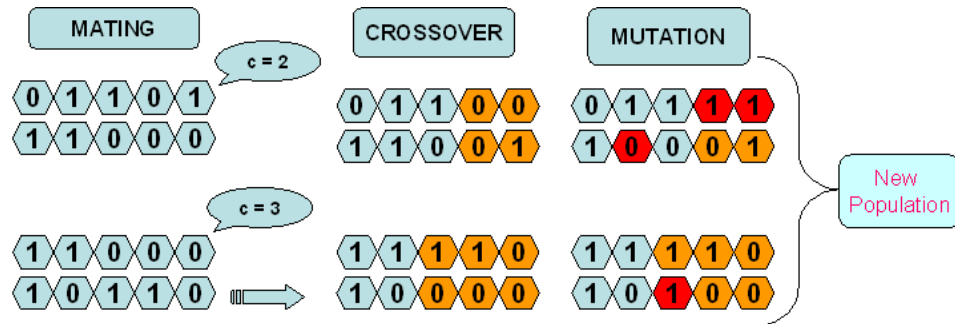
Control Parameters:

As explained in the above section, there are three parameters that need to be adjusted for each population; the population size, the mutation rate and the crossover rate. These three variables are the control parameters of the Genetic Algorithms. In general, genetic algorithms are better than gradient search methods if your search space has many local optima; however,

POPULATION P1	X	FITNESS (X ²)	STRENGTH (Percent of Total)
0 1 1 0 1	13	169	14.4
1 1 0 0 0	24	576	49.2
0 1 1 0 0	8	64	5.5
1 0 1 1 0	19	361	30.9

Eliminated by selection

(a) Initial Population P1 and Selection



(b) Crossover and Mutation

NEW POPULATION P2	X	FITNESS (X ²)	STRENGTH (Percent of Total)
0 1 1 1 1	15	225	12
1 0 0 0 1	17	289	16
1 1 1 1 0	30	900	49.6
1 0 1 0 0	20	400	22

(c) Second Generation P2

FIGURE 62 – A cycle of the Genetic Algorithms

TABLE 5
PARAMETERS USED IN GENETIC ALGORITHMS

Crossover rate	Mutation rate	Population size	Maximum generations	Number of bits
0.9	0.01	30	100	5

the choice of the control parameters highly effects the outcome. The trade-offs of changing the control parameters can be summarized as [61]:

1. Increasing the crossover probability increases the recombination rate, however, it also allows to increase the disruption of good strings.
2. Increasing the mutation probability tends to shift the genetic search into a random search, but it also allows to reintroduce new genetic material.
3. Increasing the population size increases the diversity and reduces the probability that the GA will converge to a local optimum, but it also increases the computation time.

Since the choice of these control parameters is critical, [64, 65] have introduced two distinct parameter sets that guarantee good performance on carefully chosen testbeds of objective functions. These two parameters sets are:

1. crossover rate: 0.9, mutation rate: 0.01, population size: 30 [64].
2. crossover rate: 0.6, mutation rate: 0.001, population size: 100 [65].

For the implementation of Genetic Algorithms, a number of software packages are available on the web as listed in [62]; one of which is the Matlab-GA code from Mathworks that is being used in this thesis. The parameters of [64] (as given above) were adopted with *maximumgenerations* = 100 in our study. For encoding, 5 bits were given (i.e. bits = [5 5 5]) for translation in x and y and for rotation θ . The stopping criterion of the GA was chosen as (i) if a fixed number of generations are reached (ii) a string with a certain high fitness value is located.

APPENDICES II

DERIVATIVES AND GRADIENTS

Discrete derivatives of a function of one variable can be obtained from the binomial series of a Pascal's Triangle an illustration of which is given in Fig. 63:

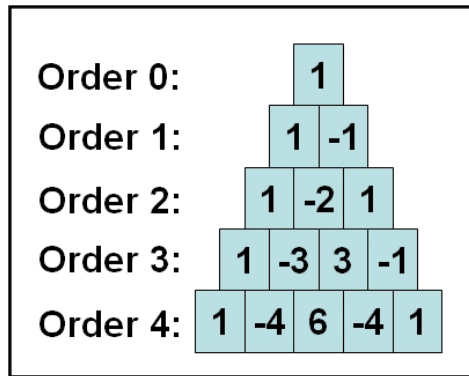


FIGURE 63: Pascal's Triangle and the signs assigned to each entry.

Let $v(s)$ be a function that can be represented in the discrete domain as an array of nodes as shown in Fig. 64. From Pascal's triangle, the second and fourth order derivatives of a function $v(s)$ is given by [70]:

$$v''(s) = v(s - 1) - 2v(s) + v(s + 1)$$

$$v''''(s) = v(s - 2) - 4v(s - 1) + 6v(s) - 4v(s + 1) + v(s + 2)$$

To calculate image gradients, simple image processing masks for first and second order derivatives are:

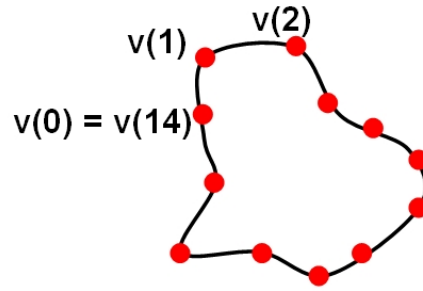


FIGURE 64 – Function $v(s)$ can be represented as an array of nodes, where the last node $v(N)$ is equal to the first node $v(0)$.

$$\frac{\partial}{\partial x} \approx [+1 \ 0 \ 1] \qquad \frac{\partial}{\partial y} \approx \begin{bmatrix} +1 \\ 0 \\ -1 \end{bmatrix}$$

$$\frac{\partial^2}{\partial x^2} \approx [+1 \ -2 \ 1] \qquad \frac{\partial^2}{\partial y^2} \approx \begin{bmatrix} +1 \\ -2 \\ +1 \end{bmatrix}$$

$$\frac{\partial^2}{\partial x \partial y} \approx \frac{1}{4} \begin{bmatrix} -1 & 0 & +1 \\ 0 & 0 & 0 \\ +1 & 0 & -1 \end{bmatrix}$$

APPENDICES III
KASS'S ACTIVE CONTOURS ALGORITHM

The energy functional introduced by Kass *et al.* in [68] is given as:

$$E = \int_s \alpha(s)|v'(s)|^2 + \beta(s)|v''(s)|^2 + E_{ext}(v(s)) ds \quad (35)$$

where α and β are some weights to control the curve's continuity and curvature, and E_{ext} is the gradient of the image:

$$\begin{aligned} E_{ext}(v(s)) &= -|\nabla \mathbf{Y}(v(s))|^2 \quad \text{or} \\ &= -|\nabla [G(v(s)) * \mathbf{Y}(v(s))]|^2 \end{aligned} \quad (36)$$

where \mathbf{Y} is a grayscale image, $G(\dots)$ is a 2D Gaussian kernel and ∇ is the gradient operator.

In this formulation, if $\alpha = 0$ at a point, a discontinuity can occur, or if α is too large, the contour may jump over the edge and hence not detect it. In the practical implementations, $\alpha(s) = \alpha$ and $\beta(s) = \beta$ are assumed to be constants, and variational calculus (explained in detail in [70]) to minimize this energy equation leads to the Euler equation:

$$\beta v^{(4)} - \alpha v'' = \nabla E_{ext} \quad (37)$$

where the derivatives of v can be approximated with finite differences (as explained in Appendix II.) giving two equations for $x(s)$ and $y(s)$:

$$\begin{aligned} \beta(x_{s-2} - 4x_{s-1} + 6x_s - 4x_{s+1} + x_{s+2}) - \alpha(x_{s-1} - 2x_s + x_{s+1}) &= f_x(x, y) \\ \beta(y_{s-2} - 4y_{s-1} + 6y_s - 4y_{s+1} + y_{s+2}) - \alpha(y_{s-1} - 2y_s + y_{s+1}) &= f_y(x, y) \end{aligned} \quad (38)$$

Here, $x(s)$ and $y(s)$ are the coordinates of the snake elements as shown in Fig.64; f_x and f_y are the gradient image forces.

Writing these equations in the forms of $\mathbf{A} \mathbf{x} = \mathbf{f}_x$ and $\mathbf{A} \mathbf{y} = \mathbf{f}_y$ where \mathbf{A} is a pentadiagonal circulant matrix, x and y can be solved iteratively with small time steps τ . According to the image forces at time $t - 1$, the new positions of the contour points at time t would be:

$$\begin{aligned} \mathbf{x}_t &= (\mathbf{A} + \tau \mathbf{Y})^{-1} (x_{t-1} - f_x(x_{t-1}, y_{t-1})) \\ \mathbf{y}_t &= (\mathbf{A} + \tau \mathbf{Y})^{-1} (y_{t-1} - f_y(x_{t-1}, y_{t-1})) \end{aligned} \tag{39}$$

A Matlab code implementing this algorithm is given by Xu and Prince on their website in [71]. In this algorithm, there are several points to consider such as, the initialization of the contour is manual and the algorithm can handle only geometrically simple objects. Moreover, the elastic energy component depends only on the first derivative of the contour, which is the difference between points. Therefore, minimizing the energy also corresponds to decreasing the distance between the points, causing the points to bunch up together on strong areas of the contour.

APPENDICES IV
WILLIAMS'S ACTIVE CONTOURS ALGORITHM

Noting the problems with the bunching up of contour points and the numerical instabilities of the Kass *et al.* solution, a more stable approach was introduced by William and Shah in [69]. In Williams *et al.* approach, a different formulation of the continuity term ($E_{elastic}$) is used so that the contours are more evenly spaced. In addition, Williams *et al.* also introduced a greedy algorithm in which each point of the contour is moved within a small neighborhood (e.g., 3x3) to the point which minimizes the energy functional.

In Williams *et al.*'s approach in [69], the energy is represented as:

$$E = E_{\text{int}} + E_{\text{ext}} = \int_0^1 (\alpha(s) E_{\text{elastic}} + \beta(s) E_{\text{bending}} + \gamma(s) E_{\text{image}}) ds \quad (40)$$

where α , β and γ are the weighting parameters and the energies are:

$$\begin{aligned} E_{\text{elastic}} &= \bar{d} - |v_i - v_{i-1}| \\ E_{\text{bending}} &= |v_{i-1} - 2v_i + v_{i+1}|^2 \\ E_{\text{image}} &= -|\nabla [G(v(s)) * \mathbf{I}(v(s))]|^2 \end{aligned} \quad (41)$$

with \bar{d} denoting the average distance between points.

This formulation pretty much looks like Kass *et al.*'s formulation, but differs in two points. First, the elastic term is modified to be the difference between the average distance between points (\bar{d}) and the distance between two consecutive points. By this way, the points that are closest to the average distance have the minimum value; so the points do not shrink into one region. The second difference is, William *et al.* calculated the curvature (E_{bending}) at each iteration for each point by a Greedy algorithm, and updated the β parameter so that the corners can be detected. The curvature at each point is given by:

$$c(s) = \left| \frac{\vec{u}(s)}{|\vec{u}(s)|} - \frac{\vec{u}(s+1)}{|\vec{u}(s+1)|} \right|^2 \quad (42)$$

where

$$\begin{aligned}\vec{u}(s) &= (x(s) - x(s-1), y(s) - y(s-1)) \\ \vec{u}(s+1) &= (x(s+1) - x(s), y(s+1) - y(s))\end{aligned}\tag{43}$$

If the curvature is a curvature maximum, then $\beta(s)$ is set to zero for the following iteration to allow a corner; otherwise, it is set to one. A pseudocode for this algorithm is given below:

William and Shah Active Contours Algorithm:

```
BEGIN
  Initialize {  $\alpha_i$ ,  $\beta_i$  and  $\gamma_i$  to 1 for all  $i$  }
  Initialize {  $threshold_1$  and  $threshold_2$  }
DO
  FOR each snake point
    Calculate the value of the energy function for the neighboring
    positions around the snake point, then move the point to the
    position with minimum energy
  FOR each snake point
    Calculate the curvature estimate from Eq. (42)
    IF the curvature is bigger than the curvature of the neighbors
    ANDIF the curvature is larger than a  $threshold_1$ 
    ANDIF the edge magnitude is larger than a  $threshold_2$ 
    THEN
      set  $\beta_i = 0$  to allow a corner
    ELSE
      set  $\beta_i = 1$ 
END
```

Compared to Kass approach, Williams approach is able to handle the curvature points better, but it provides only a local solution requiring very carefully selected initial contours. Yet, the objects this algorithm can successfully segment are still very simple.

CURRICULUM VITA

NAME: Seniha Esen Yuksel

ADDRESS: Department of Electrical and Computer Engineering,
University of Louisville,
Louisville, KY 40292.
<http://www.cvip.louisville.edu/~esen>
esenyuksel @ ieee.org

EDUCATION: B.S., Electrical and Electronics Engineering
Middle East Technical University, Ankara, Turkey, 2003

HONORS and AWARDS:

Awarded with a full assistantship by the CVIP Lab, 2003-2005.

First place award in Research!Louisville, 2005.

IEEE Student Member; 2001 - Present.

Society of Women Engineers, Student Member; 2004 - Present.

MICCAI Society member; 2005 - Present.

UofL Graduate Student Council, Senator; 2004 - 2005.

Eta Kappa Nu member; 2004 - Present.

Phi Kappa Phi member; 2004 - Present.

WORK EXPERIENCE:

Research Assistant, Comp. Vision and Image Proc. Lab, 2003-2005.

Intern Engineer, Ayesas Software and Electronics, Summer 2002.

Intern Engineer, Basari Electronics, Summer 2002.

Intern Engineer, Aselsan Inc., Summer 2001.

PUBLICATIONS:

1. A. El-Baz, **S.E. Yuksel**, H. Shi, A. A. Farag, M.A. El-Ghar, T. Eldiasty, and M. A. Ghoneim, "2D and 3D Shape Based Segmentation Using Deformable Models," Proc. of International Conference on Medical Image Computing and Computer-Assisted Intervention (MICCAI), California, 2005, pp. 821-829.
2. **S.E. Yuksel**, A. El-Baz, A.A. Farag, M.E.A. El-Ghar, T.A. Eldiasty, and M.A. Ghoneim, "Automatic detection of renal rejection after kidney transplantation," Proc. of Computer Assisted Radiology and Surgery (CARS), 2005, pp. 773-778.
3. A. El-Baz, **S.E. Yuksel**, S. Elshazly, and A. A. Farag, "Non-rigid registration techniques for automatic follow-up of lung nodules," Proc. of Computer Assisted Radiology and Surgery (CARS), Berlin, Germany, 2005, pp. 1115-1120.
4. **S.E. Yuksel**, A. El-Baz, A.A. Farag and G.C. Postel, "Automatic detection of renal rejection after kidney transplantation," Research!Louisville, Oct. 31 - Nov. 4, 2005. (poster presentation, first place award).